RALT-117

Studies of Muon-Pair Production in e^+e^- Annihilations at the LEP Collider.

Nigel Charles Edward Crosland

St. John's College, Oxford

A thesis submitted for the degree of Doctor of Philosophy at the University of Oxford

January 1991

Studies of Muon-Pair Production in e^+e^- Annihilations at the LEP Collider.

Nigel Charles Edward Crosland
St. John's College, Oxford

Submitted for the degree of Doctor of Philosophy
Hilary Term, 1991

ABSTRACT

Studies of the reaction $e^+e^- \rightarrow \mu^+\mu^-$ ('muon-pair production') using the DELPHI experiment at the LEP Collider are presented.

The design and performance of the DELPHI Barrel Muon Detector are described, and some elements of the associated software are discussed. The methods for selecting muon-pair events and for the calculation of backgrounds and efficiencies are described in detail.

Results are presented for data coming from a scan around the Z^0 peak at seven centre-of-mass energies from 88.22 GeV to 94.22 GeV. A sample of 1322 muon-pair events is selected in the polar angular range $43° \leq \theta \leq 137°$. From a fit to the measured muon-pair cross-sections the square root of the product of the $Z^0 \rightarrow e^+e^-$ and the $Z^0 \rightarrow \mu^+\mu^-$ partial widths is determined to be $(\Gamma_{ee}\Gamma_{\mu\mu})^{1/2} = 83.8 \pm 1.2(\text{stat}) \pm 1.1(\text{sys})$ MeV. The ratio of the hadronic to muon-pair partial widths is found to be $\Gamma_h/\Gamma_{\mu\mu} = 19.97 \pm 0.56(\text{stat}) \pm 0.45(\text{sys})$. The forward-backward asymmetry at the centre-of-mass energy nearest the Z^0 peak $\sqrt{s} = 91.22$ GeV is found to be $A_{FB} = 0.060 \pm 0.040(\text{stat}) \pm 0.005(\text{sys})$. From a simultaneous fit to the muon-pair cross-sections and the forward-backward asymmetries across the Z^0 resonance we find that for the vector and axial coupling constants of electrons and muons $(v_e v_\mu)^{1/2} = -0.116^{+0.074}_{-0.042}(\text{stat}) \pm 0.003(\text{sys})$ and $(a_e a_\mu)^{1/2} = -0.998 \pm 0.010(\text{stat}) \pm 0.007(\text{sys})$. All results are in agreement with the expectations of the Standard Model.

ACKNOWLEDGEMENTS

I am greatly indebted to the hundreds of dedicated and talented people who were involved in the design, construction and successful commissioning of the LEP collider and the DELPHI detector. It has been a great pleasure to work in the DELPHI collaboration and it is a privilege to have the opportunity of writing one of the first theses based on this experiment. I was genuinely impressed by the friendly spirit that characterised this truly international collaboration, even in the middle of a tedious night shift or during those extraordinary times in D1 in the first LEP physics run. In such a large experiment one relies heavily on other people's efforts and they cannot all be acknowledged individually (a list of the present collaboration is given in Appendix A), but where the contribution of certain individuals has been crucial to a piece of work reported in this thesis, this has been acknowledged in the text.

As for individuals, I must first mention Dr Dusan Radojicic, who has been my Supervisor during my spells in Oxford, and Dr Peter Renton, who was my Supervisor during my 15 months at CERN and has kindly continued to assist me since I returned to Oxford to write this thesis. I should like to thank them both not only for their sound advice but also for the friendship and respect they have always shown towards me.

It would be impossible to list all the people who have helped me at some time over the last three years; my thanks go to all the other members of the Oxford DELPHI group; it has always been a pleasure to work in this group. I am particularly grateful to Paul, Andrew, Simon and Christine for their advice on parts of this thesis, and to Jan and Martin for their help and encouragement in the final days.

I give heartfelt thanks to all the friends who made my time in Geneva so enjoyable, principally Andrew, Christine and Martin. Also my thanks to John, Craig, Liz and Andy (who quite by chance all had some part in teaching me to ski!) and Freddy. In Oxford, I have also enjoyed working nearby John Woods, Harald, Simon, Guy, Tim and Jan, and the other members of my year, Sarah, Jon, Andrew and Anita, to whom I send my very best wishes for the future. I should also like to express sincere thanks to all my other friends during my many (many) years in Oxford. My apologies to those I have forgotten.

I am grateful to the Science and Engineering Research Council for financial support.

This thesis is dedicated to my parents, in recognition of many years of love and support.

N. Crosland

11th January 1991.

Preface

The subject of this thesis is muon-pair production in electron-positron annihilations at the Z^0 resonance. The data are from the DELPHI experiment on the new LEP Collider at the European Centre for High Energy Physics (CERN), Geneva.

Data-taking began in August, 1989. As this is one of the first studies of muon-pair production in DELPHI, the design and the performance of the Muon Detector and the software pertinent to the analysis are described in some detail.

Chapter 1 is a brief introduction to the theory of Electroweak Interactions and its predictions for charged fermion pair production at LEP energies (near the Z^0 pole). Chapter 2 includes an introduction to the LEP collider and the DELPHI experiment, with special emphasis on the detectors which are the most important for this study. Chapter 3 is devoted to a detailed description of the design, calibration and testing of the Barrel Muon Chambers, which make an important contribution to muon identification in DELPHI.

There follows in Chapter 4 a description of the main elements of the offline analysis and simulation software. A fuller description is given of two relevant packages: a processor for the simulation of the Muon Detector by a fast algorithm, and the package for muon identification using the Muon Chambers.

In Chapter 5 a study is made of the reaction

$$e^+e^- \rightarrow \mu^+\mu^-(\gamma)$$

This reaction has a final state that is relatively easy to detect, and it is possible to obtain a sample with a high efficiency and a little contamination due to other types of events. The muon-pair event sample is used in the studies of Chapter 6. The Z^0 resonance parameters are obtained by a fit to the cross-section for muon-pair production as a function of centre-of-mass energy. The muon-pair sample is also used to find the ratio of hadronic to leptonic partial decay widths, and obtain the vector and axial vector couplings of the Z^0 to leptons.

Contents

List of Figures

List of Tables

Chapter 1

Introduction

This chapter is in two sections. The first section is a brief discussion of the Standard Model of electroweak interactions. The second describes the predictions of the model for the reaction $e^+e^- \rightarrow f\bar{f}$ at centre-of-mass energies close to the mass of the Z^0 boson (≈ 91 GeV), and includes a discussion of some higher order effects.

1.1 Electroweak Interactions

There are several thorough descriptions of the Standard Model [1], so we confine ourselves to a brief summary of the model and a discussion of the choice of input parameters. It is based on the Glashow-Salam-Weinberg (GSW) [2] model. Like Quantum Chromodynamics (QCD), the theory of strong interactions between quarks, the GSW model is a gauge field theory. We briefly sketch the nature of gauge theories (a detailed treatment may be found in [3] for example) and then state the form of the GSW model.

1.1.1 The Gauge Principle

The Lagrangian for a free Dirac particle of mass m,

$$\mathcal{L}_0 = \overline{\psi}(i\gamma^\mu \partial_\mu - m)\psi. \tag{1.1}$$

is invariant under the *global* phase transformation

$$\psi(x) \longrightarrow \psi'(x) = \exp(-iq\alpha)\psi(x), \tag{1.2}$$

where α is a scalar and the same for all values of the coordinates x, and q is some constant. Invariance under such transformations implies that the phase of the wave function is arbitrary and unobservable — in other words, a matter of convention.

However, invariance under 1.2 implies that once the convention is chosen for one space-time point, the same convention must be followed at all other points. Can different conventions be used at different space-time points? Under the *local* phase transformation

$$\psi(x) \longrightarrow \psi'(x) = \exp\left(-iq\alpha\left(x\right)\right)\psi(x) \tag{1.3}$$

where α is an arbitrary scalar and a function of x, $\mathcal{L}_0$ is not invariant:—

$$\mathcal{L}_0 \longrightarrow \mathcal{L}_0' = \mathcal{L}_0 + q\overline{\psi}\gamma^\mu\psi\partial_\mu\alpha(x). \tag{1.4}$$

But, if we introduce a new, vector field A_μ such that

$$\mathcal{L}_1 = \mathcal{L}_0 - q\overline{\psi}\gamma^\mu\psi A_\mu \tag{1.5}$$

then $\mathcal{L}_1$ *is* invariant under the transformation 1.3 provided that

$$A_\mu(x) \longrightarrow A_\mu'(x) = A_\mu(x) + \partial_\mu\alpha(x). \tag{1.6}$$

If the transformation 1.6 can be performed on a field without changing the physical implications, then it is known as a 'gauge field'.

Therefore, to retain local phase invariance, a gauge field A_μ has been introduced, with an interaction term $-q\overline{\psi}\gamma^\mu\psi A_\mu$ between the matter field ψ and A_μ.

The gauge field 'particles' (its quanta of excitation) must be massless or a term $\frac{1}{2}\mathrm{m}^2A_\mu(x)A^\mu(x)$, which is clearly not invariant under 1.6, would have to be included in the Lagrangian $\mathcal{L}_1$.

Equivalently, we have made the globally invariant Lagrangian $\mathcal{L}_0$ into a locally invariant Lagrangian by replacing ∂_μ by the 'covariant derivative' D_μ, where $\mathrm{D}_\mu = \partial_\mu + iqA_\mu$.

1.1.2 Yang-Mills Gauge Theory

The set of transformations given by equation 1.3 form a unitary group (i.e. each transformation may be represented by a unitary matrix), denoted U(1). It has an infinite number of elements because $\alpha(x)$ is a continuous variable. All elements commute, so the group is said to be 'Abelian'.

Yang and Mills [4] constructed a gauge theory involving invariance under rotations in three-dimensional 'weak isospin' space:

$$\psi(x) \longrightarrow \psi'(x) = \exp(-ig\tau.\mathbf{\Lambda}(x))\psi(x) \tag{1.7}$$

where $\mathbf{\Lambda}$ is an arbitrary vector in isospin space, g is a constant and τ are the Pauli spin matrices . The transformations 1.7 can be represented by the group of all 2 x 2 unitary matrices with the 'special' condition that their determinant equals one. This is called the SU(2) group. It is non-Abelian as the Pauli matrices do not commute.

In this case, local gauge invariance requires three gauge fields of massless particles W_μ^i ($i = 1, 2, 3$) (corresponding to the three components of the vector $\mathbf{W}$ in weak isospin space), which transform as

$$\mathbf{W}_\mu \longrightarrow \mathbf{W}_\mu{}' = \mathbf{W}_\mu + \partial_\mu \mathbf{\Lambda} + g\mathbf{\Lambda} \times \mathbf{W}_\mu. \tag{1.8}$$

The covariant derivative is

$$\mathrm{D}_\mu = \partial_\mu + ig\tau.\mathbf{W}_\mu. \tag{1.9}$$

1.1.3 The Standard Model of Electroweak Interactions

The GSW theory is based on the gauge group $\mathrm{SU}(2)_L \otimes \mathrm{U}(1)_y$. The symmetry requires a total of four massless gauge field bosons:-

- the isovector field $\mathbf{W}_\mu$ is required by the $\mathrm{SU}(2)_L$ symmetry (the subscript L indicates that only left-handed fermions couple to the W_μ^i). This field couples gauge invariantly with a coupling constant g to all particles carrying *weak* isospin, t.

- the isoscalar field B_μ is required by the $\mathrm{U}(1)_y$ symmetry. This field couples gauge invariantly with a coupling constant g' to all particles carrying *weak* hypercharge y.

1.	2.	3.	t^3_f	y_f	Q_f
$\begin{pmatrix} \nu_e \\ e \end{pmatrix}_L$	$\begin{pmatrix} \nu_\mu \\ \mu \end{pmatrix}_L$	$\begin{pmatrix} \nu_\tau \\ \tau \end{pmatrix}_L$	$\begin{matrix} +1/2 \\ -1/2 \end{matrix}$	-1	$\begin{matrix} 0 \\ -1 \end{matrix}$
e_R	μ_R	τ_R	0	-2	-1
$\begin{pmatrix} u \\ d' \end{pmatrix}_L$	$\begin{pmatrix} c \\ s' \end{pmatrix}_L$	$\begin{pmatrix} t \\ b' \end{pmatrix}_L$	$\begin{matrix} +1/2 \\ -1/2 \end{matrix}$	$+1/3$	$\begin{matrix} +2/3 \\ -1/3 \end{matrix}$
u_R	c_R	t_R	0	$+4/3$	$+2/3$
d'_R	s'_R	b'_R	0	$-2/3$	$-1/3$

Table 1.1: Quantum numbers for the elementary fermions. The weak isospin of each multiplet is $t = |t^3|$.

Quarks and leptons are described in weak isospin space by left-handed doublets L, and right-handed singlets R. For example:

$$\begin{aligned} L &= \begin{pmatrix} \nu_e \\ e \end{pmatrix}_L = \frac{(1-\gamma_5)}{2} \begin{pmatrix} \nu_e \\ e \end{pmatrix} \\ R &= e_R = \frac{(1+\gamma_5)}{2} e \end{aligned} \tag{1.10}$$

Here, $\frac{(1-\gamma_5)}{2}$ is a 'helicity projection operator' which selects only left-handed fermions. The weak isospin t, electric charge quantum number Q [1] , and weak hypercharge y for the known "elementary" fermions are given in table 1.1. Note that $Q = t_3 + y/2$. The states d', s', b' are weak interaction quark eigenstates, which are mixtures of the mass eigenstates as described by the Kobayashi-Maskawa matrix [5]. The top quark is included in this table although it has not yet been observed.

The $SU(2)_L \otimes U(1)_y$ symmetry is hidden. The 'Higgs mechanism' [6] is invoked to break this symmetry and generate particle masses. A consequence is the existence of at least one scalar particle, the Higgs boson, which has not yet been observed.

After the symmetry is broken there are still four vector bosons : two charged bosons of equal mass $W^\pm$, a massive neutral boson Z^0 and a massless neutral boson γ (the photon).

[1]i.e. the electric charge is $Q|e|$ where e is the charge on the electron $\approx 1.6 \times 10^{-19}$ C.

The 'physical' fields are constructed from the gauge fields as follows:

$$W^\mu_\pm = \frac{1}{\sqrt{2}}(W^\mu_1 \mp iW^\mu_2) \qquad (\rightarrow W^\pm) \tag{1.11}$$
$$Z^\mu = \cos\theta_W W^\mu_3 - \sin\theta_W B^\mu \qquad (\rightarrow Z^0) \tag{1.12}$$
$$A^\mu = \sin\theta_W W^\mu_3 + \cos\theta_W B^\mu \qquad (\rightarrow \gamma) \tag{1.13}$$

where θ_W is known as the *Weinberg* angle or *weak mixing* angle.

Transitions between left-handed fermions are mediated by the $W^\pm$ bosons ('Charged Current' weak interactions). Neutral Currents do not change flavour and are mediated by the photon and Z^0 .

There are three weak isospin currents, $(j^t_i)^\mu$, and one weak hypercharge current $(j^y)^\mu$. The Neutral Current Lagrangian is given by:

$$\mathcal{L}_{NC} = -g(j^t_3)_\mu W^\mu_3 - \frac{g'}{2}(j^y)_\mu B^\mu \tag{1.14}$$

which in terms of the physical fields may be written:

$$\mathcal{L}_{NC} = -j^{em}_\mu A^\mu - j^{NC}_\mu Z^\mu \tag{1.15}$$
$$\text{where } j^{NC}_\mu = \frac{e}{\cos\theta_W \sin\theta_W}\bar{f}\gamma_\mu \left[t_3\left(\frac{1-\gamma_5}{2}\right) - Q\sin^2\theta_W\right] f \tag{1.16}$$
$$j^{em}_\mu = eQ\bar{f}\gamma_\mu f \tag{1.17}$$
$$g\sin\theta_W = g'\cos\theta_W = e \tag{1.18}$$

Here, j^{em}_μ and j^{NC}_μ are the electromagnetic and weak neutral currents respectively, and f represents a fermion field.

1.1.4 The Weak Mixing Angle

The weak mixing angle is defined in several ways which are equivalent to lowest order:

- by the 'unification condition': $g\sin\theta_W = g'\cos\theta_W = e$
- by comparison at $q^2 \ll M^2_W$ with the Fermi theory of charged current interactions:

$$G_F = \frac{\pi\alpha}{\sqrt{2}\, M^2_W \sin^2\theta_W} \tag{1.19}$$

  where $\alpha = e^2/4\pi$ is the fine structure constant. G_F, the Fermi constant, has been measured very accurately from the muon lifetime. α can be determined very precisely from the Josephson effect (see table 1.2).

- in the Higgs mechanism the leptons and quarks can acquire mass as a result of their couplings to the Higgs field, but the resulting masses are free parameters. The relationship between the masses of the gauge bosons *is* predicted however, and for a weak isospin doublet field

$$\sin^2\theta_W = 1 - M_W^2/M_Z^2 \tag{1.20}$$

- in the definition of the weak neutral current j_μ^{NC}, equation 1.16.

Note that these definitions are no longer equivalent once higher order effects ('radiative corrections') have been considered.

1.1.5 Electroweak Radiative Corrections

To summarise the preceding section, electroweak interactions are thought to be described by a relativistic quantum field theory in the form of a non-Abelian gauge theory, with spontaneous symmetry breaking. Such theories are renormalisable: that is, any observable can in principle be calculated to an arbitrary order of perturbation theory , in terms of a finite number of input parameters. It is the existence and consistency of the higher orders of the perturbation expansion — the 'radiative corrections' — which give the Standard Electroweak Model the character of a quantum field theory.

The systematic verification of the electroweak theory has been described [7] as the *'raison d'être* of LEP'. At LEP energies the radiative corrections are large and must be accurately computed. High precision measurements of electroweak observables (for instance M_Z, M_W, asymmetries) test the electroweak radiative corrections predicted by the Standard Model. Deviations from predictions may signify the existence of heavy unseen particles of the model — the Higgs boson and the top quark — or new particles and/or symmetries (e.g. compositeness, technicolor, supersymmetry).

1.1.6 Renormalisation Schemes

A choice of renormalisation scheme involves the choice of defined quantities (i.e. input parameters) *and* the energies at which the definitions are made. All renormalisation schemes are in principle equivalent, but the results in a *given order* of perturbation theory will differ between schemes.

The Standard Model Lagrangian has in its manifest $SU(2)_L \otimes U(1)_y$ symmetric form the following input parameters: the coupling constants g and g', two coefficients to describe the Higgs potential μ^2 and λ, and coupling constants g_f to describe the coupling between the elementary fermions and the Higgs field. None of these parameters can be measured directly.

An alternative set of independent input parameters is

$$\alpha, M_W, M_Z, M_H, m_f \tag{1.21}$$

where m_f is a shorthand notation for the fermion masses and the weak quark mixing angles, and M_H is the mass of the Higgs boson. Each quantity can be measured, in principle. α is defined at $q^2 = 0$, and the W and Z^0 masses are defined on their mass shells[2]. M_H and the top quark mass m_t are unknown of course. The scheme which uses this set of parameters is known as the 'on-shell renormalisation scheme' [8].

Parameter	Measured values	Reference
α	1/137.0359895(61)	[9]
G_F	$1.16637(2) \times 10^{-5}\mathrm{GeV}^2$	[9]
M_Z	$91.188 \pm 0.013 \pm 0.030$ GeV	[10]
M_W	80.6 ± 0.4 GeV	[9]

Table 1.2: Recent Measured Values of some Standard Model Parameters

If we now adopt Sirlin's definition of $\sin^2\theta_W$ in terms of the physical W and Z masses (i.e. adopt equation 1.20 as the *definition* of $\sin^2\theta_W$) then the weak mixing angle is a constant, independent of the process involved or of energy scale. It is not an independent input parameter and can, in principle, be avoided completely (but is useful as a form of shorthand). We may then rewrite equation 1.19 as

$$G_\mu = \frac{\pi\alpha}{\sqrt{2}M_W^2}\frac{M_Z^2}{M_Z^2 - M_W^2}\frac{1}{(1-\Delta r)} \tag{1.22}$$

[2]i.e. The boson masses are defined as the pole positions of their corresponding propagators; see for example equation 1.33.

where G_μ is the Fermi constant measured in muon decay (in which certain purely electromagnetic corrections are incorporated) and

$$\Delta r \equiv \Delta r(\alpha, M_W, M_Z, M_H, M_f) \tag{1.23}$$

is the radiative correction in the on-shell scheme (see [11] for an explicit formula).

In this renormalisation scheme we may calculate M_W (or equivalently $\sin^2\theta_W$) from M_Z, Δr and G_μ in equation 1.22. This amounts to the replacement of M_W by G_μ (which is at present more accurately known — see again table 1.2) in the set of input parameters to the Standard Model given by 1.21.

After the input parameters have been defined, all other observables in the Standard Model can be calculated and compared with experimental results, in order to test the theory.

1.2 The Reaction $e^+e^- \rightarrow f\bar{f}(\gamma)$

1.2.1 Propagators and Vertex Factors

Production of charged fermion pairs in e^+e^- annihilation experiments, occurs throug ngle photon or Z^0 exchange in the s-channel, as shown in figure 1.1 [3]. Where the final state fermions are electrons, both γ and Z^0 may be exchanged in the t-channel as well.

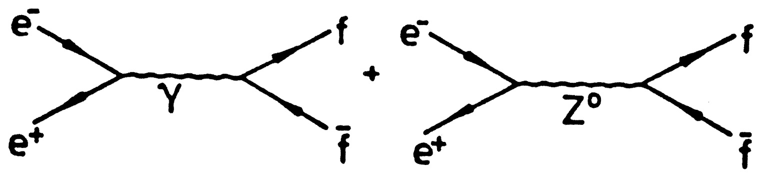

Figure 1.1: Lowest order Feynman diagrams contributing to $e^+e^- \rightarrow \mu^+\mu^-$

The vertex factor for Z^0 coupling to fermions may be written (c.f. equation 1.16):

$$V_Z = \frac{-ie}{\sin\theta_W \cos\theta_W}\gamma_\mu\left(\left(\frac{1-\gamma_5}{2}\right)t_3^f - Q^f \sin^2\theta_W\right) \tag{1.24}$$

where the superscript f stands for the fermion. Equation 1.24 may be rewritten:

1. In terms of the couplings to left and right handed particles

$$V_Z = \frac{-ie}{\sin\theta_W \cos\theta_W}\gamma_\mu\left(g_L^f\left(\frac{1-\gamma_5}{2}\right) + g_R^f\left(\frac{1+\gamma_5}{2}\right)\right) \tag{1.25}$$

where

$$g_L^f = t_3^f - Q^f \sin^2\theta_W \tag{1.26}$$

$$g_R^f = -Q^f \sin^2\theta_W \tag{1.27}$$

2. In terms of axial vector and vector couplings

$$V_Z = \frac{-ie}{4\sin\theta_W \cos\theta_W}(v_f\gamma_\mu - a_f\gamma_\mu\gamma_5) \tag{1.28}$$

[3]Higgs exch ge can be neglected because of the ail Yukawa coupling to the electron.

where

$$\begin{aligned} v_f &= 2(g_L^f + g_R^f) = 2g_V^f = 2t_3^f - 4Q^f \sin^2\theta_W & (1.29) \\ a_f &= 2(g_L^f - g_R^f) = 2g_A^f = 2t_3^f & (1.30) \end{aligned}$$

For example, the axial and vector couplings to muons are:

$$\begin{aligned} v_\mu &= -1 + 4\sin^2\theta_W \approx -0.092 \qquad (\text{using } \sin^2\theta_W = 0.227) & (1.31) \\ a_\mu &= -1 \end{aligned}$$

The photon coupling to fermions is purely vector: $V_\gamma = -ieQ\gamma_\mu$. The photon and Z^0 propagators may be written:

$$\begin{aligned} P_\gamma &= \frac{-ig^{\mu\nu}}{q^2} & (1.32) \\ P_Z &= \frac{i}{(q^2 - M_Z^2 + iM_Z\Gamma_Z)}\left(-g^{\mu\nu} + \frac{q^\mu q^\nu}{M_Z^2}\right) & (1.33) \end{aligned}$$

where Γ_Z is the 'width' of the Z^0 and is related to its lifetime τ_Z by $\tau_Z = \hbar/\Gamma_Z$.

1.2.2 The Cross-section

From the vertex factors and propagators described above, the differential cross-section for the annihilation of unpolarized electrons and positrons into final state fermions f may be derived, giving to lowest order:

$$\frac{d\sigma_f^0}{d\Omega} = \frac{\alpha^2}{4s}\left[A_1(s)(1+\cos^2\theta) + A_2(s)\cos\theta\right] \qquad (1.34)$$

$$\text{where } A_1 = Q_e^2 Q_f^2 + 2Q_e Q_f v_f v_e \Re(\chi) + (v_e^2 + a_e^2)(v_f^2 + a_f^2)|\chi|^2 \qquad (1.35)$$

$$A_2 = Q_e Q_f a_e a_f \Re(\chi) + 8 v_e v_f a_e a_f |\chi|^2 \qquad (1.36)$$

Here, $\sqrt{s}$ is the centre-of-mass energy, θ is the angle between the incoming electron and the outgoing fermion in the centre-of-mass frame [4], and $\Re(\chi)$ denotes

[4]Note that throughout this section, f stands for an elementary fermion and to obtain the cross-section, partial widths etc for any particular *quark flavour* it is necessary to sum over the three quark colours. One should multiply the relevant expression by the 'colour factor', which is $3(1 + \alpha_s/\pi)$ to first order in the strong coupling constant α_s.

the real part of χ. Fermion masses have been neglected (this formula is not valid for $e^+e^- \rightarrow t\bar{t}$).

The quantity $\chi(s)$ may be written:

$$\chi(s) = \frac{1}{16 \sin^2\theta_W \cos^2\theta_W} \frac{s}{(s - M_Z^2 + iM_Z\Gamma_Z)} \tag{1.37}$$

The term in equation 1.34 which is independent of $\chi(s)$ arises from photon exchange, that which depends on $|\chi(s)|^2$ arises from Z^0 exchange, and the term in $\Re(\chi)$ arises from γ-Z^0 interference.

From equation 1.34, the total cross-section is derived by integrating over all angles:

$$\sigma(s) = 2\pi \int_{-1}^{1} \frac{d\sigma}{d\Omega} \, d\cos\theta \tag{1.38}$$

$$= \frac{4\pi\alpha^2}{3s} A_1(s) \tag{1.39}$$

Around $\sqrt{s} = M_Z$, Z^0 exchange dominates and A_1 is approximately proportional to χ^2 (note that $\Re(\chi) = 0$ when $s = M_Z^2$):

$$\sigma_f^0(s = M_Z^2) \approx \frac{4\pi\alpha^2}{3s} \frac{(v_e^2 + a_e^2)(v_f^2 + a_f^2)}{256 \sin^4\theta_W \cos^4\theta_W} \frac{s^2}{(s - M_Z^2)^2 + M_Z^2\Gamma_Z^2} \tag{1.40}$$

1.2.3 The Cross-Section and Partial Widths

The decay rate of $Z^0 \rightarrow f\bar{f}$ is given by Γ_{ff} where Γ_{ff} is the 'partial width' to $f\bar{f}$. For massless fermions this is given by:

$$\Gamma_{ff} \approx \frac{e^2 M_Z}{192\pi \sin^2\theta_W \cos^2\theta_W} \left(v_f^2 + a_f^2\right) \tag{1.41}$$

$$= \frac{G_F M_Z^3}{24\pi\sqrt{2}} \left(v_f^2 + a_f^2\right) \tag{1.42}$$

$$\approx 82.9 \left(v_f^2 + a_f^2\right) \text{ [MeV]} \tag{1.43}$$

where we have put $M_Z = 91.2$ GeV and $G_\mu = 1.166 \times 10^{-5}$ GeV^2 . For example, the partial width to a light neutrino $\Gamma(Z^0 \rightarrow \nu\bar{\nu})$ is about 166 MeV ($v_f^\nu = a_f^\nu = 1$) while $\Gamma(Z^0 \rightarrow \mu^+\mu^-)$ is about 83.6 MeV. The Z^0 total width Γ_Z is simply the sum of the partial widths over all kinematically accessible final states:

$$\Gamma_Z = \Gamma_{\nu\nu} + \Gamma_{ee} + \Gamma_{uu} + \Gamma_{dd} + ... \tag{1.44}$$

The total width has been measured from shape of the Z^0 resonance (including higher order effects) to be $2.476 \pm 0.026 \pm 0.010$ GeV [10].

We may now rewrite the cross-section to final state fermion f (equation 1.40) in terms of partial widths:

$$\sigma_f^0(s) \approx \frac{12\pi\Gamma_{ee}\Gamma_{ff}}{M_Z^2} \cdot \frac{s}{(s - M_Z^2)^2 + M_Z^2\Gamma_Z^2} \tag{1.45}$$

Note that the cross-section is directly proportional to Γ_{ff}.

The resonance shape given by 1.45 has its maximum at

$$\sqrt{s} = M_Z \left(1 + \frac{\Gamma_Z}{M_Z}\right)^{1/4} \approx 1.0001\ M_Z \tag{1.46}$$

The cross-section at the Z^0 mass is simply:

$$\sigma_f^0(s = M_Z^2) \approx \frac{12\pi\Gamma_{ee}\Gamma_{ff}}{M_Z^2\Gamma_Z^2} \tag{1.47}$$

Using $\Gamma_{ee} = \Gamma_{\mu\mu} = 83.6 \times 10^{-3}$ GeV, $M_Z = 91.2$ GeV, $\Gamma_Z = 2.476$ GeV, we find $\sigma_\mu^0 = 5.2 \times 10^{-6}$ GeV^{-2} or about 2 nb.

The distance between the right and left half-maxima of the lowest order resonance differs from Γ_Z by only about one part in 10^4.

1.2.4 Forward-Backward Asymmetry

The term in $\cos\theta$ in expression 1.34 leads to an asymmetry between the number of fermions produced in the forward direction [5] N_F and the number produced in the backward direction N_B when A_2 is non-zero, given by:

$$A_{FB}^f(s) = \frac{N_F - N_B}{N_F + N_B} \tag{1.48}$$

$$= \frac{\int_0^1 \frac{d\sigma_f}{d\Omega} d\cos\theta - \int_{-1}^0 \frac{d\sigma_f}{d\Omega} d\cos\theta}{\int_0^1 \frac{d\sigma_f}{d\Omega} d\cos\theta + \int_{-1}^0 \frac{d\sigma_f}{d\Omega} d\cos\theta} \tag{1.49}$$

$$= \frac{3}{8} \frac{A_2(s)}{A_1(s)} \tag{1.50}$$

[5] The 'forward' direction means that hemisphere where the angle θ between the incoming electron and the outgoing fermion is less than 90°.

When $\sqrt{s} = M_Z$, then to lowest order and neglecting terms from γ exchange:

$$A^f_{FB}(s = M_Z^2) \approx \frac{3}{4} A_e A_f \tag{1.51}$$

$$\text{where } A_f = \frac{2v_f a_f}{v_f^2 + a_f^2} \tag{1.52}$$

Now consider A^μ_{FB}. As have seen, $v_\mu = v_e \approx -0.09$. Since A^μ_{FB} is proportional to the *square* of the vector coupling constant (or the square of $\sin^2\theta_W$), then near the Z^0 mass the forward-backward asymmetry is quite small [6]. Using $a_\mu = a_e = -1, A^\mu_{FB}(\sqrt{s} = M_Z) \approx 3\%$.

In general A_{FB} is a rapidly varying function of s around the Z^0 resonance and switches sign close to the Z^0 pole (where $\Re(\chi)$ changes sign), as shown in figure 1.5.

When higher order effects are taken into account, this asymmetry is not solely due to weak interaction effects [7].

1.2.5 Electroweak Radiative Corrections to $e^+e^- \to f\bar{f}$

In the on-shell renormalisation scheme the one loop ($O(\alpha)$) electroweak corrections to the process $e^+e^- \to f\bar{f}$ can be naturally separated into two classes:

- 'QED corrections' : diagrams with one extra photon (either a real bremsstrahlung photon or a virtual photon loop, depicted in figure 1.2).
- 'Electroweak corrections': all other one loop diagrams. These involve corrections to the vector boson propagators (figure 1.3), and vertex corrections (excluding virtual photon contributions), and box diagrams with two massive bosons exchanged (figure 1.4).

The largest corrections are due to photon radiation, mainly in the initial state, which leads to a significant production of Z^0 well above the pole (figure 1.5).

[6] A_{FB} is less sensitive to the weak mixing angle than asymmetries which are linear in $\sin^2\theta_W$, but these require a degree of longitudinal polarisation in the incident beams (or measurement of the polarisation of the final state fermion).

[7] A non-zero forward-backward asymmetry implies that the $f\bar{f}$ system is not an eigenstate of the charge conjugation operator $\mathcal{C}$, which transforms a particle into its antiparticle, leaving spin unchanged. In Z^0 exchange, the final state is not an eigenstate of $\mathcal{C}$ (or parity, $\mathcal{P}$). For lowest order γ exchange the final state *is* an eigenstate of $\mathcal{C}$, with eigenvalue C=-1 (the C-parity of the virtual photon). If this were the only diagram the asymmetry would be zero. However, purely QED corrections *do* make a contribution to A_{FB}, because in higher order diagrams involving two virtual photons the final state can have C=+1.

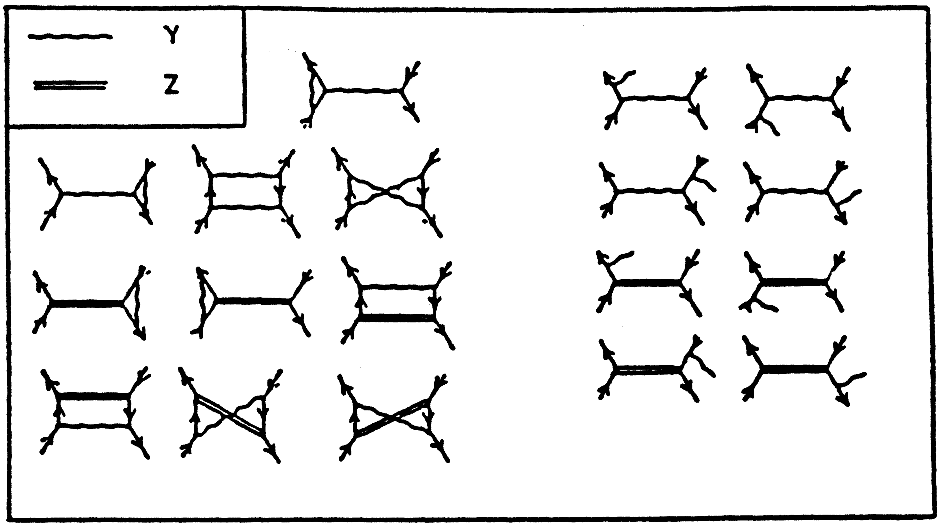

Figure 1.2: QED Corrections to $e^+e^-\rightarrow\mu^+\mu^-$ from [12]

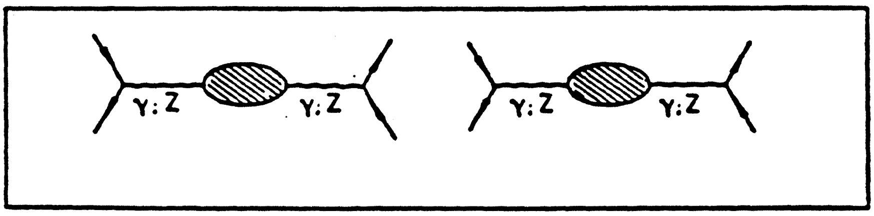

Figure 1.3: Propagator corrections to $e^+e^-\rightarrow\mu^+\mu^-$ from [12]

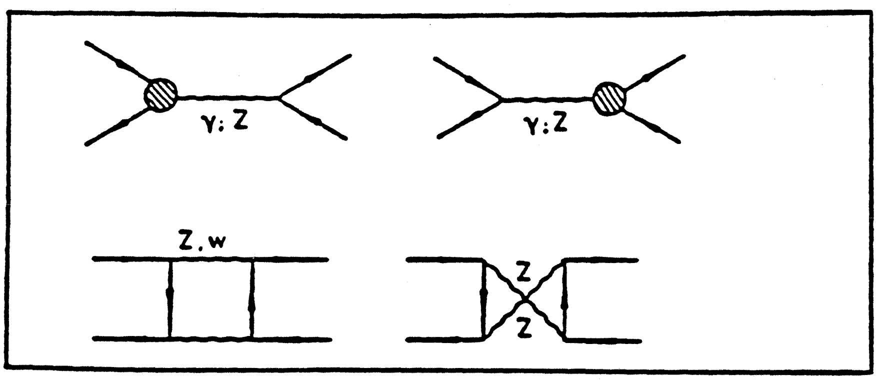

Figure 1.4: Vertex corrections and box contributions to $e^+e^-\rightarrow\mu^+\mu^-$ from [12]

These purely QED corrections are generally not so interesting with respect to the underlying theory, but they need careful treatment as they are large and are dependent on the experimental details (via the cuts applied on the final state photon).

The propagator corrections (frequently called 'oblique corrections') involve the virtual presence of all physical states — including the Higgs boson and the top quark. Using relation 1.22, precision measurements of M_Z and M_W (or M_Z, and $\sin^2\theta_W$ from an asymmetry, say) lead to a measured value of Δr which can give limits on m_t, M_H or other particles beyond the Standard Model. For light final state fermions ($f \neq b, t$) the vertex corrections of figure 1.4 contain only W and Z^0 in virtual states as the Higgs-fermion Yukawa coupling is so small.

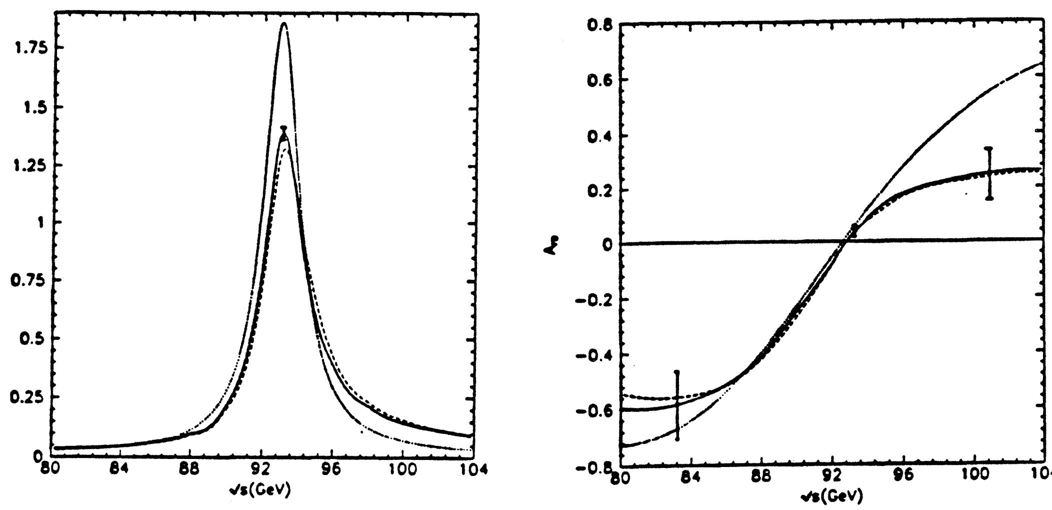

Figure 1.5: Total cross-section and forward-backward asymmetry for $e^+e^- \to \mu^+\mu^-$ as a function of $\sqrt{s}$, from [13]. The dotted curves correspond to the Born (lowest order) approximation. The dashed curves are first order corrected. However, effects of higher than first order are large, especially in the initial state bremsstrahlung. The full curves are obtained with the event generator DYMU2 [13], which takes into account electromagnetic radiative corrections to an order higher than 1.

Chapter 2

The LEP Collider and the DELPHI Experiment

2.1 LEP

The pilot run of the newly-commissioned Large Electron Positron Collider (LEP) at CERN started just before midnight on Sunday August 13^{th}, 1989. Five minutes later the first Z^0 was observed in the OPAL detector.

The first studies of the feasibility and physics possibilities of a large e^+e^- storage ring at CERN were begun in the late 1970's. Civil engineering for LEP began in the spring of 1983. Approximately 1.2 million cubic metres of earth were excavated. LEP is housed in a circular tunnel of length 26.7 km and internal diameter 3.8 m, which is large enough for the Large Hadron [proton-proton] Collider to be installed above the LEP beam pipe. The first magnets were installed in June 1987 — altogether around 3300 dipole magnets (each 6 m long) were required in the arcs, plus around 1500 quadrupoles and sextupoles for focussing. On July 14^{th}, 1989[1] a beam of positrons was steered around the full ring to complete the 'first turn'. In the next month electrons were successfully injected, the intensity of the stored beams climbed towards 500 μA, and beams were accelerated. In the five day pilot run 58 Z^0's were collected in total in the four experiments on LEP. The first physics run, which included a scan of the Z^0 resonance, started on September 20^{th}. The LEP machine was officially inaugurated on November 13^{th}, 1989.

The first stage of LEP has a maximum energy of about 50 GeV per beam and is capable of producing thousands of Z^0 bosons per day from electron-positron annihilations. When suitable superconducting cavities are installed, the energy

[1]The bicentenary of the French Revolution.

will be developed towards 100 GeV per beam — sufficient to produce pairs of W bosons. The machine is built on a slope (1.4° to the horizontal), so that from the foothills of the Jura mountains to the suburbs of Geneva, it is always between 50 m and 170 m below the ground.

The ring is not a perfect circle: there are eight 2.8 km long arcs linked by eight straight sections. In the middle of four of these straight sections are large underground halls (or 'pits') , 23 m in diameter and 70 m long, which house the four experiments. The injector complex, which delivers to LEP electrons and positrons of 20 GeV, is shown in figure 2.1. It comprises:

- a 200 MeV LINAC which delivers electrons on to a converter target to produce positrons;
- a LINAC which accelerates the positrons/electrons to 600 MeV;
- a 600 MeV storage ring (the EPA, or Electron Positron Accumulator ring);
- the Proton Synchrotron (PS) which accelerates electrons/positrons to 3.5 GeV;
- the Super Proton Synchrotron (SPS) which accelerates electrons/positrons to 20 GeV and injects them into the LEP ring.

The injector system is able to provide protons from the SPS for fixed-target experiments in parallel with LEP operation.

For the physics runs in 1989 and 1990, LEP has operated with four bunches per beam. Four of the eight possible intersection points are equipped with large general purpose experiments[2] : they are ALEPH, L3, OPAL and DELPHI. At the other four potential interaction regions the beams are kept separate.

A summary of the main parameters of the first phase of LEP is given in table 2.1. Further details on the design of LEP may be found in [16].

[2] For a good summary of the design specifications of the four detectors, see [14].

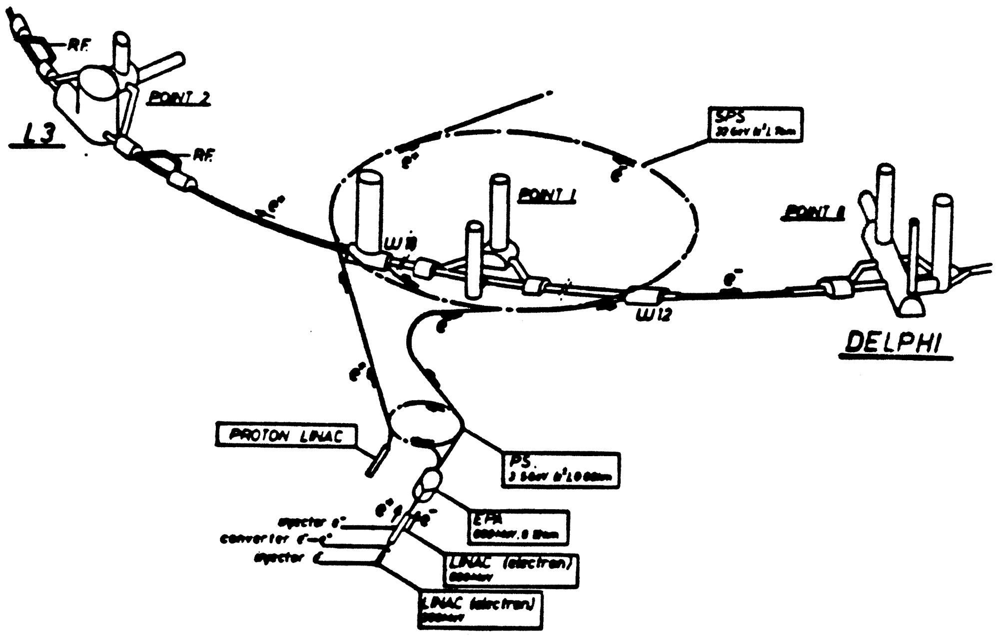

Figure 2.1: The LEP Injector Complex

2.1.1 Future of LEP

Several upgrades of LEP are under discussion to maximise its physics potential, including:

- LEP200: an upgrade of the beam energy to 100 GeV in order to cross the threshold for W-pair production. The energy lost per turn due to synchrotron radiation goes as the fourth power of the beam energy so it will be around 16 times greater[3] at LEP200. Superconducting cavities are planned to prevent costs due to power consumption being prohibitive [17].

- LEP with polarised beams: high precision on electroweak observables may be achieved by measuring various asymmetries with longitudinally polarised beams [18]. In theory, the beams in LEP may naturally become 90% transversely polarised in about 310 minutes[4]. Dedicated 'wiggler' magnets

[3]For a particle of energy E travelling in a circle of radius r the energy loss per turn due to synchrotron radiation is given by [15]:

$$\Delta E[\text{GeV}] = 8.85 \times 10^{-5}\ E^4[\text{GeV}]/r[\text{m}] \tag{2.1}$$

The average radius at LEP is roughly $r = 4200$ m. For $E = 45$ GeV, $\Delta E \approx 86$ MeV or about 0.2%. If $E = 100$ GeV, $\Delta E \approx 2.1$ GeV (2.1%).

[4]Longitudinal polarisation of 50% would be enough to make the experiments viable.

Circumference (including sagitta in dipoles)	26658.883 m
Average radius	4242.893 m
Bending radius in the dipoles	3096.175 m
Phase advance/period	60 or 90 degrees
Horizontal betatron wave number	70.35 or 94.35
Vertical betatron wave number	78.20 or 98.20
Momentum compaction factor	3.866×10^{-4}
Number of bunches per beam	4
Number of interaction points	4 + 4
Equipped experimental areas (P2, P4, P6, P8)	4
Ratio horizontal/vertical β-values at the interaction point	25
RF frequency	352.20904 MHz
Revolution time	88.92446 μs
Harmonic number	31320
Nominal klystron output power (total)	16 MW
Active RF structure length	272.377 m
RF gradient	1.474 MV/m
Injection energy	20 GeV
Maximum beam energy (zero luminosity)	~ 60 GeV
Peak luminosity (3 mA beam current and $\xi = 0.03$)	1.6×10^{31} cm^{-2}s^{-1}
Beam energy at peak luminosity	55 GeV

Table 2.1: The Main LEP Parameters (phase 1)

are required to reduce this polarisation time. Spin rotators are needed to produce longitudinally polarised beams, and polarimeters are required to monitor the polarisation.

- LEP with high luminosity: there is a proposal to increase the luminosity in order to have a better chance of seeing rare decays and to obtain more accurate measurements of electroweak parameters. A machine with 36 bunches each of electrons and positrons could have a luminosity of order 1.4×10^{32} cm^{-2}s^{-1} [19].

2.1.2 Luminosity

Luminosity $\mathcal{L}$ is a measure of the useful flux of beam particles. By definition, the number of events n obtained in time t for a reaction of cross-section σ is:

$$n = \mathcal{L} t \sigma \tag{2.2}$$

For two bunches, containing N_1 and N_2 particles, uniformly distributed in beams of cross sectional area A at the intersection, which collide at rate ν, we have

$$\mathcal{L} = \frac{\nu N_1 N_2}{A}. \tag{2.3}$$

For a multibunch machine where N_1 and N_2 are the number of particles per bunch we have simply:

$$\mathcal{L} = \frac{b f N_1 N_2}{A} \tag{2.4}$$

which is linear in b, the number of bunches per beam (f is the revolution frequency).

In practice, the calculation is much more complicated as the bunches are not uniform. The luminosity is determined from the rate of small angle Bhabha events ($e^+e^- \rightarrow e^+e^-$), for which the cross-section is high and relatively well-known[5].

The design peak luminosity of LEP is 1.7×10^{31} cm^{-2}s^{-1}. Assuming $\sigma = 40$ nb, we obtain a production rate of Z^0 on the peak of about 0.5 Hz (1 nb $= 10^{-33}$ cm^2). In a year of 10^7 s, the integrated luminosity $\mathcal{L}t$ might be about 100 pb^{-1} , corresponding to about 4×10^6 Z^0 in each experiment.

In 1990, the luminosity was around a fifth of design and some time was devoted to machine development, but DELPHI still collected over 10^5 Z^0 events.

[5]The cross-section is determined from QED with a small correction (< 1%) from weak processes.

2.2 DELPHI

DELPHI (or **DE**tector with **L**epton, **P**hoton, and **H**adron **I**dentification) has been designed and built by physicists and engineers from around 39 institutes (for a list of physicists see Appendix A). One of these institutes is Oxford University, which, in collaboration with the Rutherford Appleton Laboratory, built the Barrel Muon Detector, and has also provided effort and money for the data acquisition project and (from 1989) for the Vertex Detector.

DELPHI has its emphasis on particle identification. The original aims [20] were to build a detector characterised by:

1. hadron and lepton identification over approximately 90% of the full solid angle;
2. fine granularity in all the components;
3. three dimensional information on every track and energy deposition.

Particle identification is achieved by combining information from:

- Electromagnetic and Hadron Calorimeters and Muon Chambers with nearly 4π coverage;
- ionisation measurements in a Time Projection Chamber (TPC);
- velocity measurements in Ring-Imaging CHerenkov Counters (RICHs).

DELPHI is also designed to have precise vertex determination. A view of the experiment is shown in figure 2.2. The DELPHI z-axis is coincident with the electron beam, the y-axis points vertically upwards and the x-axis points towards the centre of LEP. The polar angle θ is measured from the z-axis while the azimuthal angle ϕ is measured from the x-axis. Space points are expressed either in Cartesian coordinates (x, y, z) or cylindrical coordinates $(R, R\phi, z)$, where $R = \sqrt{x^2 + y^2}$ and $R\phi = R \times \phi$.

DELPHI has an axial magnetic field (in common with the other LEP detectors) , provided by a superconducting solenoid of length 7.4 m and internal

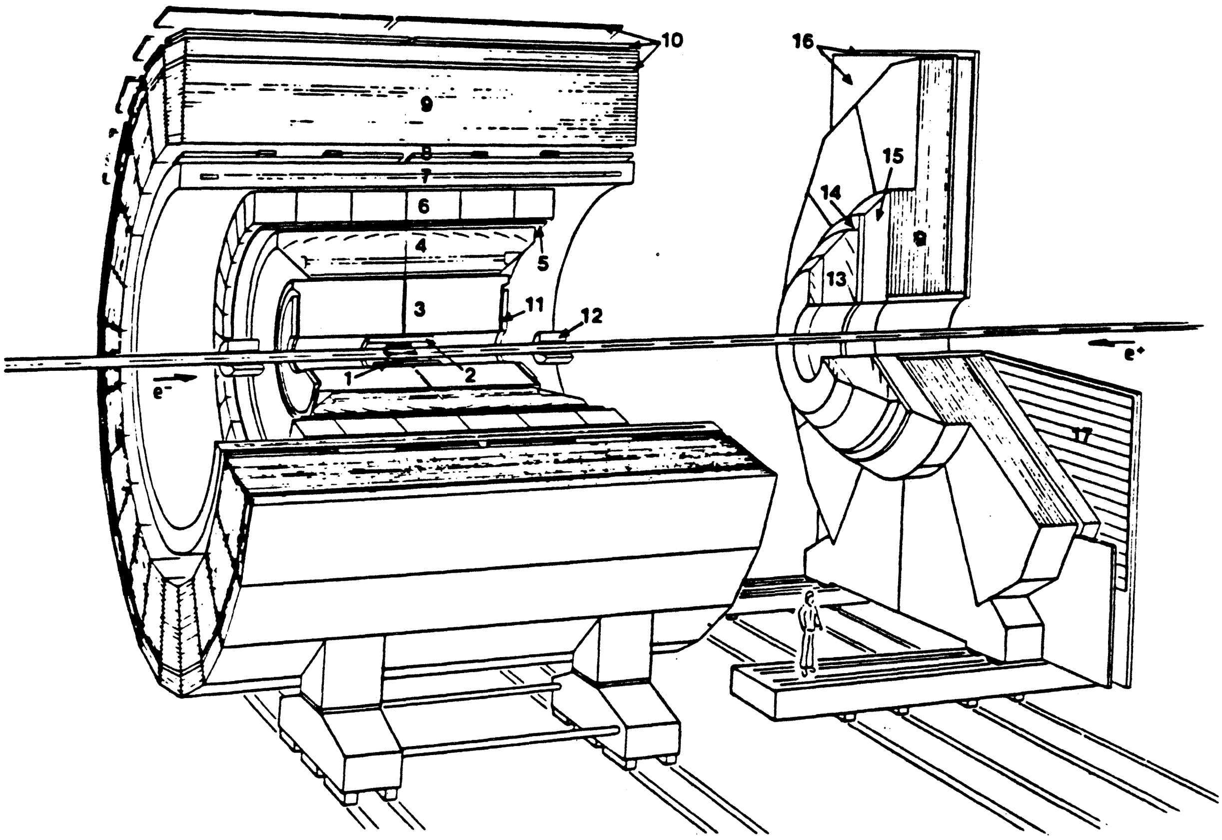

Figure 2.2: Perspective view of the the DELPHI experiment. 1: Vertex Detector (VD). 2: Inner Detector (ID). 3: Time Projection Chamber (TPC). 4: Barrel Ring Imaging CHerenkov Counter (BRICH). 5: Outer Detector(OD). 6: High Density Projection Chamber (HPC). 7: Superconducting Solenoid. 8: Time of Flight Counters (TOF). 9: Hadron Calorimeter (HCAL). 10: Barrel Muon Chambers (MUB). 11: Forward Chamber A (FCA). 12: Small Angle Tagger (SAT). 13: Forward RICH (FRICH). 14: Forward Chamber B (FCB). 15: Forward Electromagnetic Calorimeter (FEMC). 16: Forward Muon Chambers (MUF). 17: Forward Scintillator Hodoscope (HOF). The Very Small Angle Tagger (VSAT) is mounted outside this view.

diameter 5.2 m. The design field is 1.23 T (5000 A) [6]. The Solenoid, and the detectors which are coaxial with it, form the 'Barrel' of DELPHI. At each end of the Barrel are the 'End-Caps', or 'Forward' regions.

We now give a brief description of the various detectors which combine to form the DELPHI experiment. Emphasis will be placed on those detectors which are most relevant to an analysis of the reaction $e^+e^- \rightarrow \mu^+\mu^-$,where the final state muons are observed in the Barrel detectors. Further details may be found in the 1990 DELPHI technical paper [21] and the references therein.

2.2.1 Tracking Detectors

DELPHI has six independent tracking devices. Combining their information accurately is essential for the trigger and for general event reconstruction (in particular, for good momentum resolution).

Vertex Detector (VD)

During 1989 and 1990, the DELPHI beam pipe has been of aluminium, with a diameter of 158.4 mm. Outside it is a Vertex Detector, which consists of two concentric polygons of silicon strip detectors of length 24.0 cm, mounted at average radii of 90 and 110 mm. The aim is to achieve good $R\phi$ resolution (about 5 μm for a single track), mainly for heavy flavour physics.

For 1991 a 106 mm diameter beryllium beam pipe is planned for DELPHI, and a third layer of the Vertex Detector will be added inside the first two, as close to the interaction region as possible. In a future upgrade, extra strips will be added for z-information.

At the time of this study, the usefulness of VD information is limited by the accuracy of its alignment with the other tracking detectors.

Inner Detector (ID)

The Inner Detector provides positional information for vertex extrapolation, improved momentum resolution , and trigger information. It covers polar (θ) angles of approximately 29° to 151° at radii between 12 and 28 cm, and comprises:

[6] Approximately 30% of the data taken in the 1989 runs were taken in a field of 0.7 T. However, these data are not used in this analysis.

- an inner cylindrical drift chamber, giving 24 $R\phi$ points per track;
- 5 cylindrical MWPC (Multi-Wire Proportional Chamber) layers, which provide fast trigger information and solve left-right ambiguities in the inner chamber. Cathode strips give fast z information for the trigger.

Time Projection Chamber (TPC)

The main tracking device of DELPHI is a Time Projection Chamber, which provides at least four three-dimensional space-points for $22° \leq \theta \leq 158°$, and up to 16 three-dimensional space-points between 39° and 141°. Preliminary space-point precision is:

$$\begin{aligned} \sigma_{R\phi} &= 180 - 280\ \mu\mathrm{m} \\ \sigma_z &\leq 0.9\ \mathrm{mm}. \end{aligned}$$

Two-track separation is 1-2 cm.

The TPC has a 30 cm inner and 122 cm outer radius[7]. Electrons formed by an ionising particle drift away from the central plane ($z = 0$) of DELPHI towards the End-Caps in sections each of length 150 cm. The image of the ionising track is widened by the transverse diffusion of the electrons during drifting, but the electric drift field and the magnetic field are (very nearly) parallel and the magnetic field considerably reduces this widening by forcing the electrons to perform helical movements around the magnetic field lines.

The two-dimensional projected image in the R-$R\phi$ plane is reconstructed using cathode pad readout (there are 16 circular pad rows and 192 sense wires). The arrival time of the drifted electrons at the End-Cap gives the z coordinate.

The $\mathrm{d}E/\mathrm{d}x$ information (rate of energy loss of the track by ionisation) may be used to distinguish electrons and pions below 8 GeV.

Outer Detector (OD)

The Outer Detector covers θ angles between 40° to 140° at radii between 198.0 and 207 cm (the Barrel RICH is placed between the OD and the TPC). 5 staggered

[7]The TPC is necessarily smaller than the ALEPH TPC (outer radius 1.8 m, drift length 2.2 m) to allow space for the RICHs.

layers of drift tubes provide accurate $R\phi$ information; 3 of these also provide crude but fast z information to be used in the trigger.

Preliminary resolution is:

$$\begin{aligned} \sigma_{R\phi} &= 110\ \mu\text{m} \\ \sigma_z &\leq 44\ \text{mm}. \end{aligned}$$

With such a precise $R\phi$ coordinate and a relatively long 'lever-arm' (it is further from the interaction point than the other tracking detectors) the OD greatly improves the overall momentum resolution, especially for fast particles (such as muons in muon-pair events).

The OD also provides fast trigger information in both $R\phi$ and z. In addition, by comparison of drift distances over the 5 staggered layers, the OD can measure the time of passage of the ionising particle , which may identify background events (e.g. cosmic muons).

Forward Chambers (FCA,FCB)

The Forward Chambers are drift chambers which provide triggering and (x,y) coordinates for tracking in the End-Cap regions for angles $11° \leq \theta \leq 33°$ (and similar angles in negative z). The FCA chambers are mounted on both ends of the TPC. The FCB chambers are placed between the Forward RICH and the Forward Electromagnetic Calorimeter.

2.2.2 Scintillators

Time of Flight (TOF)

The Time of Flight system comprises a single layer of 172 counters (each counter has dimensions 355 cm$\times$19 cm$\times$2 cm) arranged in 24 sectors and mounted in the Barrel between the Solenoid and the iron return yoke. The counters cover polar angles $41° \leq \theta \leq 139°$ (with a dead zone around $\theta = 90°$). The TOF has been used mainly for fast triggering for beam events and cosmics.

Forward Hodoscope (HOF)

The Forward Hodoscope counters are mounted between the End-Cap yoke and the second layer of Forward Muon Chambers. They improve the trigger efficiency for beam event muons, cosmics, and in particular beam-halo muons, which are useful for alignment of the End-Cap tracking detectors, and they provide the first level of the forward muon trigger. The readout (of the hit pattern and time measurements) is combined with that of the Forward Muon Chambers.

2.2.3 Calorimeters

High-density Projection Chamber (HPC)

The High-density Projection Chamber is one of the first large-scale calorimeters to use the time-projection technique. The aim is to measure the charge distribution induced by electromagnetic showers and hadrons with high precision in all coordinates.

Showers with energies up to 50 GeV may be measured, but the HPC is also sensitive to a minimum ionising particle (MIP), which may be identified either by its low total energy deposition or by the small number of hit points recorded.

144 separate modules (segmented by 24 in azimuth and 6 in z) are mounted inside the Solenoid, covering polar angles $43° \leq \theta \leq 137°$. Gaps between modules are 1 cm, except for a gap of 7.5 cm at $z = 0$[8]. Time projection is achieved by using the lead converter as an electric field cage; the ionisation charge of showers and tracks is extracted onto a single proportional wire plane at one end of each HPC module. The gas gaps are 8 mm.

The ionisation is sampled 9 times in the radial direction, which is over 18 radiation lengths deep. A granularity of 4 mm in z and $1°$ in ϕ is achieved. The identification efficiency for MIP's is discussed in Chapter 5.

Forward Electromagnetic Calorimeter (FEMC)

The FEMC consists of two 5 m diameter discs, one in each end-cap, covering polar angles $10° \leq \theta \leq 36°$. Each disc contains 4532 lead glass blocks 20 radiation

[8] This gap is covered by scintillator/lead sandwich blocks which provide crude shower information and about 97% efficiency for a MIP.

lengths deep, of size 5 cm×5 cm (or 1° × 1°) in the shape of truncated pyramids which point towards the interaction region.

Hadron Calorimeter (HCAL)

The HCAL is a sampling gas detector incorporated in the magnet yoke. It consists of streamer tubes inserted into 2 cm slots between 5 cm iron plates.

In the Barrel the HCAL is segmented by 24 in ϕ, as is the HPC , but the sectors are offset by 7.5° with respect to HPC sectors. The streamer tubes are 9 mm×9 mm cells containing one anode wire each. There are 20 layers of detectors in the Barrel (19 in the End-Cap). Pads of 5 adjacent layers (4 or 7 in the End-Cap) are combined into a 'tower' which points towards the interaction region, so that there are typically 4 towers in the radial direction (see figure 2.3). Each tower covers an angular region of $\Delta\phi = 3.75°$, and $\Delta\theta = 2.96°$ in the Barrel, ($\Delta\theta = 2.62°$ in the End-Caps). Dimensions of a typical tower in the Barrel are 25 cm × 25 cm × 35 cm.

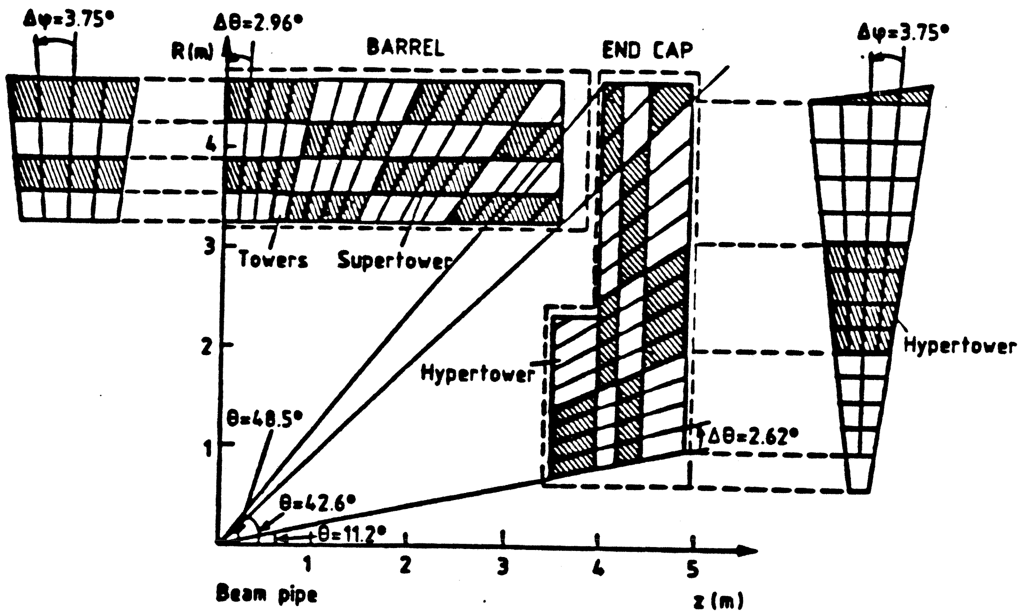

Figure 2.3: Tower Structure of the Hadron Calorimeter

2.2.4 Luminosity Devices

The SAT and the VSAT measure luminosity by counting small angle Bhabha events. Both devices have two 'arms', one each side of the interaction point. The 1990 luminosity measurements used in this thesis (Chapter 6) have been obtained entirely from the SAT measurements.

Small Angle Tagger (SAT)

The SAT is the principal luminosity monitor. Each arm has a calorimeter with a tracker in front.

The **tracker** is foreseen to be three planes of large area silicon detectors at $|z| = 203, 216, 230$ cm, each with an inner radius of 10 cm. The sensitive region is $2.49° \leq \theta \leq 6.88°$. The tracker is expected to give a resolution of $\sigma_\theta = 1.5$ mrad and to define the inner acceptance radius to an accuracy of about 40 μm. This is important as the Bhabha cross-section at small angles is a very rapidly varying function of θ. Two planes of the tracker were installed in one arm at the beginning of 1990, but only preliminary results exist. In the other arm, a lead mask (10 radiation lengths thick) has been used in 1989 and 1990 to define the inner acceptance radius for the calorimeter to better than 100 μm (see figure 2.4). The mask was introduced in 1989 as the tracker was unavailable and was retained in 1990 as it proved so successful. Additional lead masks were added to cover the vertical junction between the two half barrels of the calorimeter (these masks are referred to as the "butterfly wings").

The SAT **calorimeter** covers polar angles $2.46° \leq \theta \leq 7.73°$. It consists of alternating layers of lead sheets (0.9 mm thick) and plastic scintillating fibres, aligned *parallel* to the beam. The total thickness is 28 radiation lengths.

The accepted cross-section is about 30 nb. The event selection and systematic uncertainties are discussed at length in [22]. The systematic error on the absolute luminosity in DELPHI is discussed in section 6.2.1.

Very Small Angle Tagger (VSAT)

Each arm of the VSAT is mounted 7.7 m from the interaction point, covering polar angles $0.29° \leq \theta \leq 0.40°$. In each arm there are two rectangular tungsten-silicon calorimeter stacks , 24 radiation lengths deep, 5 cm high, 3 cm wide and

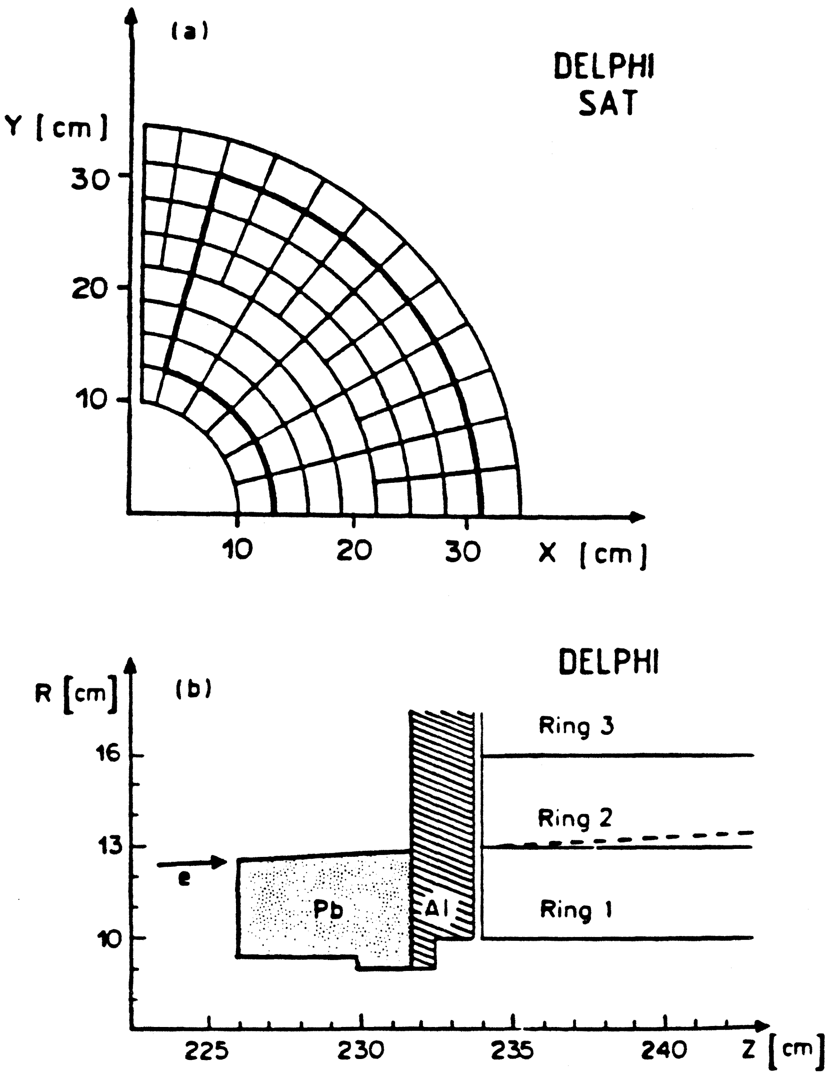

Figure 2.4: Two views of the DELPHI SAT. The lead mask in (b) is in one arm only and is used to define the inner acceptance radius.

10 cm long. The blocks are mounted to both horizontal sides of the (elliptical) beam pipe, covering azimuthal angles $315° \leq \phi \leq 45°$ and $135° \leq \phi \leq 225°$.

The accepted cross-section in this very forward region is about 400 nb, leading to a Bhabha rate 10 times the Z^0 rate on the peak. Therefore, the VSAT is suitable for fast monitoring of relative luminosity and machine operation. Absolute luminosity determination is limited by uncertainties in geometry and in theory.

2.2.5 Ring Imaging Cherenkov Counters (RICHs)

DELPHI is the only LEP experiment to include RICH detectors. Their purpose is to provide good hadron identification (particularly π/K and K/p separation) over most of the momentum range by a combination of gas and liquid radiator.

The RICHs are not used for the analysis in this thesis, but we include a brief description of their design for completeness.

Cherenkov radiation is electromagnetic radiation emitted in a forward direction by charged particles if their velocity βc exceeds the light velocity in the medium traversed by the particle (light velocity=c/n where n is the refractive index of the medium). The angle θ_c of the emitted Cherenkov radiation relative to the particle trajectory depends on the particle's *velocity*:

$$\cos\theta_c = \frac{1}{\beta n}. \tag{2.5}$$

The velocity measurement may be combined with the measured momentum to obtain the particle's rest mass. The Barrel RICH (BRICH) is a cylinder of length 3.5 m with inner and outer radii of 123 cm and 197 cm respectively, divided at $z = 0$ by a central support wall 6.4 cm thick. Cherenkov photons produced in the liquid radiator (C_6F_{14}) are detected in drift tubes, which act as time-projection chambers with readout chambers at the outer ends. Photons produced in the outer gas radiator (C_5F_{12}) are reflected by parabolic mirrors and focussed into a ring in the same drift tubes. Heating is necessary for the gas radiator as the boiling point of C_5F_{12} is 30° C at one atmosphere, so in order not to risk disturbing the other DELPHI detectors the RICH was not operated with the correct gas mixture in 1990.

All BRICH components were installed for the 1990 run except for the drift tubes in one half-cylinder. Rings have been seen from the *liquid* radiator (the average number of photo-electrons per ring from nearly perpendicular tracks is 12).

The Forward RICH has been mounted in one End-Cap, but all items (including electronics) have been delayed because priority was given to the BRICH.

2.2.6 Muon Chambers

The Barrel Muon Chambers (MUB) will be described in detail in Chapter 3. The End-Cap Muon Chambers (MUF) are drift chambers operated in limited streamer mode. They are mounted in two planes: one plane is inside the yoke behind at least 85 cm of iron of the HCAL; the second plane is behind a further 20 cm of iron and the HOF. Each plane is arranged in four quadrants, which consist of two crossed layers each of 22 drift chambers. The sensitive volume of each chamber is $434.4 \times 18.8 \times 2.0$ cm^3. Each chamber has one anode wire along the central axis and a graded cathode, with one cathode section (facing the anode) being a flat solenoidal delay line. Coordinates are derived from the anode drift time and (less accurately) from the delay line propagation times to both ends. The anode is at around 5000 V, and the central cathode is held at ground.

2.2.7 The Readout and Trigger System

The DELPHI Data Acquisition System (DAS) is based on the FASTBUS [23] standard. Some features of the design are described in detail in Appendix B.

Briefly, the aim is to read out and record events at rates of up to a few Hz. Beam Cross Over (BCO) occurs every 22 μs (i.e. 45 kHz). To free the detectors' front end buffers introduces a dead-time of 350 μs, so it is clearly impossible to read-out every beam crossing. The aim is to trigger on the small percentage of interesting events, with a high and precisely known efficiency. A four level trigger system was designed for DELPHI to cope with the highest luminosities and background rates. During 1989 and 1990, only the first level and some important elements of the second level trigger were implemented. The rates were about 2-3 Hz after the second level.

The first and second level trigger decisions are taken after 3 and 40 μs respectively. In the second level, detectors with long drift times (e.g. the TPC, whose drift time is up to 22 μs) are used. One or two BCOs will have been missed. The third and fourth level triggers will be asynchronous with BCO, with processing times of 30 ms and 300-500 ms respectively.

It is useful to have several independent triggers for the same class of events, so that the trigger efficiency may be calculated from real data. The main trigger components are:

- Track Trigger: the forward track trigger uses data from FCA and FCB. The first level Barrel track trigger uses data from the ID and OD and looks for a correlation between the two detectors in the R-$R\phi$ plane (acceptance angles are $42° \leq \theta \leq 138°$) . The TPC provides a second level track trigger using an 'OR' of the ID and OD signals as first level pre-trigger.

- Muon Trigger: a muon signature is provided by MUB and MUF. A hit in the TOF or HOF is required to reduce the rate. MUF is used only at the second level due to the long drift times (up to 14 μs, as opposed to a maximum drift time of about 2.5 μs for the MUB). The muon trigger was implemented, for the End-Caps only, in July 1990.

- Electromagnetic Energy Trigger: this trigger looks for electromagnetic showers in the HPC and FEMC. The threshold was set to 2 GeV in the Barrel and 3.5 GeV in the End-Caps.

- Hadron Energy Trigger: this trigger, which looks for hadronic energy deposited in the HCAL, was not an active trigger in 1989 and 1990 runs.

- Bhabha Trigger: this is the e^+e^- trigger at small angles. Back-to-back energy depositions of $\geq$ 13 GeV are required in the two arms of the SAT.

- Other triggers: several other triggers were available in the Barrel region including a TOF back-to-back trigger, a TOF majority trigger, an ID/OD majority trigger, and a trigger ('SCOD') which combined information from the TOF and the OD.

The triggering of muon-pair events is discussed further in Chapter 5.

Chapter 3

The Barrel Muon Detector

The Barrel Muon Detector comprises 1372 single-wire proportional drift chambers, positioned within and outside the iron return yoke of the DELPHI solenoid. In this chapter we describe the design of the chambers and the overall geometry of the detector. We also describe how the chambers were tested and calibrated before installation in DELPHI, as this is relevant to understanding their performance in the LEP physics runs.

3.1 Principles of Drift Chambers

The principles of operation of drift chambers are described in detail by Sauli [24]. A charged particle ionises the gas along its path by incoherent Coulomb interactions, producing about 120 ion pairs per centimetre in argon under normal conditions for a minimum ionising particle, for example. The liberated electrons quickly lose their energy in multiple collisions with gas molecules and assume the average thermal energy of the gas[1]. However, under the influence of an applied electric field, there is a net movement of charge along the field direction, which occurs with 'drift velocity' v_d.

In moderate fields, electrons collide elastically with the molecules of the gas in the chamber. Owing to their small mass, electrons can substantially increase their energy between collisions. In a simple formulation, due to Townsend, one can write the drift velocity v_d in an electric field $\mathbf{E}$ as

$$v_d = \frac{\epsilon \mathrm{E}\tau}{2m_\epsilon} \tag{3.1}$$

where τ is the mean time between collisions and ϵ and m_ϵ are the charge and mass of the electron.

[1] They may also be neutralised by an ion or become attached to an electronegative molecule, but the probability of attachment is essentially zero for all noble gases.

Assuming that the electron's drift velocity is smaller than its non-directional velocity v (due to its thermal energy) we may write

$$\tau = \frac{\lambda(\epsilon)}{v} \tag{3.2}$$

$$= \frac{1}{v}\frac{1}{\mathrm{n}\sigma(\epsilon)} \tag{3.3}$$

where ϵ is the electron's energy, $\lambda(\epsilon)$ is the mean free path between collisions, n is the number of gas molecules per unit volume, and $\sigma(\epsilon)$ is the collision cross-section [2]. Since n is proportional to pressure P divided by temperature, we expect the drift velocity to depend on the so-called 'reduced electric field', that is:

$$v_\mathrm{d} \propto \frac{\mathrm{E}}{\mathrm{P}}. \tag{3.4}$$

In a drift chamber, the electric field is shaped to be as uniform as possible throughout most of the chamber. Electrons very quickly reach a stable drift velocity, thus giving a simple linear relationship between drift time and distance.

The anode is formed by a thin metal wire, so that the field is a maximum at its surface and falls off rapidly as r^{-1} in its immediate vicinity. In the high-field region within a few wire radii (where E is a few kilovolts per centimetre) electrons receive enough energy between collisions to produce inelastic phenomena: that is, excitations and ionisation of the gas. An ion pair is formed and the primary electron continues on its path; a drop-like avalanche develops with all the electrons in the front and the ions behind. This so-called 'avalanche multiplication' boosts the amplitude of the signal on the anode by several orders of magnitude.

Adding small amounts of another gas to argon can dramatically change the drift properties. In an ideal gas mixture the electron drift velocity v_d shows only weak field dependence ('plateaus') at suitable electric fields and falls off slowly below this plateau. The drift velocity at the plateau should be appropriate to the needs of the experiment and should be insensitive to likely fluctuations in the content of contaminants such as oxygen or water vapour. The gas mixture must also satisfy safety requirements by having low flammability.

[2]The collision cross-section σ varies strongly with E for some gases, going through maxima and minima due to quantum mechanical effects which occur when the electron wavelength approaches those of the electron shells (Ramsauer effect).

3.2 The Barrel Muon Detector (MUB)

3.2.1 The Drift Chamber

Schematic views of a Barrel Muon drift chamber are shown in figure 3.1. The dimensions of the internal gas volume are $1.5 \times 20.0 \times 365.0$ cm for a standard chamber (other chambers differ only in the length of the longest side).

A single anode wire runs along the central longitudinal axis, made of gold-plated tungsten with a 47 μm diameter and characteristic impedance of 500 Ω. It is supported at roughly metre intervals by plastic inserts called 'spiders'. Signals propagate along the anode wire at about 20 cm/ns.

Two sets of twelve parallel, longitudinal copper strips, 0.4 cm wide, are glued on to 0.28 cm thick plastic sheets on the two largest inner surfaces of the chamber. These strips hold the graded cathode voltage ('the grading') , which is designed to give an approximately uniform electric field across the chamber. On each surface there is an additional central strip of width 1.5 cm , which holds the maximum cathode voltage. One of these two central strips also acts as a 'delay line' . It is composed of insulated copper windings, with characteristic impedance of around 600 Ω. The cloud of charge from the avalanche at the anode induces a pulse on the delay line which propagates along it to both ends at about 0.5 cm/ns.

A chamber is designed to produce three signals when a charged particle passes through it: one anode signal and one signal from each end of the delay line.

The nominal anode voltage is +6.15 kV and the grading voltages range from +4.00 kV on the central strip to ground at the edge of the chamber. Since the internal width of half a chamber is 10.0 cm, the mean drift field is 400 Vcm^{-1}.

The chambers are operated in proportional mode. During tests in Oxford on a cosmic ray test-rig, the chambers were flushed with a gas mixture of 88% argon, 7% methane and 5% carbon dioxide by volume (as recommended in [25]), with a normal flow rate through each chamber of about 10 cm^3/min. At DELPHI a mixture of $Ar/CH_4/CO_2$ in the proportions 85.5/8.5/6.0% has been used.

3.2.2 Geometry of the Detector

The chambers are bonded together in 'modules' of either 7 or 14 chambers. At the plane of the Muon Chambers, the DELPHI Barrel measures roughly 10 m in

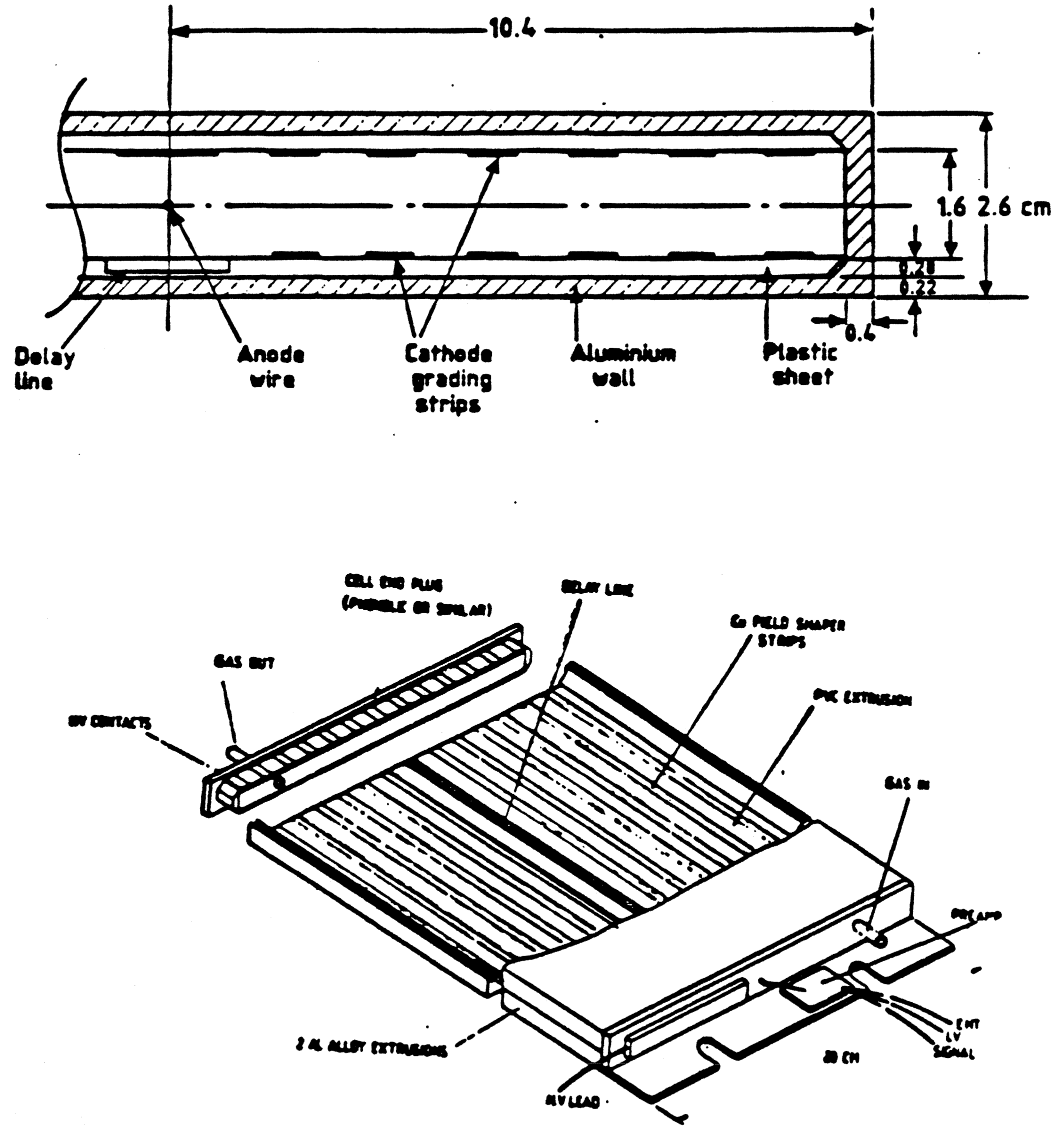

Figure 3.1: Schematic View of a Barrel Muon Chamber

diameter and 8 m in length. There are three sets of Muon Chamber modules, called the 'Inners', the 'Outers' and the 'Peripherals'. They are mounted in concentric polygons around the DELPHI z-axis, as illustrated in figure 3.2. A single chamber covers half the length of the Barrel, so that the detector naturally divides into two 'hemibarrels', with a gap of about 3.0 cm between 'positive-z' and 'negative-z' modules. Each hemibarrel is subdivided in azimuth into 24 sectors, so that each sector subtends 15° in ϕ. A standard sector contains one Inner, one Outer, and one Peripheral module[3]. The radial distances from the DELPHI z-axis to the base of a module in the Inner, Outer, and Peripheral layer are nominally 445.5 cm, 479.3 cm , and 532.0 cm respectively.

Inner modules are installed within the iron of the Hadron Calorimeter (after about 90 cm of iron). They contain 14 drift chambers stacked in three layers: 5 chambers in layer 1 (the nearest layer to the centre of DELPHI), 4 in layer 2, and 5 in layer 3 . In common with Outer and Peripheral modules, layers are staggered by half a chamber width in order that the natural left-right ambiguity that is characteristic of drift chambers may be resolved by looking at the reconstructed hits in the adjacent layer [4]. However, because of the geometry of the detector and inefficiencies, this left-right ambiguity is not always solved. The third layer of the Inners is spare, and chambers in this layer are not on high voltage (and not read out) unless there is a fault with one of the overlapping chambers in the first two layers.

Outer and **Peripheral** modules contain seven chambers (4 + 3) and are mounted on the outside of DELPHI, behind a further 20 cm or so of iron. Peripheral modules are displaced by 7.5° in ϕ relative to the Outers of the same sector, in order to cover the gaps in the Outers for cables and pipes. Although it is possible for a muon to pass through a total of six layers of chambers, a more

[3]The existence of large supports for the Solenoid and its return yoke (the 'magnet legs') means that extra modules are required in the Outers and Peripherals. There are thus two additional sectors (conventionally called sectors 49 and 50) which consist of Outer and Peripheral modules only.

[4]If the measured drift distances in adjacent layers A and B are d_A and d_B then we expect

$$d_A + d_B \approx hwid \tag{3.5}$$

where $hwid$ is half the width of a chamber (10.4 cm) and the equality holds in the limiting case that there is no measurement error on the drift distances and the track traverses the chambers exactly at right angles to the drift direction.

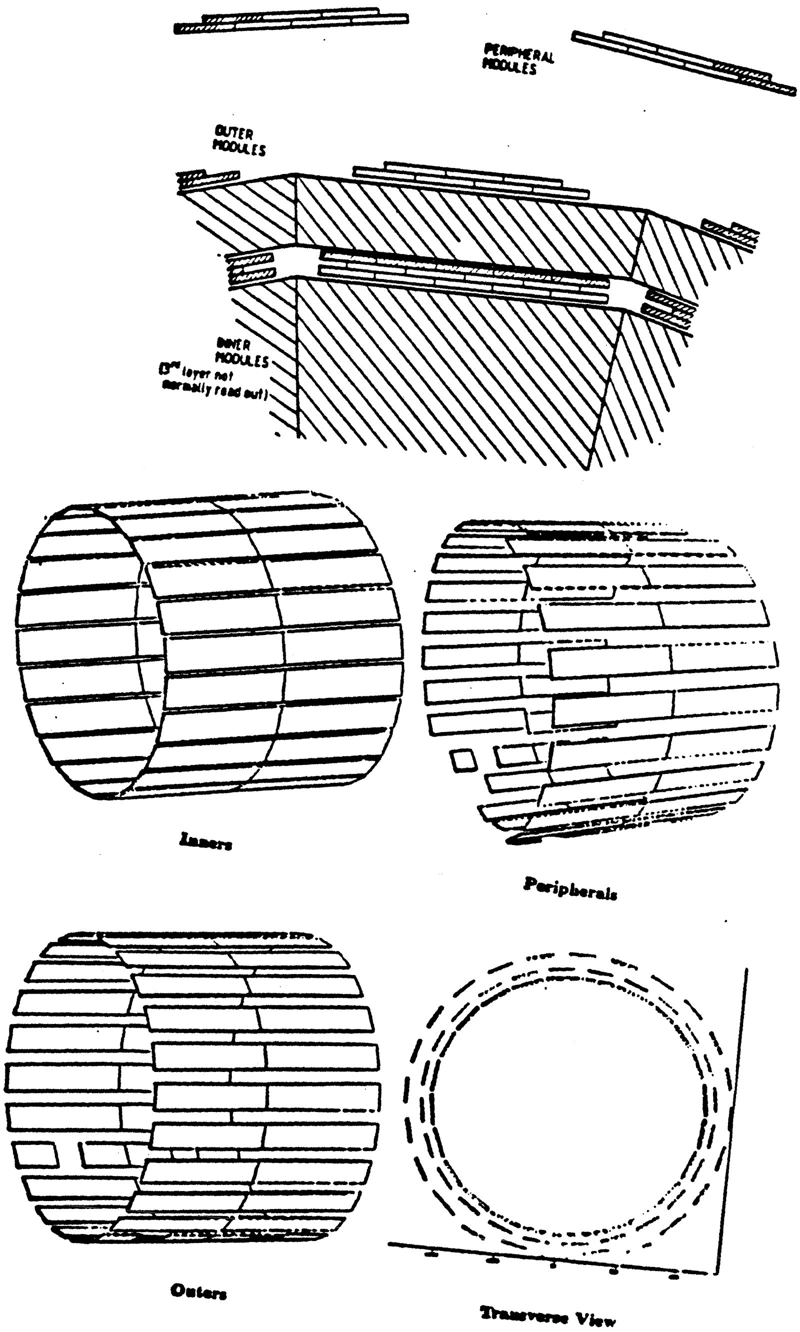

Figure 3.2: The Barrel Muon Detector

typical upper bound is four. The most likely combinations of modules with hits are Inners+Outers and Inners+Peripherals. For some ϕ angles we expect hits in the Peripherals only.

If only one or two hits are demanded, there is little MUB dead space in ϕ. The dead space in the polar angle θ is highly localised, being due to the gap between chambers at $z = 0$ ($\theta = 90°$). In addition, polar angles around $\theta = 45°$ are not covered by either the Barrel or the End-Cap Muon Detectors.

In summary, there are 24 standard sectors in each hemibarrel (48 in total), each comprising $14 + 7 + 7 = 28$ chambers. In addition, there are two anomalous sectors around the magnet legs, each containing Outer and Peripheral modules only (14 chambers). Hence, there is a total of 1372 chambers installed in DELPHI.

3.2.3 Associated Hardware

The Barrel Muon front-end electronics consist of NIKHEF hybridised amplifiers with gains of 20 mV/μA, differentially feeding into LECROY MVL407 discriminators, with thresholds set to 100 mV. These amplifiers and discriminators are assembled in 50 electronically screened boxes mounted on the outside of the DELPHI Barrel.

There is one amplifier/discriminator box per sector. The discriminated signals are then fed to the nearer of two counting rooms (which are called **B2** and **D2**) which house the MUB electronics, where they are all multiplexed six-fold before being digitised.

Figure 3.3 show schematically the Barrel Muon electronics in one counting room and its integration in the DELPHI readout system (see also Appendix B for a more detailed discussion).

In both B2 and D2, MUB has one FASTBUS crate, which houses several modules including 7 Time-to-Digital Converters (so-called 'LEP Time Digitisers' or 'LTDs' [26]) and one Hit Latch Buffer (HLB). The HLB stores one bit for each input channel of the multiplexer indicating whether or not a signal occurred on that channel (i.e. on that anode or delay line end) in that event. Six signals are fed into each LTD channel, so the HLB information is used to indicate which anode or delay line actually fired. Of course, if signals arrive from more than one of the six

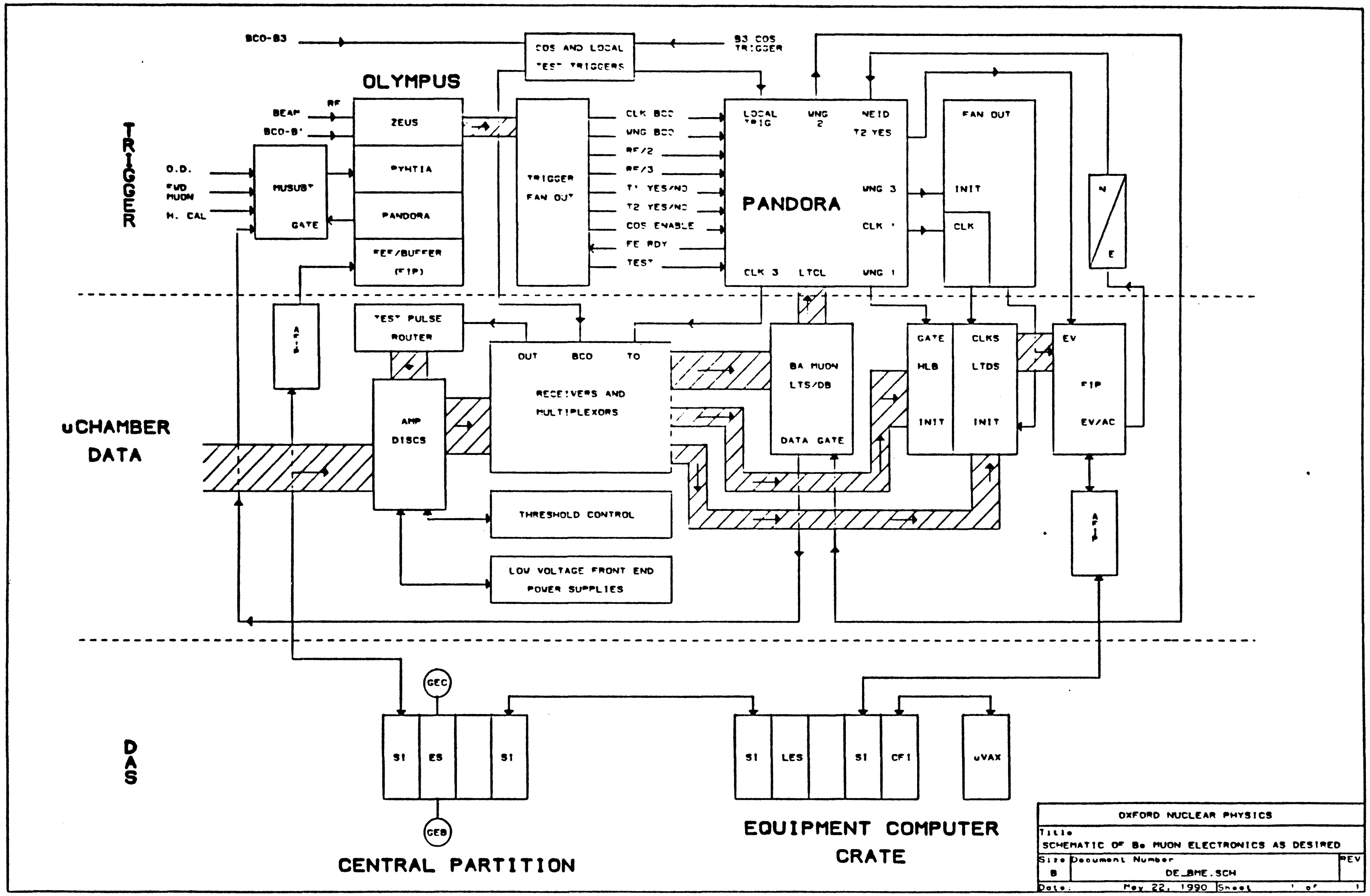

Figure 3.3: Schematic diagram of the Barrel Muon Electronics

possible sources, there will ambiguity as to which LTD time corresponds to which signal, but the probability of this happening is very small as very few chambers fire in any one event, and the signals are 'shuffled' before being multiplexed according to strict rules[5].

LTD time measurements are in ≈ 2 ns bins over a dynamic range of 32.7 μs. Each LTD has 48 channels, each with multihit capability (with a dead time of about 70 ns between digitisations).

The high voltage for the chambers is distributed from four 'CAEN' crates. Each CAEN channel supplies the anodes or gradings for one sector via 50 distribution boxes mounted on the Barrel. Hardware and software interlocks link the anodes and gradings of a sector so that the voltage difference between the anode and the central cathode is not allowed to exceed safe values. The supply is monitored and controlled by a special program running on the Equipment Computer[6]. For example, when a sector's total anode current exceeds a strict, pre-defined threshold , the high voltage on the anode and gradings for that sector is immediately ramped down. After a short pause, anode and grading are slowly ramped up again. The time during which the chambers are not sensitive (some five minutes) is stored in a database for possible access by the offline analysis programs. High voltage is also removed automatically when there is a problem with the gas supply.

3.2.4 Measurement of Space-points

By timing measurements, the Muon Chambers measure two quantities:

1. **drift distance**: this is obtained from the time of the hit on the anode wire and the assumed time of passage of the particle through the chamber (which is very soon after the beams cross for a particle originating from a beam event);

2. **delay line distance**: this is usually obtained from the *difference* in the times measured at the two ends of the delay line.

[5]For instance, no signals from different chambers in the same sector are fed to the same time digitiser channel.

[6]Communication to the CAEN is via a system based on the G64 standard implemented in special MAC crates.

If suitable signals are recorded on the anode and both delay line signals, the hit is referred to as a 'triplet'. A 'doublet' is a hit reconstructed with the anode signal and one delay line signal. The delay line distance resolution is worse for a doublet, where it depends on absolute time delays in the cables, trigger etc., rather than differences in delays.

The z coordinate in the DELPHI coordinate system is obtained from the delay line distance, while R and $R\phi$ depend on the drift distance. MUB measurement errors on delay line distance and drift distance give rise to the same errors on DELPHI z and $R\phi$ respectively (to a good approximation).

The Muon Detector is designed to select muons by recording two space points on the tracks of those charged particles which penetrate the Hadron Calorimeter over its full depth. Hits in two chambers approximately 30 cm apart can be used to obtain a measurement of the particle's direction at the Muon Chambers, which is useful in rejecting against hadronic punchthrough. The useful precision of this angle is limited by multiple Coulomb scattering.

Target resolutions of 1.0 mm in drift distance and 10 mm in delay line measurement were chosen for high muon identification efficiency and tracking for muons with momenta up to around 100 GeV (in LEP200).

The drift velocity should be fast enough to allow anode signal information to be used in the DELPHI first level trigger decision (which is taken after 3 μs) without being so fast that drift distance resolution is sacrificed. v_d varies between chambers and over time, but it is usually ≈ 4.7 cm/μs, which leads to a maximum drift time of ≈ 2.1 μs). For 1 mm resolution, v_d must be known to around 1% and the time of passage of the ionising particle relative to the digitised time must be known to about 20 ns for every chamber.

For the z-coordinate, the delay is about 1.8 ns/cm, so the time of arrival of the signals at each end of the chamber should be known to about 2 ns. One requires good knowledge of the difference in cable delays between the two ends of the delay line, and good time-digitiser performance. The resolution is also sensitive to variations in the signal propagation velocity along the delay line.

To achieve the targets on spatial resolution, drift and delay line characteristics had to be measured to a high precision for each individual chamber.

3.3 The Cosmic Ray Test-Rig

To test and calibrate chambers under carefully controlled conditions with large statistics (usually tens of thousands of events), and to ensure that only good quality chambers were installed in DELPHI, all chambers were tested on a specially designed cosmic ray test-rig soon after they were assembled[7].

The test-rig comprised 25 'calibration' chambers, whose characteristics were well-known and stable, and 20 newly assembled 'test' chambers. A diagram of the test-rig coordinate system is shown in figure 3.4 (x is the drift coordinate and z the distance along the delay line, with $(z, x) = (0, 0)$ being on the anode wire halfway along the chamber). All chambers are between two layers of scintillators. The hardware trigger consisted of a coincidence between any scintillator on the top layer and any in the bottom layer, so that all chambers received an approximately equal flux of roughly vertical cosmics. LECROY Time-to-Digital Converters (TDCs) were started by the trigger signal and stopped if there was a signal on that channel.

3.3.1 Measurement of Chamber Constants

The anode and delay line times are related in the following way:

$$\begin{aligned} t_{\mathrm{A}} &= t_0^{\mathrm{A}} + t_{\mathrm{prop}}^{A}(z) + t_{\mathrm{drift}}(x) \quad \text{(anode)} \\ t_{\mathrm{N}} &= t_0^{\mathrm{N}} + t_{\mathrm{prop}}^{\mathrm{N}}(z) + t_{\mathrm{drift}}(x) \quad \text{(delay line near)} \\ t_{\mathrm{F}} &= t_0^{\mathrm{F}} + t_{\mathrm{prop}}^{\mathrm{F}}(z) + t_{\mathrm{drift}}(x) \quad \text{(delay line far)} \end{aligned} \tag{3.6}$$

Here t_{prop} is the time taken for the pulse to propagate along the wire/delay line, t_{drift} is the drift time, and $t_0^{\mathrm{A,N,F}}$ are offsets, chosen such that the signal times became zero for a particle of zero drift distance (or zero drift *and* delay line distance for the delay line TDCs).

The Drift Distance

The anode times obtained from the test chambers were fitted to the following equation

$$x = \mathrm{a}_0 + \mathrm{a}_1 t_{\mathrm{drift}} + \mathrm{a}_2 z t_{\mathrm{drift}} + \mathrm{a}_3 t_{\mathrm{drift}}^2 \tag{3.7}$$

[7]The design and maintenance of the test-rig and the associated software was the work of many members of the Oxford group.

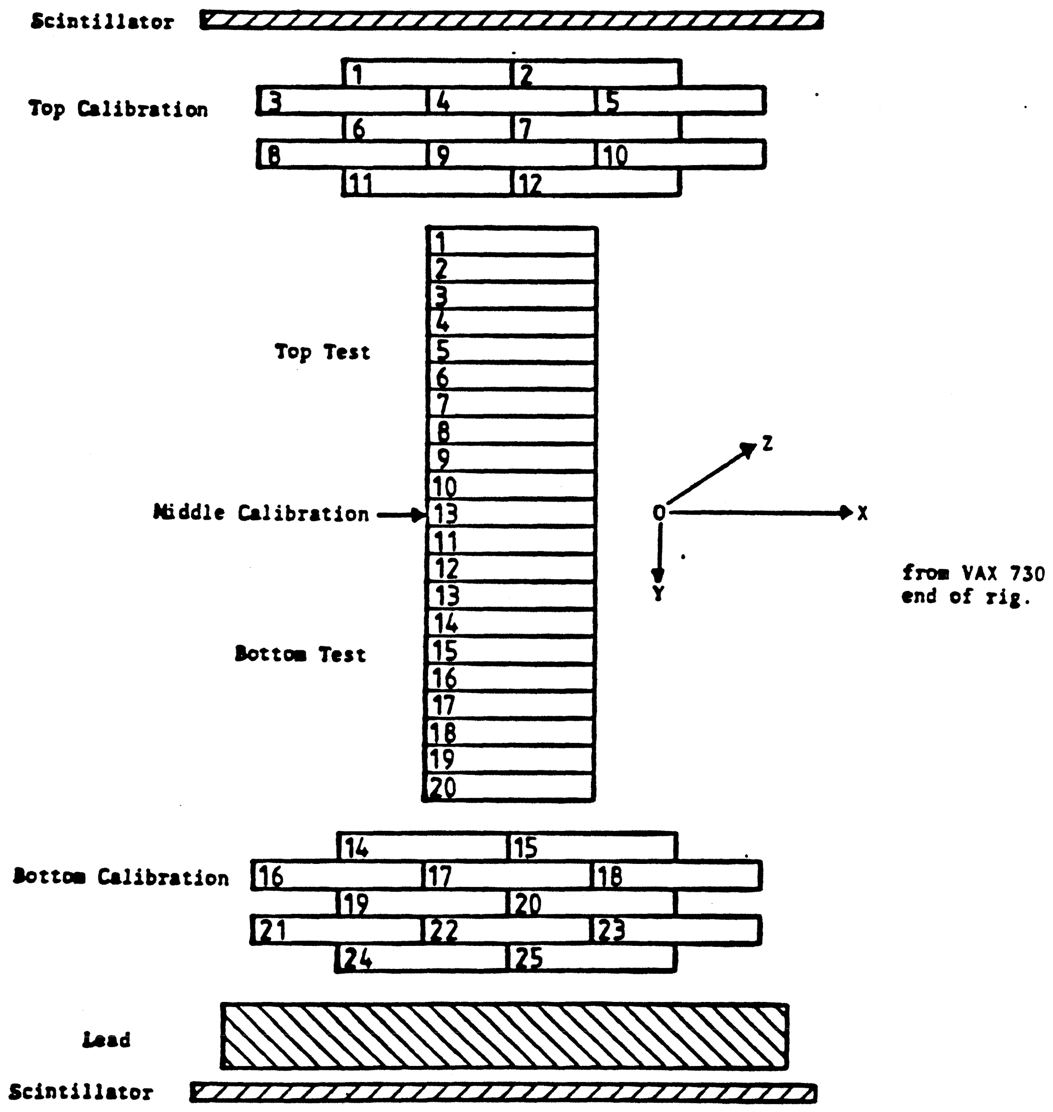

Figure 3.4: Schematic View of the Cosmic Ray Test-Rig

Note that a quadratic in $t_{\rm drift}$ is used in order to attempt to parameterise the effect of non-linear potential gradients around the anode wire and near the edge of the chamber. A linear dependence on z is assumed[8]. The coefficient $\rm a_1$ is usually referred to as the velocity, and $\rm a_2$ as the 'slope'.

On the test-rig, x and z were obtained from the calibration chambers, and $t_{\rm drift}$ was obtained from measuring $t_{\rm A}$. The parameters $\rm a_0, a_1, a_2, a_3$ were obtained using a least-squares fit for all the hits; that is, by minimising with respect to variations in these three parameters the sum:

$$\sum_{i}^{n} \left[x - (\mathrm{a}_0 + \mathrm{a}_1 t_{\rm drift} + \mathrm{a}_2 z t_{\rm drift} + \mathrm{a}_3 t_{\rm drift}^2)\right]^2 \tag{3.8}$$

where the summation is over all the hits in the chamber.

The relative importance of the four coefficients is illustrated in figure 3.5.

The Delay Line Distance

A new variable $t' = (t_{\rm N} - t_{\rm F})/2$ was defined and a least-squares fit was performed for all hits to the relation:

$$z = \mathrm{b}_0^T + \mathrm{b}_1^T t' + \mathrm{b}_2^T t'^2 + \mathrm{b}_3^T t'^3 + \mathrm{b}_4^T t'^4. \tag{3.9}$$

The T superscript indicates 'triplet'. Two further sets of five parameters were obtained for doublets, which only used the far (near) delay line signals (making 15 delay line parameters per chamber in total).

The term in t' is the dominant one, and one may (loosely) refer to $\rm b_1$ as the delay line velocity. The relative importance of the five triplet coefficients is illustrated in figure 3.6.

Time Sums

The 'time sum' t_s is defined in the following way:

$$t_s = (t_{\rm N} - t_0^{\rm N}) + (t_{\rm F} - t_0^{\rm F}) - 2(t_{\rm A} - t_0^{\rm A}) \tag{3.10}$$

$$= t_{\rm prop}^{\rm N} + t_{\rm prop}^{\rm F} \tag{3.11}$$

[8]This was shown to hold by dividing the test chambers into ten equal sections in z and measuring the drift velocity in each tenth.

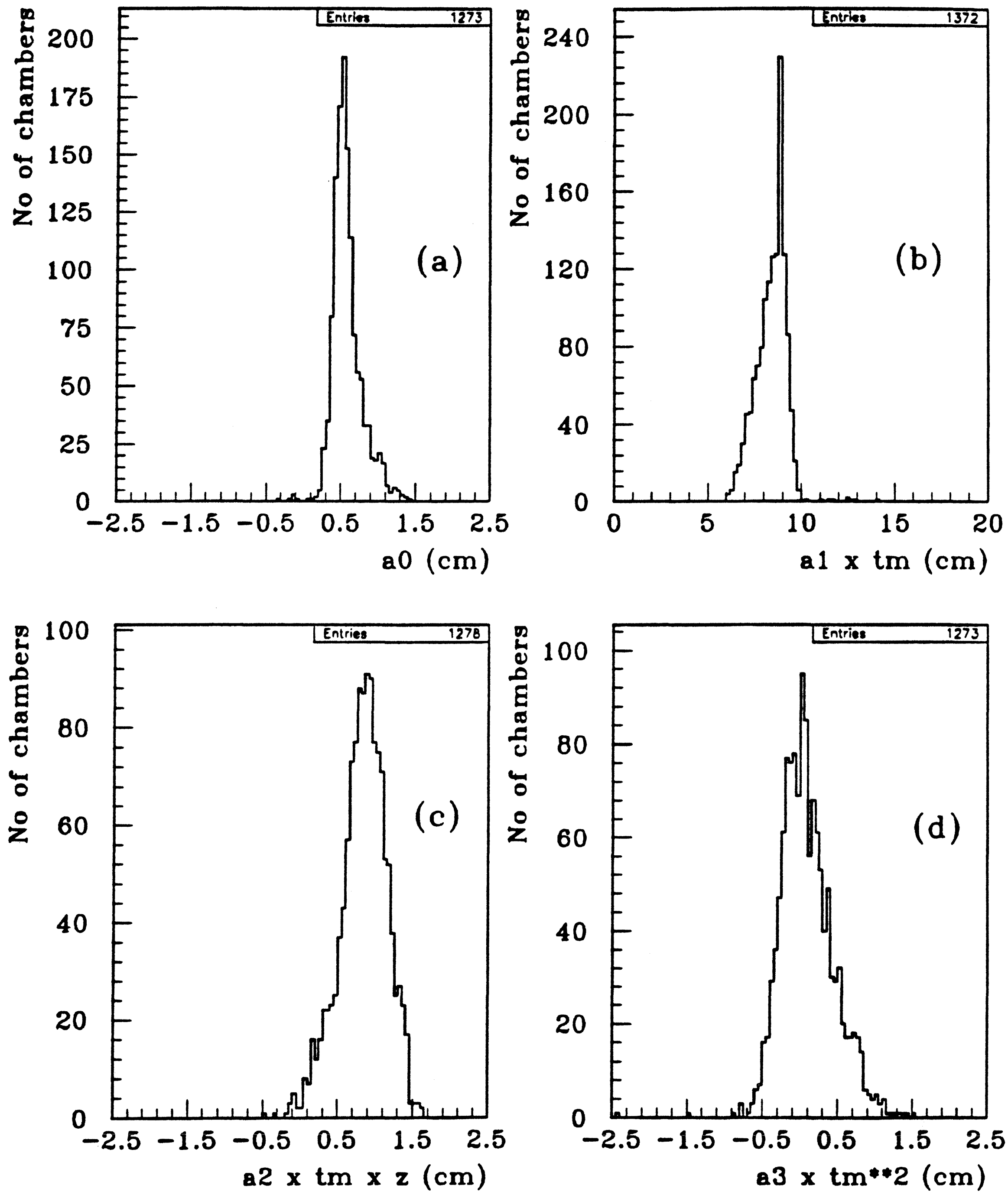

Figure 3.5: Drift Distance Coefficients: (a) a_0;(b) $a_1 \times t_m$; (c) $a_2 \times t_m \times z_m$; (d) $a_3 \times t_m^2$, where t_m is 2.2 μs (approximately the maximum drift time) and z_m is the maximum z distance from the centre of the chamber (that is, half the chamber's internal length). The values are from the DELPHI database for chambers which were installed at DELPHI during 1990.

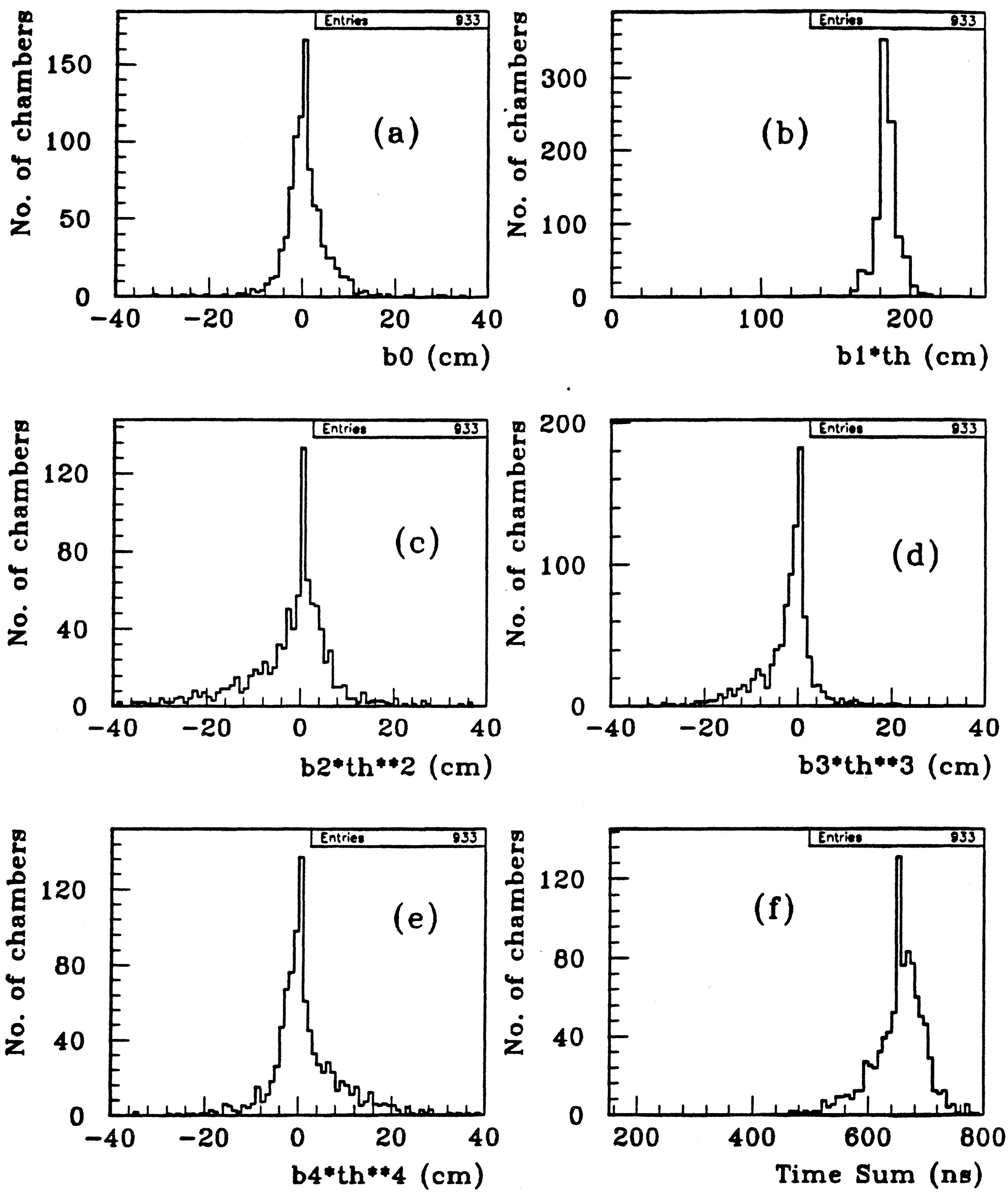

Figure 3.6: Triplet Delay Line Coefficients and Time Sums: (a) b_0; (b) $b_1 \times t_h$; (c) $b_2 \times t_h^2$; (d) $b_3 \times t_h^3$; (e) $b_4 \times t_h^4$; (f) time sum t_s. Here, $t_h = 0.5 \times t_s$. The values are from the DELPHI database for chambers which were installed at DELPHI during 1990 and were of internal length 365.0 cm.

Notice that the time sum is simply the time taken for a signal to travel the length of a delay line; therefore, it represents a measured quantity that is a *constant* for all real hits for a particular chamber.

The average rms spread of the time sums in one chamber was found to be about 5 ns on the test-rig. The time sum is therefore an extremely powerful way of identifying a triplet from an array of digitised times (this is particularly useful as signals are multiplexed).

Test-rig time sums are stored on the MUB database. The measured values for all standard length chambers are shown in figure 3.6(f). For a triplet at DELPHI to be reconstructed, it is required to have a time sum close to the database value for that chamber.

Chamber Efficiency

Figure 3.7 shows the chamber efficiencies as measured on the test-rig. The efficiency is close to 100% in live areas. There are dead areas near the chamber walls and close to the spiders.

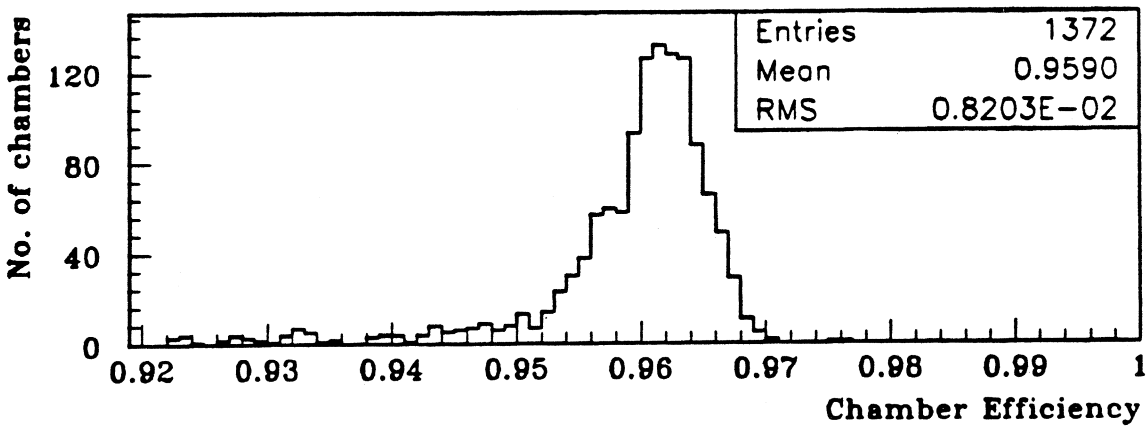

Figure 3.7: Barrel Muon Chamber Efficiencies

3.3.2 Operation of the Test-Rig

Chambers were tested soon after assembly (at a rate of about 20 per week), with a rejection rate of about 14% . Chambers were rejected for inability to hold high voltage reliably, for low overall efficiency ($\leq 90\%$), or for having a very fast or very non-linear delay line (a resolution of better than 2 cm in z was demanded). Most rejected chambers were repaired and returned to the test-rig.

3.3.3 Tests of Drift Characteristics

The test-rig was also used to make tests of the stability of the drift velocity [9]. Note that calibration chambers were on gas continuously.

Definition of Quantities

In these tests only those hits more than 5 mm from the anode wire were considered and the term in t^2_{drift} in equation 3.8 was dropped (i.e. $a_3 = 0$ was assumed).

When a test chamber was first put on gas, a_1 (the velocity at $z = 0$) was usually lower than in calibration chambers. The 'slope' a_2 was typically positive (as can be seen in figure 3.5(c)). This implies that v_d was greater at the end of positive z, which was the gas inlet end. The dependence of the slope on the direction of gas flow was demonstrated by reversing the direction of gas flow on a new chamber, which brought about a switch in the sign of the slope almost immediately.

Development of Velocity and Slope

Breaks in the production schedule offered an opportunity to test chambers over a longer time-scale. For example, over Easter 1988 velocities and slopes of 17 chambers were measured daily for about two weeks. The average values at the start and finish of the test are shown in table 3.1. The slopes decreased for all but one of the test chambers; those for the calibration chambers were at least an order of magnitude smaller. The velocities in the calibration chambers were about 8% larger.

One chamber was tested periodically for six weeks, during which time the velocity increased steadily from 4.43 to 4.76 cm/μs and the slope fell from 193 to 36×10^{-5} μs^{-1}.

[9]Data for these tests were collated by Andrew Pinsent and the author. For more detailed accounts see [27].

	$t = 0$ hours		$t = 320$ hours	
	Velocity cm/μs	Slope $\times 10^{-5}\mu s^{-1}$	Velocity cm/μs	Slope $\times 10^{-5}\mu s^{-1}$
Test Chambers	4.54 ± 0.20	178 ± 45	4.57 ± 0.23	144 ± 38
Calibration Chambers	4.91 ± 0.10	10 ± 13	4.90 ± 0.09	12 ± 12

Table 3.1: Easter 1988 tests: velocities and slopes near start and finish. The errors represent the spread in values over the 17 test chambers or the 25 calibration chambers.

Discussion of Results

A possible explanation of these results is the existence of some contaminant within the gas, whose concentration varies with z and decreases with time. If the contaminant is evaporated off the surfaces which the gas flows over (or 'out-gassed'), there will be a higher proportion of this contaminant furthest from the gas inlet end — therefore the slope implies that it should suppress the drift velocity. This is consistent with the (well-flushed) calibration chambers' having a higher mean central drift velocity.

For the calibration chambers, the drift velocity seemed to be stable to within about 1% and the slope was about 10^{-4} μs^{-1}. This implies a difference in drift velocity between the two ends (365.0 cm apart) of about 0.04 cm/μs, or about 1%. The variation in v_d between calibration chambers was ± 0.10 cm/μs $\approx$ 2%. Since the maximum drift distance is 10 cm, a 2% uncertainty in drift velocity corresponds to a maximum uncertainty on the drift distance of 2 mm.

The tests demonstrated the importance of flushing the chambers well before data taking begins.

3.4 HFM (Beam Test) Experiment

During July and August 1988, three DELPHI detectors were operated together in the H6 beam in the North Area at CERN. One module of the Forward Electromagnetic Calorimeter, one *end-cap* sector of the Hadron Calorimeter, and around thirty Barrel Muon Chambers were employed in what was known as the HFM experiment (**H**CAL,**F**EMC,**M**UB). This was the first test of DELPHI detectors combined. The experiment is described in detail elsewhere [28]. Briefly, some of the aims were:

1. to test the performance of the data acquisition system and to exercise online software and monitoring tasks in a real data taking situation involving more than one detector;

2. to test and calibrate the calorimeters using particles of different types and energies;

3. to estimate rates of hadronic contamination of muon signals and study algorithms for improving the rejection against hadronic punch-through,

4. to gain experience with real data to improve the offline analysis programs.

Data were collected using pion and positron beams of momenta 10, 20, and 40 GeV, and using beam halo muons. The pion beams were heavily contaminated with muons, which were reduced by trigger conditions and by selection cuts in the offline analysis.

MUB modules were placed behind the HCAL module (see figure 3.8) and behind a further 20 cm of iron. Thus, particles encountered a greater depth of iron than they would do when penetrating a Barrel HCAL module. For this reason, the size of the hadronic background in muon signals would be expected to be slightly greater in DELPHI than in the HFM experiment.

In general, all the aims of the HFM experiment were achieved. However, the data collected from the Muon Chambers were degraded by some factors which were peculiar to this experiment, for example:

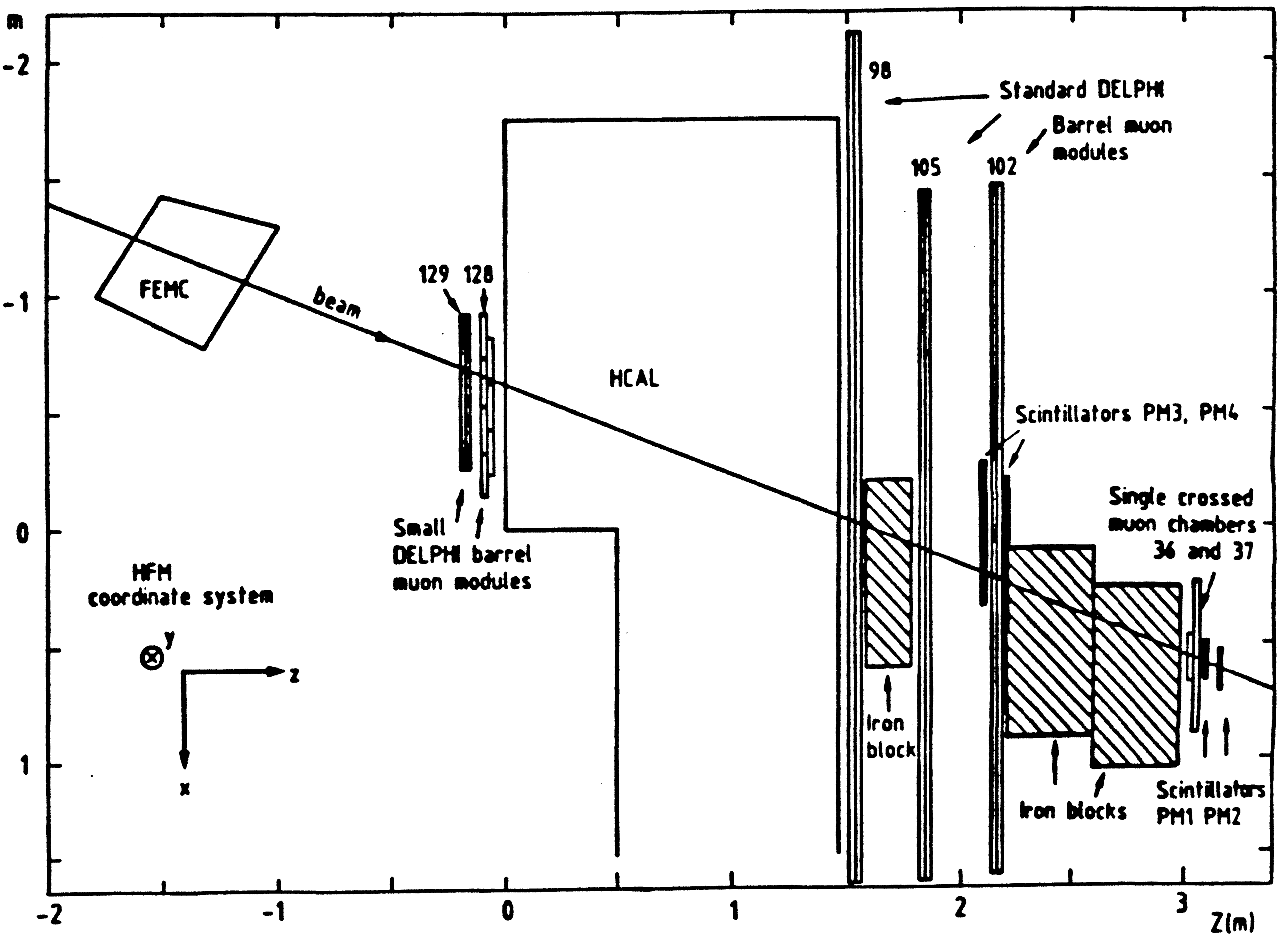

Figure 3.8: Plan View of the HFM Experiment

1. One of the two LTDs used was found to corrupt the four least significant bits of its data words during data transfer, leading to poor time resolution.

2. Drift velocities were typically 25% lower than the values obtained on the test-rig, probably because the chambers had not been sufficiently flushed with gas.

3. The efficiency of some chambers was poor.

3.4.1 Some Conclusions

The results of the HFM experiment are discussed at length elsewhere [28]. It is clear that Muon Chambers should be thoroughly gassed before data-taking for optimal resolution and efficiency. There is a need to make some *in situ* measurements of drift velocities and efficiencies. Gas composition and LTD performance need to be carefully monitored.

The results regarding muon identification efficiency are discussed in Chapter 4.

3.5 Multiple Hits

LTDs were used with the Barrel Muon Chambers for the first time in the HFM experiment. Because of the multihit capacity of these digitisers, data from this experiment were valuable for a high statistics study of the occurrence of multiple hits — that is, several hits (i.e. triplets and doublets) in a single chamber at almost the same time.

Over 30000 beam halo muon 'events' were analysed. We found that secondary pulses ('afterpulses') were seen on the anode in $29\pm4\%$ of hits (the error indicates the root-mean-square variation over the 39 drift chambers). The sequence of pulses was well-structured in time, being separated by about 200 ns, and the delay line times indicated that the secondary hits were generally less than around 15 cm in z from the primary hit [30].

A previous study on the End-Cap Muon Chambers [31] had reached similar conclusions. The following cause was identified: ultra-violet photons are emitted in the avalanche due to the first ionising particle. They may strike the (copper) central cathodes, liberating electrons by the photoelectric effect, which then themselves drift towards the anode and cause a secondary avalanche and an 'echo' hit. This process may be repeated many times.

We studied the occurrence of multiple hits in DELPHI by re-analysing the raw data for 230 muon-pair candidates from April and May 1990 using an adapted version of the MUB online monitoring program MUONLINE [32]. The number of channel hits in which there was at least one afterpulse was $21.1 \pm 1.1\%$ (anode), $16.1\pm1.0\%$ (near delay line), and $16.6\pm1.0\%$ (far delay line). The time differences between the second pulse and the primary pulse on the anode are shown in figure 3.9(a) (the plots for the delay line show similar behaviour). The peak is at about 170 ns (there is a long tail on the high side which is not shown) which is roughly consistent with the expected drift time between the central cathode and the anode[10]. The frequency of occurrence of different numbers of pulses is shown in figure 3.9(b).

[10]The minimum distance between the anode and a part of the central cathode is 1 cm, which implies a mean drift velocity of less than approximately 6 cm/μs in this region.

One way of removing the echo hits from the final list of MUB space points is to reconstruct only the first triplet seen in any one chamber[11]. The probability of more than one beam-event muon passing through a single chamber in one event is thought to be very small. However, multiple hits may also be caused by secondary interactions, particularly delta rays (electrons removed from the walls of the chambers and the last few millimetres of the iron in front of the chambers). Simulation studies with 45 GeV muons (made by S. Hodgson [29] using the DELPHI Full Simulation program [36]) indicated that $6.0 \pm 0.4\%$ of chamber hits are accompanied by delta rays, and for $1.8 \pm 0.2\%$ of chamber hits there is a delta ray which is at least 2 mm closer to the anode than the muon. Therefore, if only the first hit is taken, the position of the muon track is recorded incorrectly in about 2% of cases.

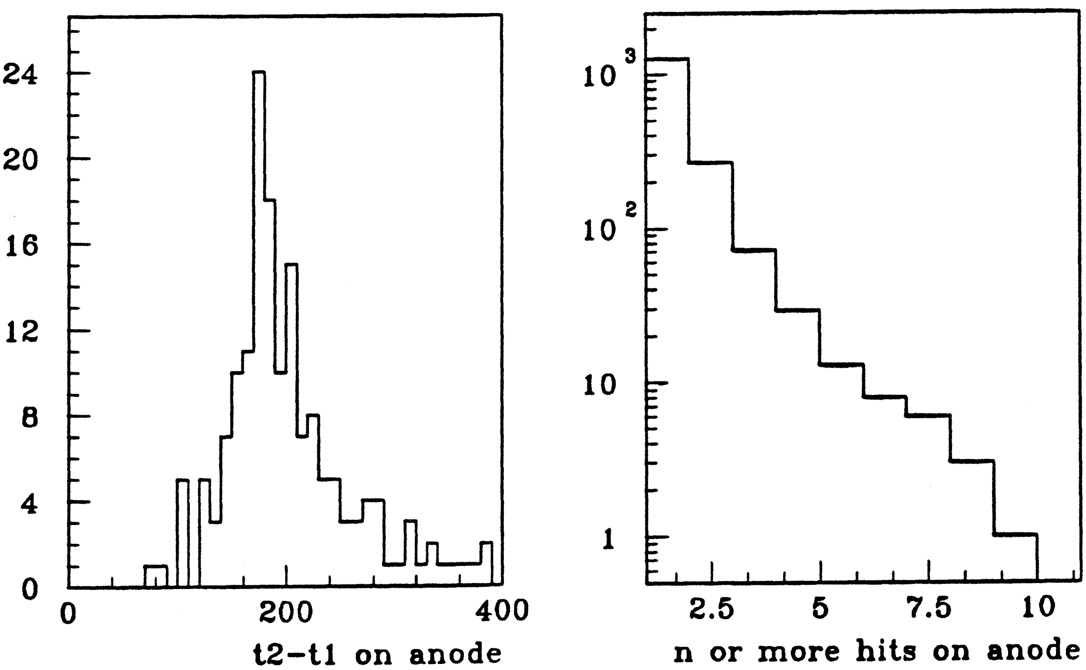

Figure 3.9: The nature of 'afterpulses' on the anodes in DELPHI. (a) $\Delta t = t_2 - t_1$, where t_2 is the time of the second pulse (first afterpulse) and t_1 is the time of the primary pulse. (b) The frequency occurrence of n or more hits on the anode, shown on a log-linear plot.

If all hits are reconstructed but there is information in several MUB layers, the muon identification package EMMASS (section 4.3) should in principle find the most likely solution where there are any ambiguities.

[11]This is indeed how the Barrel Muon reconstruction software operated in 1990.

Attempts to reduce the number of echo hits by adjusting the discriminator thresholds or the gas mixture have been unsuccessful [61]. However, the occurrence of multiple hits is not thought to present a serious problem for current analyses.

Chapter 4

DELPHI Offline Software

This chapter is devoted to a description of DELPHI offline software. In the first section we give an overview of the most important programs. Particular emphasis is placed on the DELPHI event reconstruction and analysis program, 'DELANA', and a package which handles the basic event information, called 'TANAGRA'. The second section — a discussion of the principles behind muon identification — acts as an introduction to section 3, which is a description of the algorithm used in DELANA to handle particle identification in the DELPHI Muon Chambers. Section 4 is a brief description of a package for fast simulation of the DELPHI Muon Detector.

4.1 Overview

The DELPHI experiment has the following features which had to be considered when designing the offline software:

- the large size of the collaboration;
- the complexity of the apparatus;
- the anticipated long-life of the apparatus, with build-up over several years and the probability of frequent hardware changes.

DELPHI offline software is written in standard FORTRAN77 and is maintained in files which are read and assembled by a CERN source code management system called PATCHY [33]. Programs are built up from several independent modules which are designed and written by many people at many institutes. They run on several types of main-frames and are *designed* to be 'user friendly' to allow ease of compilation and execution by every member of the collaboration.

As data structures in FORTRAN77—arrays and common blocks— cannot be manipulated as complete entities or be defined dynamically at execution time, DELPHI offline and online software uses ZEBRA [34]. This is a CERN data structure management system which overcomes these deficiencies and allows the data structures ('ZEBRA banks') to be written to an external storage medium and to be recovered intact on some other computer.

4.1.1 Detector Description

Data files describing the DELPHI detectors are built into an overall DELPHI database. The same data records are accessed by simulation, analysis and event display programs. Data files contain:

- calibration constants (pedestals, drift velocities etc.);
- geometry constants (down to the position of each wire for example);
- material constants (required to calculate the effects of various physical processes within DELPHI).

The interfacing of the detector description files to simulation or analysis programs is done using the Detector Description Access Package (DDAP) [35].

The geometry database is read by the general routines that are used to convert from local frames to the DELPHI frame. It is also accessed by the Detector Visualisation Package (DVP), which was used to produce the views of the Barrel Muon Detector (figure 3.2).

4.1.2 DELSIM

DELSIM [36] is the abbreviation for the DELPHI Full Simulation program. The package includes event generators for e^+e^- interactions (and some background events) and simulates the interactions of the generated particles with the DELPHI detectors.

There is a choice of generators, or one may read in externally generated events. A package of routines tracks particles through DELPHI, generating possible secondary interactions, and providing an interface to the detector-specific software. The description of the detectors is obtained from the database.

Each detector provides its own module (e.g. the Barrel Muon simulation processor is called MUBSIM). Each module has two objectives:

1. to determine space points for display purposes and for checking track finding algorithms;

2. to convert space points into pulses on electronic channels.

Inefficiencies are taken into account and realistic noise and background is added. The aim is to produce simulated data (in ZEBRA banks) that are *indistinguishable* from real data banks as they are written to disk at the DELPHI pit.

The software is written in a modular fashion, so detailed simulation may be switched off for detectors that are not of interest to the user, in order to save time and storage space.

A parallel stream of 'truth' information (i.e. information about the real nature of the event as opposed to how it appears in the detectors) is produced to allow general debugging of DELANA and for estimation of efficiencies in various physics channels.

4.1.3 DELANA

The DELPHI data analysis and event reconstruction program is called DELANA [38]. One may distinguish between high level steering routines, general purpose software modules, and detector-specific software modules. As with DELSIM, each detector is treated by a separate module (e.g. the Barrel Muon processor is called MUBANA).

For each event, a steering routine checks on the validity period of the database information for each detector and, if necessary, updates the constants which are in memory. For each detector module, steering routines are called to control the standalone 'local pattern recognition' of each detector. In the so-called 'first stage processing' data are analysed to produce space points, track elements, energy deposits etc., without using any information from other detectors[1]. Note that MUBANA produces space point information only.

[1]The Combined Calorimetry processor (CCA) is subsequently called to link data from the Electromagnetic Calorimeters and the Hadron Calorimeter for hadronic showers common to both detectors. However, the data from this processor will not be used in this analysis.

Track search processors group the track elements into candidate tracks which are then submitted to the full track fit to resolve ambiguities and provide fitted track parameters. The resulting tracks are extrapolated throughout the detector, giving impact points and track parameters and their errors (including extrapolated measurement errors and multiple Coulomb scattering errors) at the entry to each of the detectors, for use in the second stage pattern recognition.

In this second stage, tracking detectors are called to complete their pattern recognition using predictions supplied by the first stage. Those track elements not so far included in a fitted track are passed through the track fit and search again. All rebuilt and refitted tracks are extrapolated. Second stage calorimeter steering is called, and whenever a calorimeter can connect an energy deposit to an extrapolated charged track, this information is added to the track bank information.

The next step is to call the detector-specific particle identification modules (called EuMASS, where u=T for TPC, M for Muon Chambers, R for RICH's. EMMASS is the subject of section 4.3). The particle identification information is collected and analysed by a global processor which gives a final mass assignment to the tracks.

Finally, primary and secondary vertices are fitted from among the charged tracks. Neutral tracks are constructed from the calorimeter data and added to the primary vertex.

The output from DELANA is in data structures called TANAGRA banks.

4.1.4 TANAGRA

The purpose of TANAGRA (**Tr**ack **Ana**lysis and **Gra**phics package [39]) is to provide a coherent way of handling basic event information. It may be said to provide a 'backbone' for the offline analysis program, DELANA. The package is organised as a library of routines built on top of ZEBRA, and consists of:

- a data structure called VETBAS (**Ve**rtex and **T**rack **B**asic **S**tructure) which contains track, vertex and space point information in a form that is almost independent of the detector from which it originated;

- a package of routines to transfer, retrieve or modify the VETBAS. The data are carefully protected; a scheme is provided to test if an intervention is allowed, given a set of privileges depending on the user and the nature of the intervention;

- some application software, referred to as DAST (**D**irect **A**pplication **S**oftware of **T**anagra).

Kinds of TANAGRA Data

Several levels of data exist in the VETBAS structure (see figure 4.1). For each level there is a 'header' bank (**'Ti'**, where **i** stands for 'D','E','S','K','B',or 'V') and a 'results' bank (labelled **TiR**) which contains the results of the processing at that level.

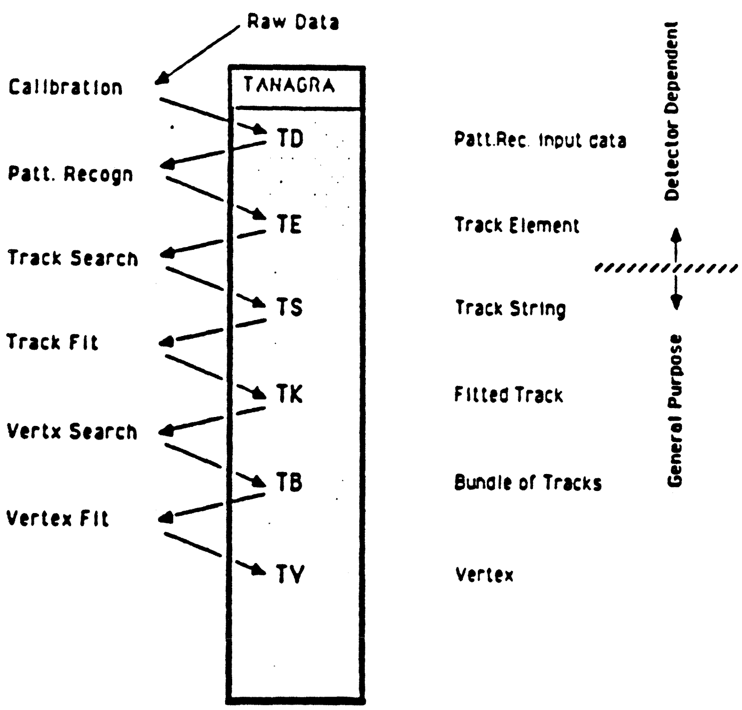

Figure 4.1: The different kinds of TANAGRA data

- **TD Banks** (Detector Data): TD results banks contain space points or clusters and the corresponding pulse heights.

  The Barrel Muon Chamber pattern recognition module MUBANA produces one TD bank for each *sector* in which there is a chamber with a hit (i.e. a triplet or a doublet). The results bank contains one 'point sequence' for each hit, containing information on the chamber number , the drift distance, and the delay line distance measured from the end nearest the centre of DELPHI (the 'far' end).

- **TE Banks** (Track Elements): The results of local pattern recognition are stored in TE banks. They contain the basic information necessary to combine these elements into tracks. MUBANA produces one TE [header] bank for each hit in the MUB. The TER [results] bank contains the position of the hit $(R, R\phi, z)$ in the DELPHI frame. If left-right ambiguity cannot be solved *two* results banks are created (with the same z coordinate and different R and $R\phi$ coordinates), but both TERs hang off the same header bank.

  The TERs are later modified (and new TERs may be created) in the muon mass identification module, EMMASS (section 4.3).

- **TS banks** (Track Strings): An element of the DAST package is a 'track search' which builds up 'strings' of track elements. Where there is some ambiguity, TANAGRA has the facility to keep all concurrent solutions and to declare that they are 'mutually exclusive'.

- **TK banks** (Tracks): One or several strings are put together to form a track by another DAST module. This 'track fitting' procedure solves all ambiguities and contradictions. Therefore, TK banks represent a clean and consistent set of tracks.

- **TV banks** (Vertices): A TV bank stores tracks obtained using a global vertex fit. For the back-to-back topologies found in muon-pair physics the fitted vertex may be unreliable, and consequently the muon tracks may be distorted. TV data are not used in the analysis of Chapter 5.

There is a general DELANA extrapolation package which gives intersection points of extrapolated tracks on various surfaces (cylinders and planes) throughout the detector. These intersection points are stored in **TKX** banks.

The analysis in this thesis is based exclusively on TANAGRA TE and TK information.

4.1.5 DST

DST ('Data SummaryTape') data give event information in its most concise form. The information on the DST is extracted from the TANAGRA output of DELANA. There is one DST track ('PA') bank for each TANAGRA TK bank. The structure of the track bank is flexible to accommodate information from the Calorimeters, the RICHs, Muon Chambers, TOF etc., but not all the routines to provide this information were available by the end of 1990.

From 1991 it is intended that only DST data will be stored for physics analyses. However, DST data are not used in this analysis.

4.1.6 DELGRA

The DELPHI interactive event display program DELGRA may be used to display simulation 'truth' banks or DST data, but is used most commonly with TANAGRA data. Figures 4.2 and 4.3 show a typical muon-pair event as displayed by DELGRA.

4.1.7 FASTSIM

The aim of the DELPHI fast simulation program FASTSIM [40] is to simulate many events in a short time, in order to do a first analysis of a considerable number of physical channels. A set of selected events may be reprocessed with DELSIM.

Event *generation* is exactly the same as for DELSIM. The fast event simulation is based on simplified tracking, simplified treatment of secondary processes, and simplified detector description in which the DELPHI detectors are represented by a set of cylindrical and planar reference surfaces (figure 4.4).

Figure 4.2: A typical muon-pair event as displayed by the DELPHI interactive analysis package DELGRA. There are two very straight back-to-back tracks (TKs), seen in the Inner Detector, TPC, and Outer Detector. Both tracks have good muon signals in the HCAL and the MUB. One track produces a line of TEs in the HPC which is characteristic of a minimum ionising particle.

Figure 4.3: Close-up of the same event as displayed by DELGRA. This track would in all probability be classified as a muon in three detectors: the HPC, the HCAL and the MUB.

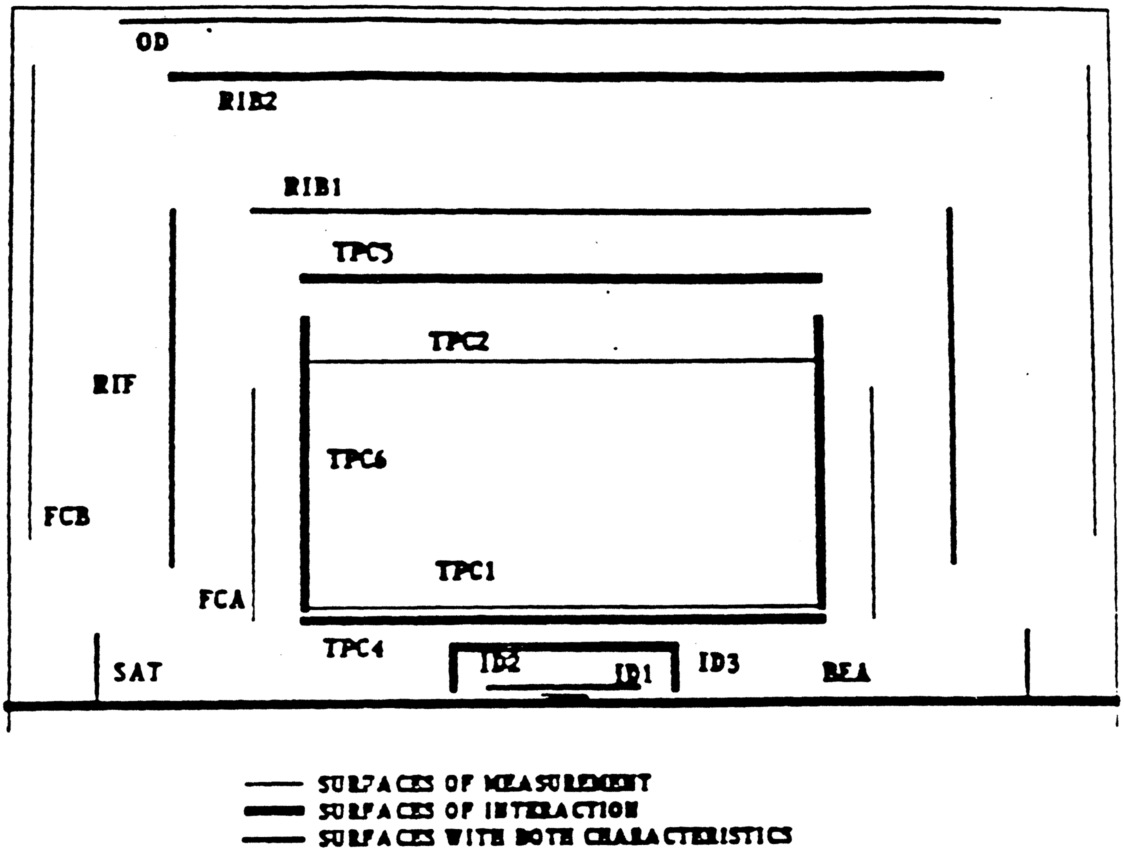

SURFACE	R_{min}	R_{max}	Z	X_{RL}	ρ	Z	A
BEA	7.8	7.8	290.	0.011	2.7	13	27.
VD1	9.	9.	12.	0.005	2.3	14	28.1
VD2	11.	11.	12.	0.005	2.3	14	28.1
ID1	12.	12.	40.	0.005	2.3	6	12.
ID2	22.3	22.3	60.	0.028	2.27	6	12.
ID3	12.2	22.3	60.	0.263	8.96	29	63.5
TPC1	36.5	36.5	134.				
TPC2	106.2	106.2	134.				
TPC4	30.75	30.75	134.	0.025	2.27	6	12.
TPC3	127.1	127.1	134.	0.223	2.64	15	30.
TPC6	34.	117.	134.	0.3	2.7	13	27.
RIB1	147.3	147.3	160.	0.066	2.64	15	30.
RIB2	188.	188.	200.	0.093	2.7	13	27.
OD	200.	200.	227.	0.126	2.7	13	27.
FCA	31.7	98.	160.				
RIF	46.8	147.3	203.	0.281	2.7	12	25.
SAT	8.	29.	240.				
FCB	55.3	192.	274.				

Figure 4.4: FASTSIM Reference Surfaces for Detector Description

A particle's track is parameterised as an ideal helix. Starting from a point on some surface, the step is taken exactly as the distance to the next surface along the helix. One may distinguish three types of surfaces:

a) measurement surfaces;

b) surfaces in which the particle suffers secondary interactions;

c) surfaces with both types of characteristics.

If the particle decays, the step is the distance up to the decay point. When the surface is reached, control is given to the software module for the associated detector. In the case of surfaces of types b) and c), one test is made on all the different secondary processes which may be suffered inside it by the particle.

The history of the simulated event, with all the initial momenta and characteristics of the primary and secondary particles is stored in one common block. Another common contains the measured momentum, the mass identification, and the detectors traversed for each track. User routines are called at various stages for easy access to the event information and for booking and filling histograms etc.

The user may also choose output in the form of TANAGRA banks. TE banks (space points) are produced in FASTSIM (but not TD banks). It is possible to use these data as input to DELANA and DELGRA. The fast simulation of the Muon Chambers is described in section 4.4.

4.2 Muon Identification

In this section we discuss why muon identification is important and the outline means by which it is done, as a prelude to the description of the algorithm used in DELPHI to identify muons using the Muon Chambers (section 4.3).

The observation of muons plays an important role in the study of several physics channels, including:

- Muon-pair Physics:

$$e^+e^- \rightarrow \mu^+\mu^-(\gamma)$$

- Higgs production e.g.

$$e^+ + e^- \rightarrow H^0 Z^{0*}$$

$$Z^{0*} \rightarrow \mu^+\mu^-$$

- Production of heavy quarks and leptons, for example:

$$e^+e^- \rightarrow b\bar{b}$$

$$b \rightarrow \mu^- c\bar{\nu}_\mu$$

and

$$e^+e^- \rightarrow \tau^+\tau^-$$

$$\tau^- \rightarrow \mu^- \nu_\tau \bar{\nu}_\mu$$

4.2.1 Methods of Identification

The methods of muon identification rely on the differences between the interactions of muons with matter and those of other particles. Hadrons undergo strong interactions with matter, causing a cascade of particles. Electrons cause electromagnetic cascades when they pass through matter due mainly to bremsstrahlung and pair-production processes. Muons do not interact strongly and do not emit bremsstrahlung as significantly as electrons (the bremsstrahlung cross-section for a relativistic particle depends inversely on the square of the incident particle mass).

There are two methods of discriminating between muons and hadrons or electrons:

1. Muons may be recognised in a calorimeter as isolated, minimum ionising tracks, frequently ranging far beyond the tracks from hadronic showers or electromagnetic cascades.

   In DELPHI, minimum ionising particles may be identified in both the Electromagnetic and the Hadron Calorimeters (see Chapter 5).

2. Muons may be identified by their ability to penetrate matter almost without being deflected. Charged particle detectors ('muon chambers') are placed behind an absorber (usually iron). If the extrapolation of a track in front of the absorber to the detector layers can be matched with hits in the detectors, then the track is likely to be a muon.

   In DELPHI, these charged particle detectors are the Barrel and End-Cap Muon Chambers, while the Calorimeters act as the absorber.

Muons and charged pions cannot be separated using the DELPHI RICHs because they have very similar masses ($m_\mu = 106$ MeV, $m_{\pi^\pm} = 140$ MeV).

4.2.2 Identification by Muon Chambers

The method is to match muon chamber hits with tracks by extrapolating the track through the absorber and constructing around it ellipses which represent, for given probabilities, the limits of multiple Coulomb scattering for a muon of this momentum. However, there are several ways in which a small percentage of hadrons may be misidentified as muons :—

1. Particles produced in the hadronic shower may escape from the back of the absorber and give hits in the muon chambers which mimic those produced by an almost undeviated track.

2. Hadrons may slip through cracks in the absorber ('sneak-through') or there is a small chance that they may simply not interact ('sail-through').

3. Pions and kaons may decay to muons, which are then identified in the muon chambers. Some decays will be detected in the tracking detectors, but the small p_T of the decay (30 MeV for pions) implies that the change in track direction is small and the decay vertex is hard to detect.

The term 'punch-through' is usually applied to the sum of all three effects.

The probability of sail-through is reduced if the thickness of the iron absorber is increased. However, if the absorber is too thick, low energy muons will be 'ranged out'[2]. The probability of a hadron failing to interact in x cm of absorber is almost independent of momentum above about 2 GeV, and is given by $P(x) = \exp^{-x/\lambda}$ where $\lambda \approx 17.1$ cm for iron (the 'absorption length'). In the DELPHI Barrel $x \approx 100$ cm, which implies hadron sail-through probability of about 3×10^{-3}. Assuming muons lose energy by ionisation at a rate of about $\mathrm{d}E/\mathrm{d}x \approx 1.6$ GeV/m in iron, muons of energies less than about 1.6 GeV will be ranged out. Also, the deviation of the track due to multiple scattering becomes very much larger on average at lower momenta (see figure D.1).

The punch-through probability is in general dependent on the hadron momentum and detector resolution (ideally, measurement errors on the hit points and track extrapolation errors should be less than the uncertainties due to multiple Coulomb scattering). Figure 4.5 shows a Monte Carlo calculation of percentage punch-through for π^- of different incident momenta p as a function of iron absorber depth (from [42]).

An approximate punch-through probability in DELPHI was estimated using results from the HFM experiment ([28] and section 3.4). One criterion adopted for a positive muon identification was to require the extrapolated track to be matched with hit(s) in the "Inner" module and in the "Peripheral" module[3]. The percentage of chosen events having this muon signal was $2.3 \pm 0.3\%$ for a 20 GeV pion beam (compared with $97.7 \pm 0.2\%$ for muons).

However, punch-through due to feedthrough of secondaries and decays was reduced by comparing the particle direction before and behind the absorber. The track direction after the absorber was deduced from fitting a line through the hits in the "Inner" and "Peripheral" modules. For genuine muons, this track is expected to be almost colinear with the track in front of the absorber (with a small deviation due to multiple scattering). By imposing suitable cuts on the angular difference the percentage of 20 GeV pions giving muon signals was almost

[2]Cost is also a factor, especially in a cylindrical absorber where the amount of iron required increases as the square of the thickness of the absorber.

[3]As explained in section 3.4, the arrangement of modules in the HFM experiment was not exactly the same as in DELPHI.

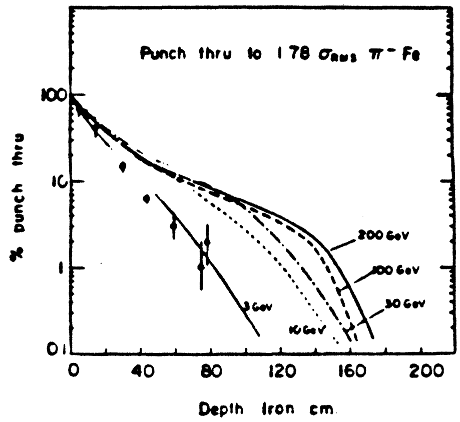

Figure 4.5: Monte Carlo punch-through probabilities of π^- in iron as a function of absorber depth (from [42]). σ_{RMS} is the root mean square multiple scattering radius of an equivalent muon. 1.78 σ_{RMS} corresponds to the circle containing 96% of muons of this momentum.

halved to $1.3 \pm 0.2\%$, while the percentage of muons passing all cuts was virtually unchanged ($96.9 \pm 0.3\%$).

In DELPHI, the task of maximising muon identification efficiency and minimising hadron contamination is complicated by the presence of a magnetic field, a more complex detector geometry, and in general a more complex event topology with a consequential higher chance of misassociation of tracks and Muon Chamber hits. The software package which was written to handle this task is the subject of the next section.

4.3 EMMASS

EMMASS is the package that handles muon identification by the DELPHI Muon Chambers. Certain routines are common to the Barrel Muon Chambers and the Forward Muon Chambers, in order that the same philosophy is applied to both the Barrel and the End-Cap. The code is the work of P.M.Kluit (IIHE, Brussels) who wrote the MUF code and the common track fitting routine, C.Buttar (now at Sheffield University) who worked on an earlier version of the MUB code, and myself. It is based on ideas developed with P.Renton (Oxford) and J.Wickens (IIHE, Brussels). The code has been run on all DELPHI data since the beginning of 1990 data taking, but EMMASS remains an ongoing project, since the understanding the performance of several different elements of the DELPHI experiment and its software is critical in order to realise the full potential of the EMMASS algorithm.

The package runs within the framework of the general DELPHI event reconstruction program DELANA, and is run simply by selecting the appropriate cards in the DELANA 'title file'. The input to, and output from, this package is TANAGRA data.

4.3.1 General Principles

The idea is to match, as accurately as possible, tracks found in the central tracking detectors of DELPHI with space points reconstructed by the Muon Chambers. This is done by extrapolating all suitable tracks through the Electromagnetic and Hadronic Calorimeters and the coil towards the planes of the Muon Chambers, taking into account energy loss, multiple Coulomb scattering, and the influence of the DELPHI magnetic field, and propagating the measurement errors on the initial track. The predicted intersection points of the extrapolated track with the Muon Chambers (the 'extrapolated hits') are then compared in EMMASS with the measured space points, taking into account the full error matrix on the extrapolated hit and the detector measurement errors on the measured hit.

In practice, muon identification criteria must be tailored to the particular analysis. In muon-pair analyses for example, where one usually preselects events with two high momentum, roughly back-to-back tracks, one may in general adopt looser criteria than may be required to find a muon in a jet.

The aim of EMMASS is to output all information which may be relevant for muon identification. The user may then select cuts according to the particular requirements of his/her analysis and the standard of performance of the relevant detectors at the time the data were taken.

EMMASS produces both spatial information and angular information (i.e. the track direction at the Muon Chambers).

4.3.2 Interface of EMMASS with other DELPHI software

The input to EMMASS is Muon Chamber space points (TE banks from MUBANA or MUFANA) and extrapolated track parameters (TKX banks), together with their respective error matrices. The geometry database is also required.

Tracks which are found in the central tracking detectors are stored in TK banks. The DELANA extrapolation package (EXX) is called to calculate the intersection points and track parameters for a set of pre-defined *cylinders* and *planes* throughout DELPHI which correspond roughly to the various detectors[4]. The results are stored in TKX banks (there is one TKX bank for each pre-defined surface that is intersected by the track). The surfaces corresponding approximately to the Muon Chambers are [38]:

- for MUB: three cylinders with axis coincident with the z axis, with radii 445.5 cm, 479.3 cm, and 532.0 cm, limited by $|z| \leq z_{max} = 380.0$ cm;
- for MUF: planes of constant z at $z = 469.0$ cm, 506.0 cm, limited by 91.0 cm$\leq R \leq 632.0$ cm.

The aim of the MUTRACK, the package that performs the extrapolations through the Calorimeters and the coil [41], is to output 'deterministic' extrapolated hits, taking into account bending in the magnetic field but not attempting

[4]In general, these surfaces are the same as those used for the simplified description of DELPHI in the Fast Simulation program.

to mimic the effect of multiple scattering. The package also calculates the track direction at the intersected surface, which is given by the polar and azimuthal angles of the momentum vector, denoted θ and ϕ respectively. The TKX bank also includes the covariance matrix containing the variances and covariances on $T1, T2, \theta, \phi$ due to multiple scattering and propagated measurement errors ($T1$ and $T2$ are the coordinates measured in the Muon Chambers. In the Barrel, $T1 = R\phi, T2 = z$; in the End-Cap $T1 = x, T2 = y$).

EMMASS is called in DELANA once per event after all tracks and space points have been finalised. We shall now give a brief description of the tasks performed by EMMASS for each *track*, using the Barrel Muon Chambers as the example (the reader is referred to Appendix C for more details of the routines involved). The program flow for the Forward Muon Chambers is quite similar.

4.3.3 Processing for Each Track

A loop is performed over all charged tracks. It is necessary first to obtain the coordinates of the extrapolated hits in the seven layers of the MUB (rather than on the three cylinders defined for the extrapolation package). A straight line extrapolation is made using the momentum vector of the extrapolated track at its intersection with the cylinder. The MUB geometry database is used as several modules are at anomalous radii.

Muon identification is then performed in two stages:

- The first task is to find all the MUB space points that are close to this extrapolated track. We form a χ^2 for each space point i, defined by:

$$\begin{aligned}\chi_i^2 \;=\; & \frac{1}{\sigma_{R\phi}^2\sigma_z^2 - (\mathrm{cov}\,(R\phi, z))^2}[\left(R\phi_{muc}^i - R\phi_{ex}^l\right)^2 \sigma_z^2 + \left(z_{muc}^i - z_{ex}^l\right)^2 \sigma_{R\phi}^2 \\ & - 2\left(R\phi_{muc}^i - R\phi_{ex}^l\right)\left(z_{muc}^i - z_{ex}^l\right)\mathrm{cov}\,(R\phi, z)] \qquad (4.1)\end{aligned}$$

  where: $R\phi_{muc}^i$ and z_{muc}^i are the coordinates of space point i as measured in the MUB, $R\phi_{ex}^l$ and z_{ex}^l are the coordinates of the extrapolated hit in MUB layer l, and the covariance $\mathrm{cov}\,(R\phi, z)$ is from the covariance matrix on the extrapolated hit as defined at the nearest cylinder. The variances

$\sigma^2_{R\phi}$ and σ^2_z are given by the errors on the extrapolated track and the MUB measurement errors added in quadrature[5].

All space points which have $\chi^2_i \leq$TKCUT (presently 50) are gathered.

- The space points that have the best match with the extrapolated track are chosen. The extrapolated track is fitted to hits in the MUB. Essentially a straight-line minimum χ^2 fit is made to the *differences* between the coordinates of the extrapolated hits and the MUB space points (the method of fitting is described more fully in the next section). There may be more than one space point in any one layer that passes the cut on χ^2_i (due to left-right ambiguous solutions, afterpulsing, or large errors on the extrapolated track, for example). Only one hit per layer is used in the fit, the 'best' fit being defined in terms of the lowest value of χ^2_G (the 'global χ^2' of the fit). If for this 'best' case χ^2_G/ndf >CHISEL (presently 100), each layer is omitted from the fit in turn, in order to try to find a 'good' solution. If no such solution is found, all combinations with two layers left out are fitted. This may go on until no more layers can be dropped, when the best of the previous results is kept.

In this way we associate MUB space points to the track, we fit the track through the MUB layers, and we have a measure of the quality of association. The associated space points, the χ^2_G, and additional information are output in the TER banks of the Muon Chambers.

4.3.4 Method of Fitting

The fitting routine EMMFIT was written by P.M. Kluit, but is briefly described here for completeness. The idea is to shift the extrapolated track to match the measured space points in the Muon Chambers, taking into account the errors on these quantities. The global χ^2 is built up from two contributions:

$$\chi^2_G = \chi^2_{ex} + \chi^2_{muc} \tag{4.2}$$

[5]When $\mathrm{cov}\,(R\phi, z) = 0$, this expression takes on the more intuitive form:

$$\chi^2_i = \left(\frac{R\phi^i_{muc} - R\phi^l_{ex}}{\sigma_{R\phi}}\right)^2 + \left(\frac{z^i_{muc} - z^l_{ex}}{\sigma_z}\right)^2 .$$

χ^2_{ex} takes into account the shifts made in the extrapolated track:

$$\chi^2_{ex} = [\Delta T1_{ex} \quad \Delta T2_{ex} \quad \Delta\theta_{ex} \quad \Delta\phi_{ex}] \quad V_{ex}^{-1} \begin{bmatrix} \Delta T1_{ex} \\ \Delta T2_{ex} \\ \Delta\theta_{ex} \\ \Delta\phi_{ex} \end{bmatrix} \tag{4.3}$$

where V_{ex}^{-1} is the inverse covariance matrix from the extrapolation package and $\Delta T1_{ex}, \Delta T2_{ex}, \Delta\theta_{ex}$, and $\Delta\phi_{ex}$ are the shifts in the extrapolated track parameters:

$$\begin{aligned} \Delta T1_{ex} &= T1_{ex} - T1_{fit} \\ \Delta T2_{ex} &= T2_{ex} - T2_{fit} \\ \Delta\theta_{ex} &= \theta_{ex} - \theta_{fit} \\ \Delta\phi_{ex} &= \phi_{ex} - \phi_{fit} \end{aligned} \tag{4.4}$$

For example in the Barrel, $T1_{fit}$ is the $R\phi$ of the fitted track. ϕ and θ are the azimuthal and polar angles of the momentum vector. All quantities are defined on the innermost reference surface.

χ^2_{muc} takes into account the deviations from the space points in the Muon Chambers. It is defined as:

$$\chi^2_{muc} = \left[\Delta T1^1_{muc} \quad \Delta T2^1_{muc} \ldots\right] V_{muc}^{-1} \begin{bmatrix} \Delta T1^1_{muc} \\ \Delta T2^1_{muc} \\ \ldots \\ \ldots \end{bmatrix} \tag{4.5}$$

where V_{muc} is the (diagonal) error matrix containing the Muon Chamber measurement errors on the coordinates $T1$ and $T2$ and:

$$\begin{aligned} \Delta T1^i_{muc} &= T1^i_{muc} - T1^i_{fit} \\ \Delta T2^i_{muc} &= T2^i_{muc} - T2^i_{fit} \end{aligned} \tag{4.6}$$

For example in the Barrel, $T1^i_{muc}$ is $R\phi$ of the i^{th} measured space point and $T1^i_{fit}$ is the $R\phi$ of the fitted track in that layer. The coordinates $T1^i_{fit}$ and $T2^i_{fit}$ are calculated from the shifts in the extrapolated track parameters (equations 4.4).

χ^2_G is then minimised with respect to the four shifts: $\Delta T1_{ex}, \Delta T2_{ex}, \Delta\theta_{ex}$, and $\Delta\phi_{ex}$. The minimisation is done analytically by a matrix method.

To take a simple example, let us consider the case where there is no correlation between the $(R\phi, R)$ plane and the (z, R) plane. The fitting procedure then amounts to fitting independently in these two planes a straight line through the *differences* between the *measured* space points and the *extrapolated* hits, taking into account the predicted track direction at the innermost reference surface. The deviation of measured space points from the fitted line should be due to the Muon Chamber measurement errors (neglecting multiple scattering *between* layers), whilst multiple scattering and propagated measurement errors are absorbed in $\Delta R\phi_{ex}$ and $\Delta\phi_{ex}$, and in Δz_{ex} and $\Delta\theta_{ex}$.

After the fit the results for χ^2_G, χ^2_{ex} and χ^2_{muc} are known, as well as the values of the four fitted variables and the coordinates of the fitted track through each layer of the Muon Chambers.

4.3.5 Output of EMMASS information

Recall that after MUB local pattern recognition there is one TE [header] bank for each physical hit (triplet or doublet). If there are two or more TER [results] hanging from the header they are ambiguous (i.e. mutually exclusive) solutions. The existing information in the results bank includes:

Word 2: Identifier of the chamber in which this hit was seen;

Word 10-12: $R, R\phi, z$ coordinates of this space point solution.

If a space point is associated to an extrapolated track, several new words are added to the results bank. Otherwise, the results bank is left unaltered.

The additional words are shown in table 4.1. Words 3 and 20 to 35 are the same for all results banks which represent space points that are associated to a *single* track, and contain all the quantities the user is likely to cut on. Summary information on which layers have a hit associated to the track is packed in the 'hit pattern' (word 35):

$$\text{hit pattern} = \sum_{l=1}^{7} 2^{l-1}\delta_l \tag{4.7}$$

where $\delta_l = 1$ if there is an associated hit in layer l, and is zero otherwise ($l = 1$ is the layer nearest to the interaction point).

Words 36 to 41 contain information which is specific to this particular space point.

The user may obtain a list of all the results banks associated to a given track (with a suitable call to the TANAGRA subroutine TLIST), or may start from the

Word	Content
3	TANAGRA identifier of extrapolation bank (TKX) on innermost cylinder
20	Number of mass assignments following = 1
21	Number of degrees of freedom of fit
	= 2× number of layers associated to track
22	DELPHI muon mass code = 6
23	Global χ^2 from fit = χ^2_G
24	2 (one 'global' and one 'specific' calorimetric extension of TER)
25	χ^2 from fit of Muon Chamber information alone = χ^2_{muc}
27	$R\phi_{ex} - R\phi_{fit}$ on innermost cylinder
28	$z_{ex} - z_{fit}$ on innermost cylinder
29	$\theta_{ex} - \theta_{fit}$ on innermost cylinder
30	$\phi_{ex} - \phi_{fit}$ on innermost cylinder
31	$\sigma^{ex}_{R\phi}$ = error in extrapolated $R\phi$ on innermost cylinder
32	σ^{ex}_{z} = error in extrapolated z on innermost cylinder
33	σ^{ex}_{θ} = error in extrapolated θ on innermost cylinder
34	σ^{ex}_{ϕ} = error in extrapolated ϕ on innermost cylinder
35	Hit Pattern (see text)
36	MUB layer number l for this space point
37	Layer χ^2 defined by
	$\chi^2_l = \left(\frac{R\phi_{fit}-R\phi_{muc}}{\sigma^{muc}_{R\phi}}\right)^2 + \left(\frac{z_{fit}-z_{muc}}{\sigma z_{muc}}\right)^2$
39	R^{fit}
40	$R\phi^{fit}$
41	z^{fit}

Table 4.1: Additional Words in 'Muon-ID' TER Banks

MUB TERs and find the track involved using the extrapolation bank identifier on the innermost reference surface (TER word 3).

All the relevant information is written on to the DST.

Multiple Associations

It is possible in complex events that a single space point (or two space points representing mutually exclusive solutions of a single physical hit) may be associated to more than one track. In this case, EMMASS flags the association that it feels is most likely, based first on the number of layers associated and then on χ^2_G, but the information in the results banks is untouched[6].

4.3.6 EMMASS Results

Figure 4.6 shows the difference between the MUB measured hit and the fitted track for a sample of real data muon-pair candidate events from the data collected in 1990. Tracks in positive and negative z are plotted separately. The quantity $(R\phi_{fit} - R\phi_{muc})$ is seen to be normally distributed with a mean close to zero and a σ of about 5 mm. This is an indication of the measurement error in the MUB. The plots of $(z_{fit} - z_{muc})$ show that the mean difference between the fitted track and the MUB space-points is -2.1 cm for tracks where $z_{ex} \geq 0$ ($\theta \leq 90°$) and $+2.1$ cm where $z_{ex} < 0$. To investigate this further, plots were made of $(z_{muc} - z_{ex})$ in the two halves of DELPHI, and $(z_{muc} - z_{ex})$ against z_{ex} (figure 4.7). It is clear that the reconstructed MUB hit is systematically about 1% further from the centre of DELPHI in z than the prediction for the extrapolated track[7]. The same results are seen using a very simple straight line extrapolation of the track in the central tracking chambers[8]. A similar 'z shift' between the extrapolated track and the local hit has since been seen in the Inner Detector. This shift is under active investigation at the time of writing.

[6]In TANAGRA terminology, a multiple association is manifest by the existence of more than one TER [results] bank with EMMASS information hanging off the same TE [header] bank. EMMASS flags the preferred TER as being 'active' (TANAGRA allows only one TER per TE to be active); the other solutions are 'de-activated' but not 'disabled', so the user may look for other solutions herself.

[7]The smaller peaks at ±10-20 cm on either side of the main peak are due to hits reconstructed from *doublets*, for which there are systematic errors which are presently under investigation.

[8]This is to be expected as there should be very little bending in the (R, z) plane due to the magnetic field.

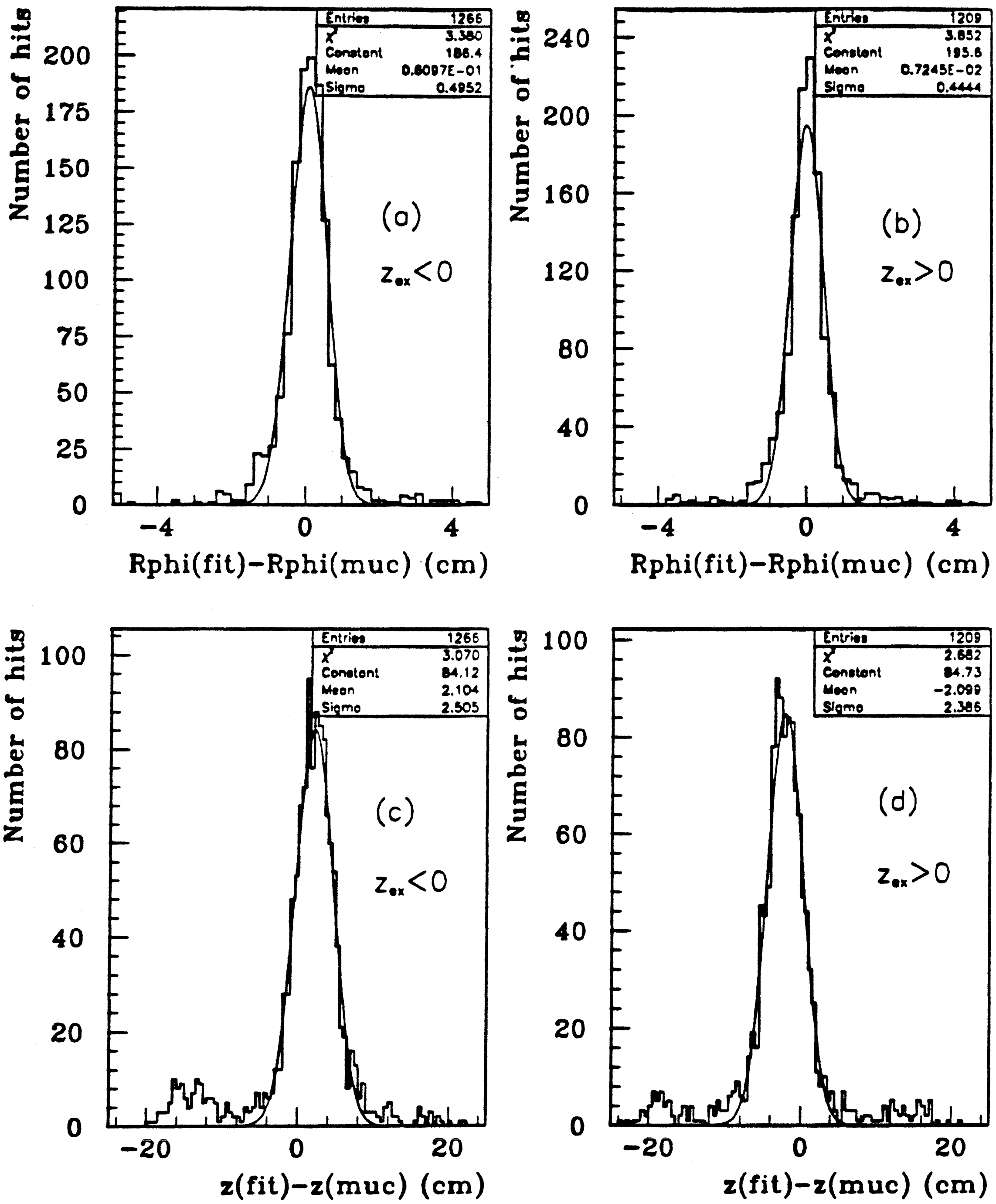

Figure 4.6: Difference between MUB hit and the fitted track in EMMASS, for a sample of muon-pair candidate events. (a) $(R\phi_{fit} - R\phi_{muc})$ for $z_{ex} < 0$, (b) $(R\phi_{fit} - R\phi_{muc})$ for $z_{ex} > 0$, (c) $(z_{fit} - z_{muc})$ for $z_{ex} < 0$, (d) $(z_{fit} - z_{muc})$ for $z_{ex} > 0$

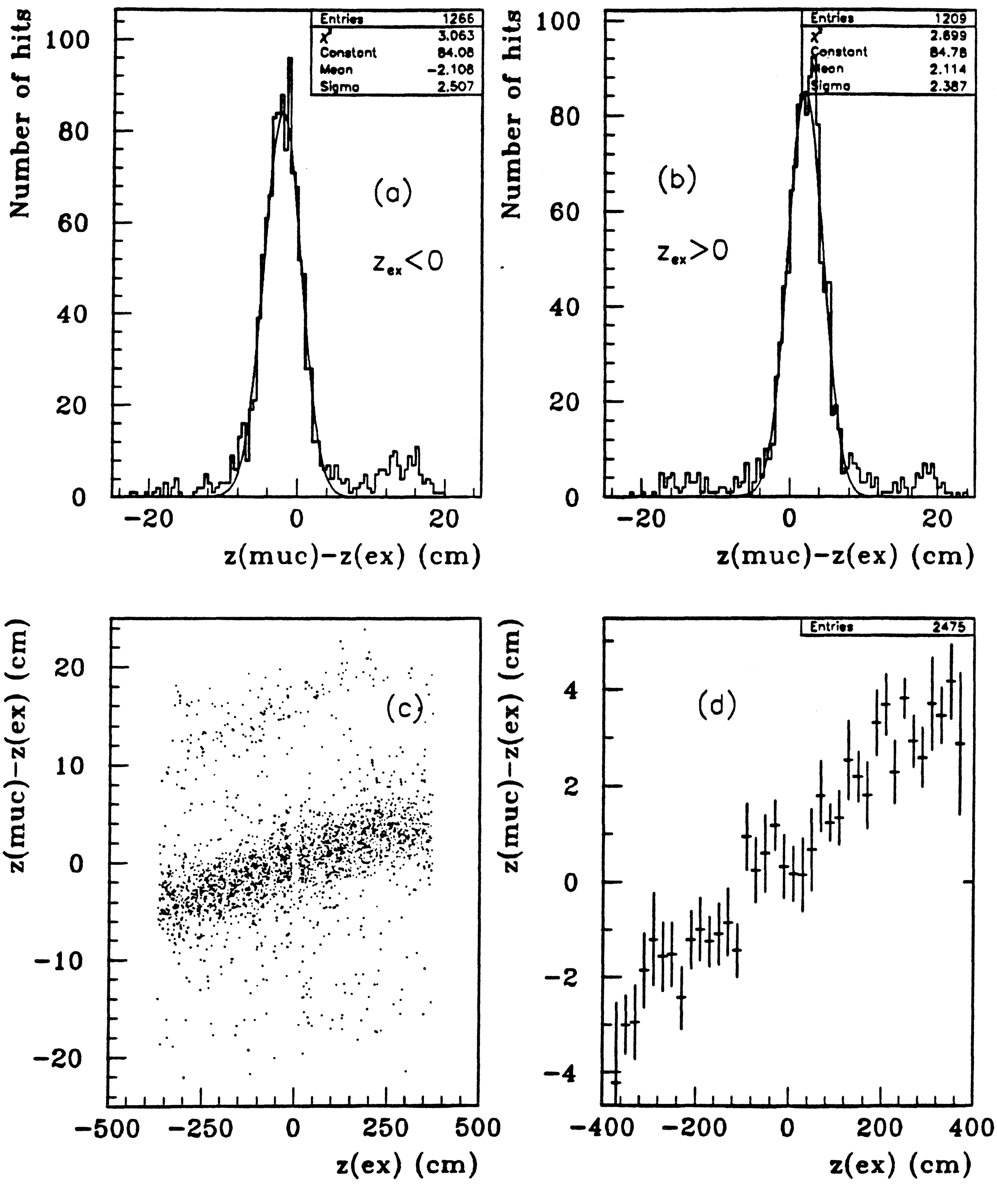

Figure 4.7: Difference between MUB hit and the extrapolated track in EMMASS in the z coordinate, for a sample of muon-pair candidate events. (a) $(z_{muc} - z_{ex})$ for $z_{ex} < 0$, (b) $(z_{muc} - z_{ex})$ for $z_{ex} > 0$, (c) $(z_{muc} - z_{ex})$ against z_{ex} (scatter plot), (d) $(z_{muc} - z_{ex})$ against z_{ex} (profile plot).

Figure 4.8 shows the χ^2_G distribution in the MUB for these muon-pair candidate events. For this data sample, the χ^2_G is presently not correctly normalised. Work is continuing to obtain accurate estimates of the magnitude of all the errors which are input to EMMASS and to correct all systematic deviations.

The EMMASS package was run on all data in 1990 as part of the DELPHI data production chain, and its results were used for muon identification by the Muon Chambers in a variety of physics channels.

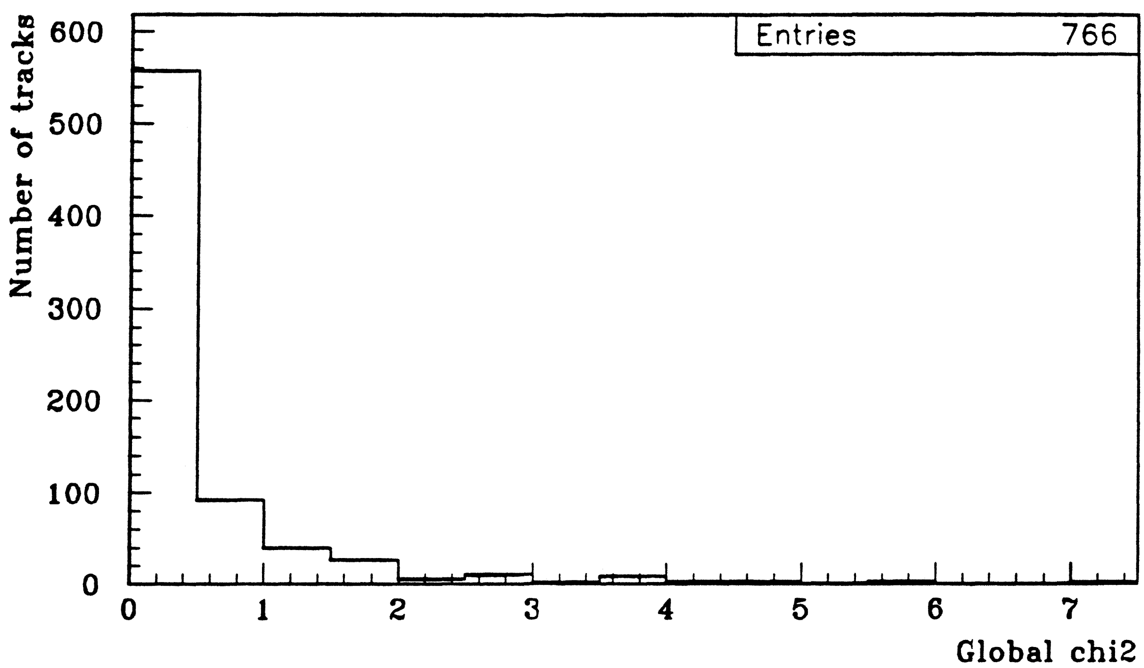

Figure 4.8: χ^2_G from EMMASS for a sample of muon-pair candidate events.

4.4 Fast Simulation of the Muon Detector

In this section we describe the FASTSIM module SPMSIM, which simulates the response of the Barrel and the End-Cap Muon Chambers. In FASTSIM , normal tracking in the Barrel ends at a cylinder which corresponds to the Outer Detector, and at a plane close to Forward Chamber B in the End-Cap. The Calorimeters, the coil and the Muon Chambers lie outside these boundaries. Those muons with momentum $p > 3$ GeV and a small fraction of hadrons chosen at random are tracked up to the Muon Chambers using the same package as is used in DELANA for track extrapolation through the DELPHI Calorimeters[9] (MUTRACK [41]).

SPMSIM is called on a track-by-track basis. Its purpose is to produce space points *as reconstructed* in the Muon Chambers. For a track in the Barrel, the following quantities are input to SPMSIM:

- Coordinates $(R, R\phi, z)$ for the intersection of the track with a simplified model of the MUB (a perfect 24-sided polygon of 7 layers).

- The (co-)variances on $R\phi$ and z in each of the three layers of modules (Inners, Outers and Peripherals) *and* the covariances *between* modules (Inners and Outers, Inners and Peripherals, Outers and Peripherals). These are purely due to multiple Coulomb scattering since measurement errors in the central tracking detectors are not modelled.

Analogous quantities are input for tracks passing through the End-Cap.

We shall briefly describe the tasks performed by this module (see Appendix D for more details on the routines involved). First we determine where the track actually passed through the Muon Detector:

- The first step, if the user requests this, is to obtain a realistic impact point after allowing for multiple scattering. A Gaussian distributed random number generator is employed with the covariances from the track extrapolation package, bearing in mind the correlations between layers (see Appendix D).

[9] The DELANA muon identification package EMMASS gathers MUTRACK information from TANAGRA TKX banks. Thus the highly modular nature of DELANA is retained (EMMASS may be rerun on existing TANAGRA data without performing the track extrapolations again). The FASTSIM Muon Chamber simulation module SPMSIM accesses actual MUTRACK common blocks, and so is able to gather additional information to that used by EMMASS.

- Checks are made to determine if the track passed through a chamber or struck 'dead space'[10]. If the track passed through a chamber, the chamber number[11] and the drift distance are calculated. Note that impact points in the third layer of the Inner modules of the MUB (which is not normally active) are ignored.

The next task is to determine the space points which Muon Detector reconstructs:

- Within a chamber there is a small amount of dead space, for example at the anode wire supports ('spiders'). By default the chamber efficiency is globally 95%, so 5% of all hits are discarded at random[12].

- The hit point is smeared for measurement error using a Gaussian distributed random number generator. In the Barrel the measurement errors are $\sigma_z = 1$ cm, $\sigma_{R\phi} = 1$ mm by default.

- If the track produces a hit in only one of the two layers of a module there should be left-right ambiguity, so a second space point is generated on the other side of the chamber's anode wire.

The generated space points are stored in common blocks for easy access by user routines. TANAGRA TE banks are created which are indistinguishable in form from those created in DELANA after local pattern recognition (by the MUBANA and MUFANA modules).

4.4.1 Comparison with DELSIM

The detector simulations of DELSIM and FASTSIM are entirely independent. A comparison has been made of the hit distributions obtained in one *sector* of the Barrel Muon Chambers according to the two simulations[13]. 5000 muons of momentum $p = 45$ GeV were generated randomly in the angular range

[10]The high degree of symmetry of the Muon Detector means that it is possible to model nearly all the areas which are without Muon Chamber coverage. These include the gap between the MUB and the MUF, the holes for the Solenoid support legs, nylon endplugs, cryogenic and cable ducts, and various non-standard modules.

[11]In the End-Cap, only the 'quadrant' identifier is found.

[12]Like most other parameters, this efficiency is set at the beginning of a run, and it may easily be adjusted by the user or optimised to give the best agreement with real data samples.

[13]This comparison is the work of S.D.Hodgson, and is reported in [29]

$50° \leq \theta \leq 90°$ and $22.5° \leq \phi \leq 37.5°$. The number of MUB hits recorded is shown in table 4.2. The ratio of DELSIM to FASTSIM hit distributions is plotted in figure 4.9.

Layers Hit	DELSIM	FASTSIM	Ratio
0	236 ± 15.4	303 ± 17.4	0.78 ± 0.07
1	230 ± 15.2	189 ± 13.8	1.22 ± 0.12
2	859 ± 29.3	731 ± 27.0	1.18 ± 0.06
3	1083 ± 32.9	1256 ± 35.4	0.86 ± 0.04
4	1978 ± 44.5	1964 ± 44.3	1.01 ± 0.03
5	621 ± 24.9	557 ± 23.6	1.11 ± 0.06
6	8 ± 2.8	0	-

Table 4.2: Comparison of the number of MUB hits recorded in DELSIM and FASTSIM for 5000 single muons, and their ratio (from [29]). The option for simulation of random electronic noise in DELSIM was disabled. The assumed global chamber efficiency in FASTSIM was 95%, while in DELSIM individual chamber efficiencies were taken from the test-rig measurements in the database. In this study, FASTSIM required a factor of eight less CPU time.

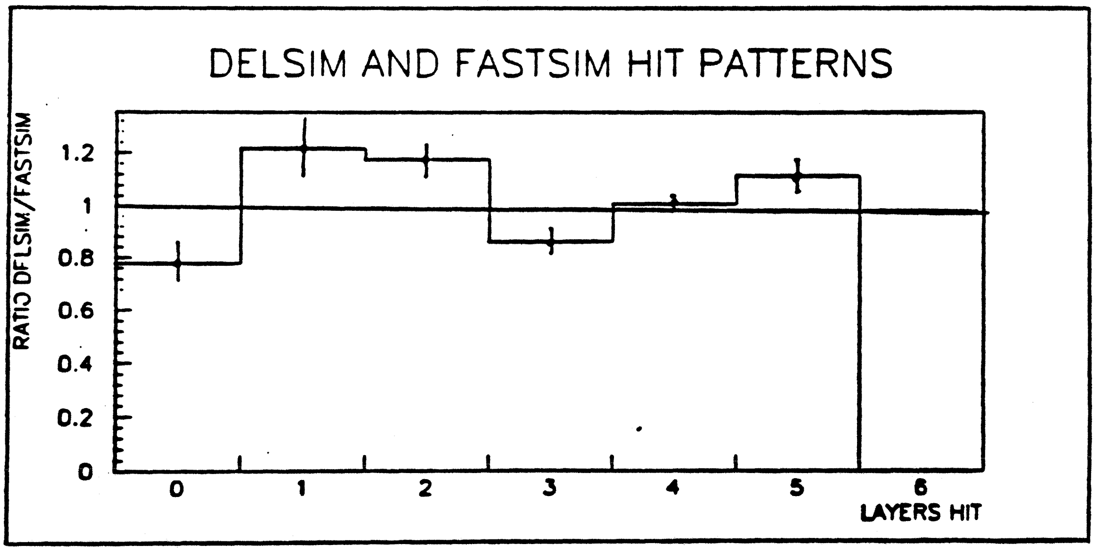

Figure 4.9: Ratio of layers hit in DELSIM and FASTSIM (column 4 of table 4.2).

4.4.2 Acceptance of Muon Chambers

FASTSIM provides a quick and simple way of studying the geometrical acceptance of the Muon Chambers. All numbers in this section are based on a sample of 10000 muon-pair events, which were simulated by FASTSIM in 41 minutes of CPU on a VAX8700.

The geometrical acceptance of the Muon Chambers is a fairly complicated function of the polar angle θ. This is demonstrated in figure 4.10 for two different muon identification criteria:

1. 'Loose' Criterion: a muon is assumed to have been positively identified if at least one layer is hit in the MUB or the MUF;

2. 'Strong' Criterion: a muon is assumed to have been positively identified if at least one layer is hit in...

   - the MUB Inners **and** the MUB Outers, **or...**
   - the MUF Inners **and** the MUF Outers, **or...**
   - the MUB Peripherals

Figure 4.10(a) shows the generated polar angle θ (measured with respect to the electron beam) of the μ^- for all events in which exactly two charged tracks were seen. Figure 4.10(b) shows the muon polar angle for that subset of events ($90.8 \pm 0.3\%$) where the μ^{-1} is identified in the Muon Chambers according to the 'loose' criterion. Dead areas are evident at $\theta = 90°$ (because each MUB chamber extends over only half the length of the Barrel) and at around $\theta = 50°$ and $\theta = 130°$, where there is a gap between the MUB and the MUF[14]. Figure 4.10(c) is the same distribution for muons selected by the 'strong' criterion ($83.5 \pm 0.4\%$).

It is also instructive to plot the number of Barrel Muon Chamber layer hit in each arm of a muon-pair event for different angular regions. Let us divide events with two charged tracks reconstructed into the following classes:

[14]Because the End-Cap Muon Chambers are mounted in large quadrants, they *do* in fact cover certain azimuthal angles at polar angles between 40° and 50°.

1. Events in the 'barrel region': at least one of the charged tracks must have polar angle $50^\circ \leq \theta \leq 130^\circ$. This angular range was used in the 1989 DELPHI leptonic analyses [55] and roughly corresponds to the range covered by the Inners (which is larger than the range in polar angle covered by the Outers and Peripherals of course).

2. Events in the 'extended barrel region': at least one charged track must have $43^\circ \leq \theta \leq 137^\circ$. This angular range will be used in the muon-pair analysis of Chapter 5. It extends well beyond the range covered by the Barrel Muon Chambers.

Figure 4.11 shows 'lego' plots of the number of Barrel Muon Chamber layers hit in FASTSIM for muon-pair events which fall into these two regions. There are 6130 events in the extended barrel region and 5205 events in the barrel region. The most common occurrence is a hit in four layers for both muons. The number of events in each bin is also shown, from which it is possible to read off estimated geometrical efficiencies of different muon-pair selection procedure.

For example, if we require that both the μ^+ and the μ^- give at least one hit, we miss 1459 events in the 'extended barrel' and 534 events in the 'barrel', corresponding to Barrel Muon Chamber identification efficiencies of $76.2 \pm 0.5\%$ and $89.7 \pm 0.4\%$ respectively. The μ^- single track efficiencies (the percentages of events in which there is at least one hit on the μ^- track) are $78.8 \pm 0.5\%$ and $92.9 \pm 0.4\%$ for the 'extended barrel' and 'barrel' regions respectively. Clearly, the probabilities of identification for the two muons are not independent.

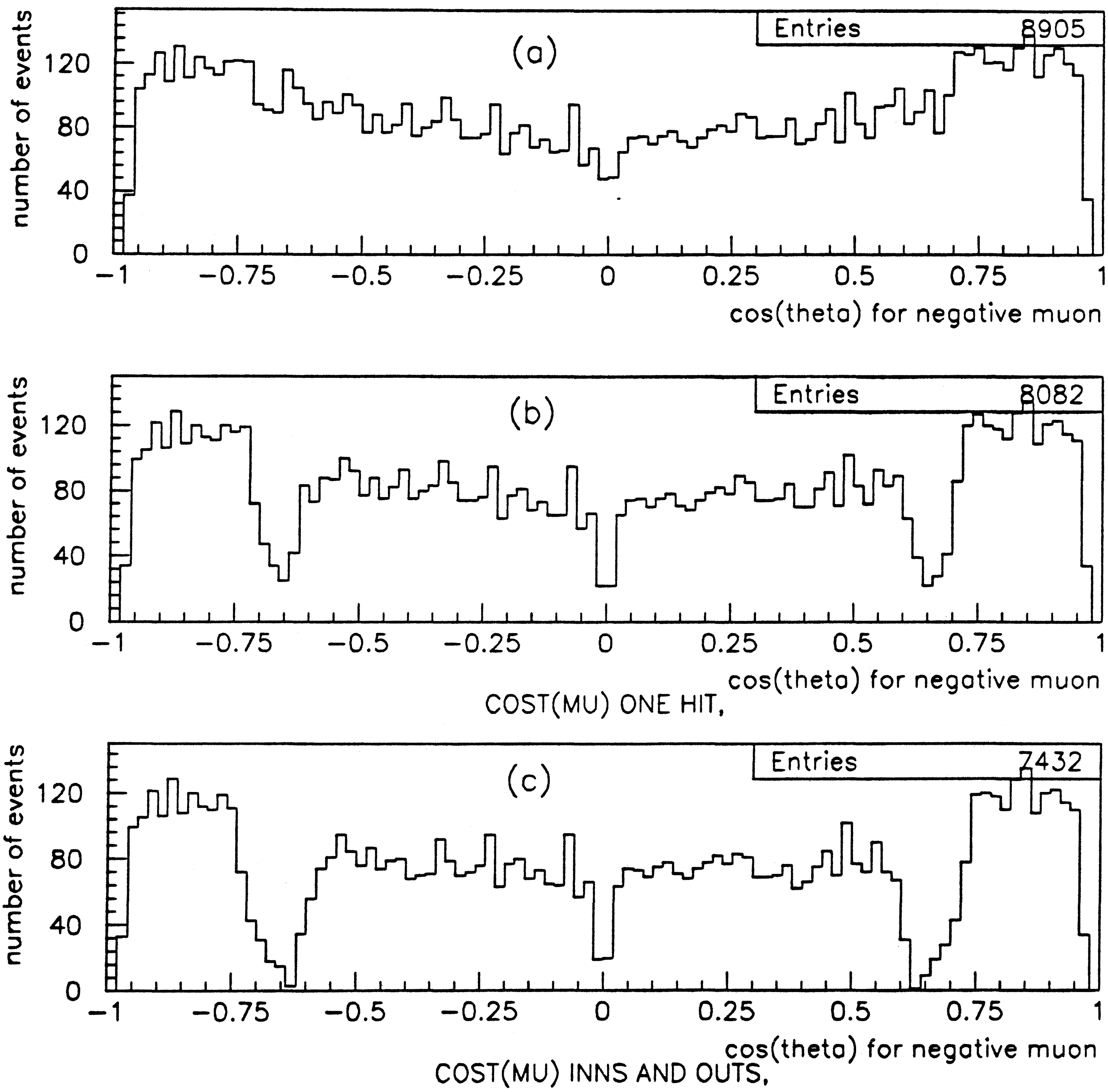

Figure 4.10: Angular acceptance of Muon Chambers according to FASTSIM. (a) Generated $\cos\theta$ distribution of μ^- in all events where there are two charged tracks reconstructed. (b) The $\cos\theta$ distribution of all μ^- identified by 'loose' criterion (see text). (c) The $\cos\theta$ distribution of all μ^- identified using 'strong' criterion (see text).

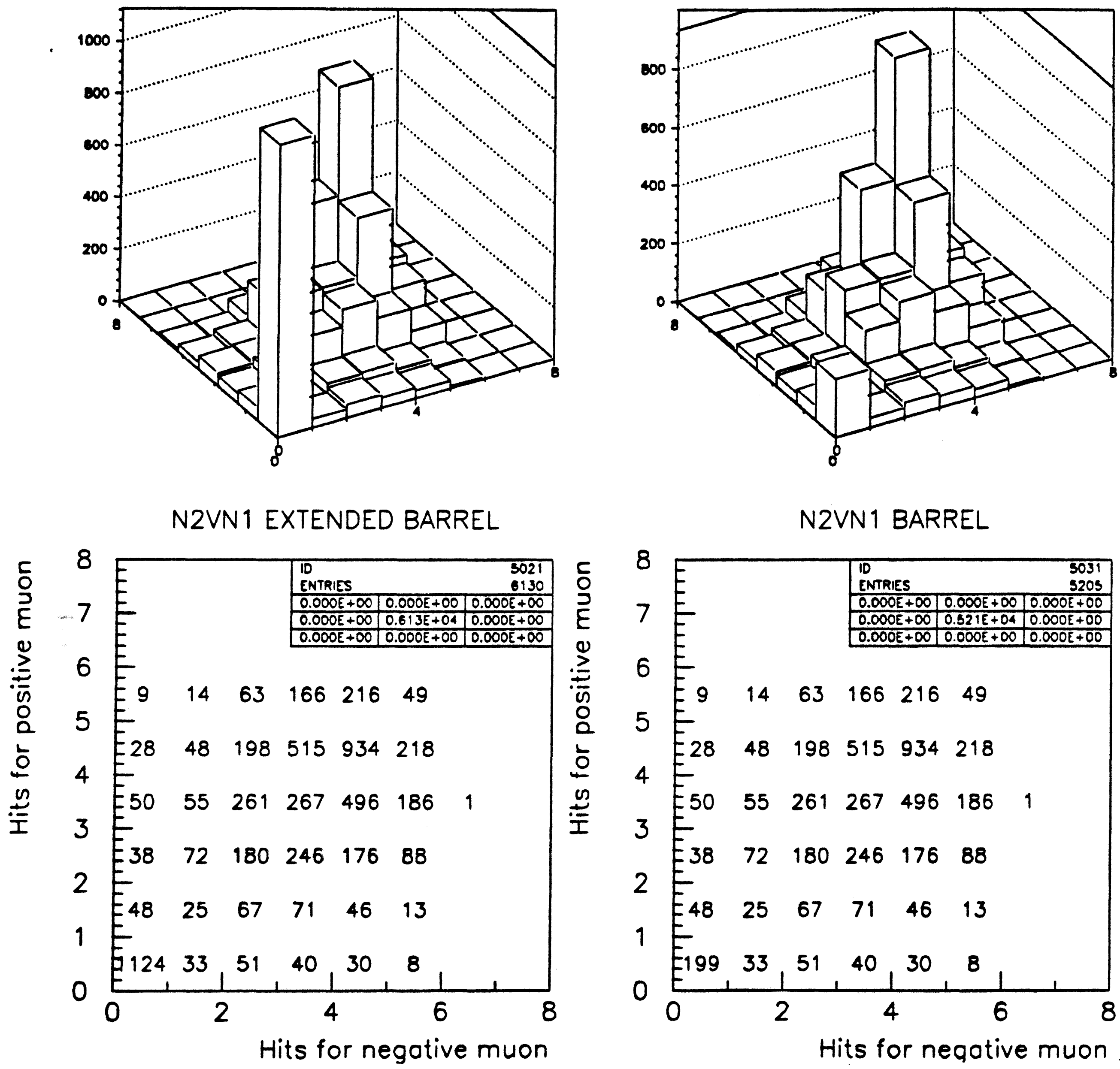

Figure 4.11: Lego plots and bin contents showing the number of Muon Chamber layers hit in each arm of a muon-pair event, according to FASTSIM, for events in the 'extended barrel region' (left), and the 'barrel' region (right).

Chapter 5

Data Reduction and Event Selection

This chapter describes the selection of muon-pair candidate events and the techniques used to estimate backgrounds and inefficiencies.

5.1 Data Collection

The analysis in this chapter is based on data taken during 1990[1]. In that year, LEP physics runs took place from April 23$^{\rm rd}$ to August 29$^{\rm th}$. The corresponding LEP Fills were 185 to 415[2]. The analysis in this chapter is based on the data taken up to the end of fill 350 (July 15$^{\rm th}$, 1990)[3].

Data were taken at seven different nominal centre-of-mass energies between about 88.3 GeV and 94.3 GeV.

During many of these runs, there was only one trigger for the $\mu^+\mu^-$ channel in the forward region. Track reconstruction efficiency in the forward region was low (about $60-80\%$) due to hardware problems and the lack of accurate knowledge of alignment between detectors. Consequently, the efficiency of muon-pair tagging was also low and difficult to estimate.

Therefore, this analysis is restricted to the angular range:

- $43° \leq \theta \leq 137°$

where θ is the polar angle with respect to the incident e^- direction (the DELPHI z-axis). This range — known as 'the extended barrel region' — is determined by the acceptance of the Outer Detector, which is used in both the trigger and the track reconstruction.

[1]As mentioned in Chapter 2, there were LEP physics runs in 1989 also, but the performance of the detector at that time did not meet the requirements of section 5.3.

[2]This corresponded to DELPHI DAS runs 7419 to 15829.

[3]i.e. up to and including DELPHI DAS run 13620.

5.1.1 Detectors

This analysis uses information from a subset of the detectors in DELPHI. Tracks were formed from hits in combinations of the following detectors: the Inner Detector(ID), the Time Projection Chamber (TPC) and the Outer Detector(OD). Muon identification was performed using the barrel electromagnetic calorimeter (HPC), the Hadron Calorimeter (HCAL), and the Barrel Muon Chambers (MUB). Luminosity measurements were made with the Small Angle Tagger (SAT). The Time-of-Flight Counters (TOF) were used in the trigger.

5.1.2 Trigger

Initially, the trigger for most muon-pair candidate events was provided by at least one of the following sub-triggers (which were 'OR'ed):

- Coincidences of back-to-back TOF sectors
- Coincidences between ID and OD requiring back-to-back tracks
- Coincidence of any TOF and any OD signals

Further triggers became available during the 1990 running including:

- The ID and OD 'majority' trigger
- TPC single track trigg[illegible]

The trigger efficiency [illegible] μ-pair samples (see section 5.7.1).

5.2 Data Reduction for 1990 Data

The raw data[4] was processed 'offline' by the DELPHI reconstruction and analysis package, DELANA (see section 4.1.3). Several stages of data reduction followed:

Leptonic Tagging

In the first stage of data reduction, events were selected (or 'tagged') as likely leptonic candidates. The tagging criteria were designed to reject background events (beam-gas, beam-wall, cosmics) and hadronic events (which tend to have a large number of charged tracks).

Events tagged as being likely leptonic candidates had ≤ 8 charged tracks and **either**:

- $N_{ch} \geq 1$ where N_{ch} was the number of charged tracks with momentum $p > 2$ GeV, AND
- $N'_{ch} \geq 1$ where N'_{ch} was the number of charged tracks with impact parameter at the origin < 8 cm in the xy-plane and < 10 cm from $z = 0$;

or

- Energy sum in the event, $ESUM > 8$ GeV,

where $ESUM$ is the sum of the visible energy in the tracks and in the electromagnetic calorimeters[5]. With the exception of the calculation of the energy in the Forward Electromagnetic Calorimeter (FEMC), this code used DST data as input.

In parallel to this, *additional* events were tagged which had no charged tracks but which had roughly back-to-back muonic signals in the MUB, MUF, HPC, and FEMC. This 'Team 2' tagging was mainly designed to exploit areas of the forward region where track reconstruction efficiency is low. Such low topology events are not used in this analysis.

Selected events were written to so-called 'Leptonic Master-DSTs', which contained raw data, TANAGRA Data and DST Data, stored on IBM 3480 cassettes.

[4]i.e. the data as written to disk at the DELPHI pit. See Appendix B.
[5]Note that double counting is allowed.

Oxford Tagging

Raw and TANAGRA data for events with fast, charged tracks in the barrel region were stripped off the Leptonic Master-DSTs and copied to compact EXABYTE cassettes for transportation to Oxford. This exercise reduced the data volume by about one third. Tagged events had:

- **either** at least one charged track in the extended barrel region with momentum $p > 10$ GeV
- **or** at least two and not more than 6 charged tracks in extended barrel region with momentum $p > 1$ GeV

N-tuple Production

EXABYTE cassettes contained a total of nearly 18000 Oxford-tagged events (approximately 5 GBytes of data). Each event could have a few hundred variables which were of interest for this analysis. To collect together these variables, we have used a special analysis program 'GEDTAN', which is written entirely by the author. This program interrogates TANAGRA data only, and only those TANAGRA banks created after detector-specific processing and local pattern recognition (TEs), and those produced after the track search and fit (TKs). In this way, we hope to minimise errors due to the use of software which is not fully optimised for the performance levels which the detectors reached in 1989-90, or which may not have been fully exercised and documented, and to obtain the maximum available amount of information which is relevant to a muon-pair analysis.

Useful quantities were saved in an HBOOK[6] 'N-tuple' in a RZ direct access file [34]. The N-tuple was used here mainly as a micro-DST, but in conjunction with the PAW [47] package it may also provide a means for data presentation and interactive analysis. The N-tuple was filled for all events satisfying the following criteria:

- exactly two charged tracks with momentum $p > 5$ GeV;

[6] HBOOK is a histogramming, fitting and data presentation package [43] developed at CERN.

- the event came from a run where all relevant detectors were working (see section 5.3).

5.3 Run Selection

The status of the detectors, the triggers and the Solenoid varied substantially from day to day (especially during 1989 and the first few months of the 1990 running). The status of the various components of DELPHI was recorded on a run-by-run basis in the files RUNSEL89 and RUNSEL90 [44]. From these files a list of 'good' runs for fills 185 to 350 was produced. We imposed the following conditions on 'good' runs:

- the current in magnet $I_{mag} \geq 5000$ A (corresponding to nominal field of 1.22 T)
- $\geq 95\%$ of TPC, OD, and HCAL in nominal working condition
- $\geq 90\%$ of MUB and HPC in nominal working condition
- $\geq 95\%$ of ID, TOF and SAT triggers in nominal working condition
- $\geq 90\%$ of OD trigger in nominal working condition
- data from the whole run were input to Oxford tagging and copied to EXABYTE

5.4 Muon-Pair Selection Criteria

In this section we summarise how candidate muon pair events were selected from the quantities in the N-tuple.

We select two track events with the following features:

- **'momentum cut':** exactly two charged tracks with momentum $p \geq 15$ GeV; no further charged tracks with momentum $p \geq 5$ GeV;
- **'barrel cut':** at least one of these two charged tracks has polar angle θ at the origin such that $43° \leq \theta \leq 137°$;
- **'vertex cut':** both charged tracks satisfy $r_0 \leq 0.8$ cm and -4.5 cm$\leq z_0 \leq 3.5$ cm, where r_0 and z_0 are the distances from the origin of the DELPHI coordinate frame in the xy-plane and in z respectively, measured at minimum r;
- **'acolinearity cut':** the 'acolinearity' between the two charged tracks $acol \leq 10°$ (see eqn. 5.2 for precise definition of $acol$) .

Events which pass all these cuts will be referred to as **'barrel two track events'**.

For an event to be selected as a muon-pair candidate we require that **each** of the two tracks is identified as a muon in **one** or more of the three detectors. That is, we demand:

- Track 1 is identified as a muon in **either** the HPC, **or** the HCAL, **or** the MUB.

AND

- Track 2 is identified as a muon in **either** the HPC, **or** the HCAL, **or** the MUB.

2725 barrel two track events were selected, of which 1322 events were muon-pair candidates. These selection criteria will be explained in sections 5.5 and 5.6.

5.4.1 Simulation Studies

Comparison will be made with simulated data samples. Events in these samples were generated with centre-of-mass energy $\sqrt{s}$ near the Z^0 peak, and with most important radiative corrections taken into account. They were then passed through the DELPHI full simulation program DELSIM, reconstructed by DELANA as if they were real events, and passed through exactly the same chain of data reduction and analysis that was used for the real data (except for the 'Leptonic Tagging'). The simulations used were:

- 3900 $\mu^+\mu^-$ events generated over the full angular range with DYMU3 [13].
- 7499 $\tau^+\tau^-$ events generated over the full angular range with KORALZ [45].
- 803 e^+e^- events generated over angles $45° \leq \theta \leq 135°$ range with the BABAMC generator [46].

5.5 Selection of 'Barrel Two Track Events'

Assuming the incident electron and positron have the same energy and neglecting radiative effects, muon-pairs from Z^0 decay are produced 'back-to-back' in the laboratory frame, each with the energy E_B of one of the beams, and each originating from the interaction region (which is centred close to the origin of the DELPHI coordinate frame) at the time the beams cross (the Beam Cross-Over or BCO). The muons are highly relativistic and to a good approximation their momenta are equal to their energies. Radiative effects lead to the final state muons having momenta slightly less than E_B and not emerging back-to-back.

5.5.1 Momentum Cut

The momentum is obtained from the curvature of the charged track in the magnetic field of the Solenoid. High momentum tracks are very straight[7] so good detector alignment is critical for good momentum resolution and accurate charge determination. Figure 5.1 illustrates the average momentum resolution for $z < 0$ and $z > 0$ separately (this corresponds to the two halves of the TPC) in 1990[8]. The inverse of the magnitude of the three-momentum, multiplied by the measured charge on the track and the beam energy, is shown for all muon-pair candidates. From two-Gaussian fits to these two distributions we obtain standard deviations σ_i where

$$\begin{aligned} \frac{\delta p}{p} &= p\left|\delta\left(\frac{1}{p}\right)\right| \\ &= \frac{p}{E_B}\left|\delta\left(\frac{E_B}{p}\right)\right| \\ &= \frac{p}{E_B}\,\sigma_i \\ &\approx \sigma_i \end{aligned} \tag{5.1}$$

since in general $p_\mu \approx E_B$. The momentum resolution obtained by this method is $11.0 \pm 0.6\%$ and $10.5 \pm 0.5\%$ for negatively and positively charged tracks tracks

[7]Radius of curvature ρ of a charged track in a magnetic field B is given by

$$\rho = p_T[GeV] \times 10^9/cB$$

where c is the speed of light and p_T is the momentum of the particle transverse to the magnetic field. For a $p_T = 45$ GeV track in DELPHI (B=1.2 T) we find $\rho \approx 125$ m.

[8]Detailed studies showed the momentum resolution to be time-dependent.

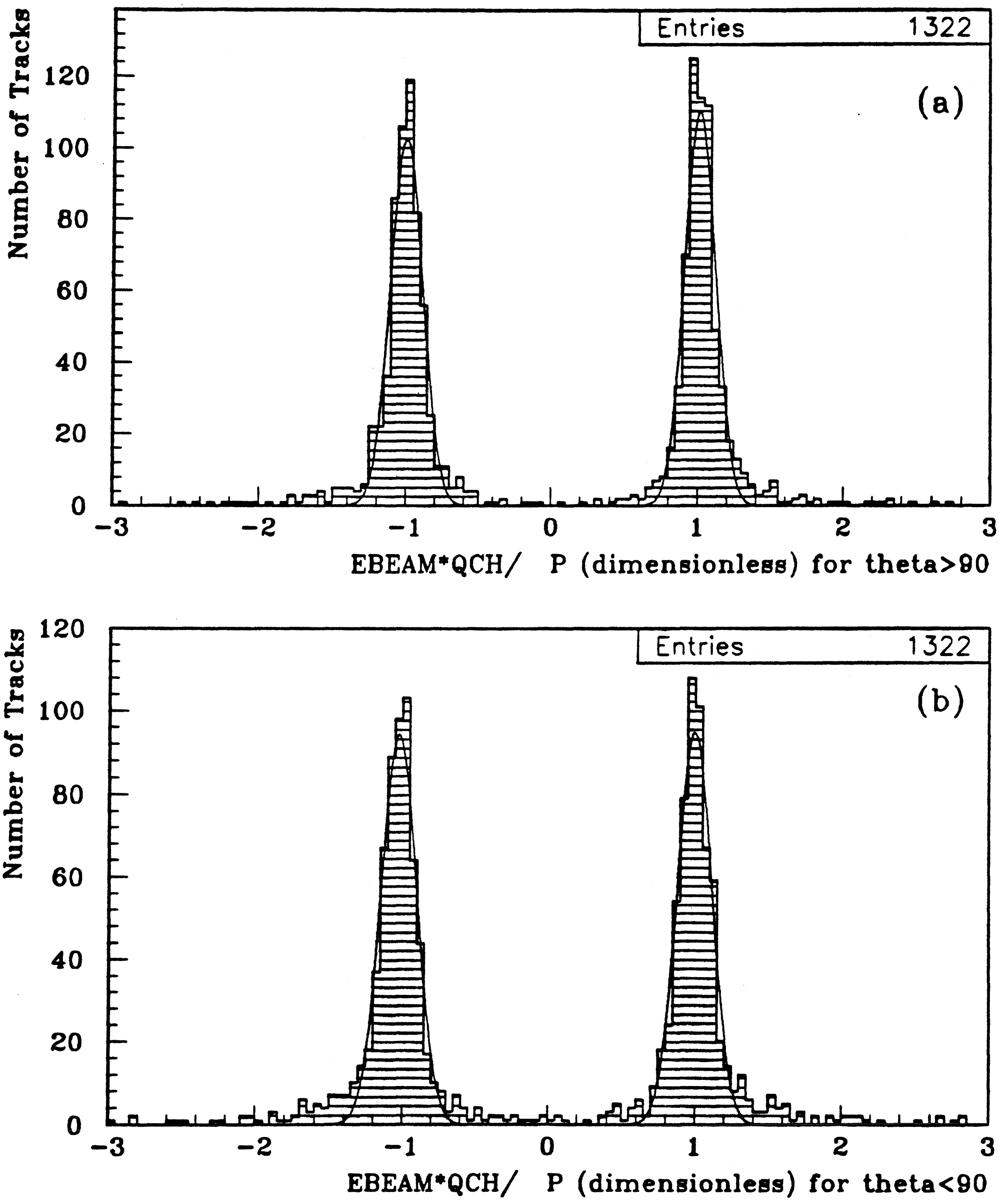

Figure 5.1: Momentum resolution in the 1322 candidate muon-pair events for: (a) $\theta > 90°$, or equivalently $z < 0$, and (b) $\theta < 90°$, $z > 0$. A two-Gaussian fit is made to each distribution (see text).

respectively in the region $\theta > 90°$. The corresponding figures for $\theta < 90°$ are slightly worse: $12.0 \pm 0.6\%$ and $11.7 \pm 0.5\%$ respectively.

The distribution has non-Gaussian tails that are due mainly to radiative effects and the contamination of this sample by $\tau^+\tau^-$ events. To demonstrate this, figure 5.2 shows a comparison of the momentum distribution of the muons in $\mu^+\mu^-$ events for the real data and the simulated data. A further cut of *acol* $\leq 1°$ has been applied for the purpose of this study to both samples, in order to reduce the tau contamination in the real data sample[9], leaving 1130 real data events and 1978 events from the $\mu^+\mu^-$ simulation. The real data distribution is seen to be slightly broader than the simulation and slightly offset. Figure 5.2(b) and 5.2(c) show in more detail lower 'tail' of the distribution: that is, the muon tracks between 15 and 25 GeV. The fraction of tracks with momentum between 15 GeV and 20 GeV is $0.31 \pm 0.11\%$ in the real data and about $0.25 \pm 0.07\%$ for the $\mu^+\mu^-$ simulated data (with a small contamination of $\tau^+\tau^-$ events as predicted by the simulations (see section 5.8.1)).

We conclude that a momentum cut of 20 GeV would probably not lead to significant errors. However, a cut of 15 GeV is employed in this analysis for safety.

5.5.2 Vertex Cut

The Vertex Detector was not in general used in the track fit in 1990. The first measured point on the track may be some tens of centimetres from the interaction region (IR). We need to know if the track came from the interaction region in order to distinguish muon-pairs from cosmic muons.

Since muon-pairs are very nearly back-to-back in the 'laboratory' frame, if one attempts to find an event vertex from the two tracks then small errors in measurement of track direction and momentum may lead to very large errors in the calculated vertex position. Hence, we simply extrapolate each charged track separately towards the origin of the DELPHI frame, taking into account the bending in the magnetic field, and attempt to find the z position z_0 and perigee r_0, *at the perigee*[10]. We performed the extrapolation using the FASTSIM

[9] Simulations predict the $\tau^+\tau^-$ background in this sample to be $0.5 \pm 0.1\%$.

[10] 'Perigee' usually means the point in the orbit of the moon at which it is nearest to the Earth (according to the Shorter Oxford English Dictionary) but is often used within DELPHI for the minimum distance of approach to the z axis *in the x, y-plane* i.e. the minimum value of $R = \sqrt{x^2 + y^2}$.

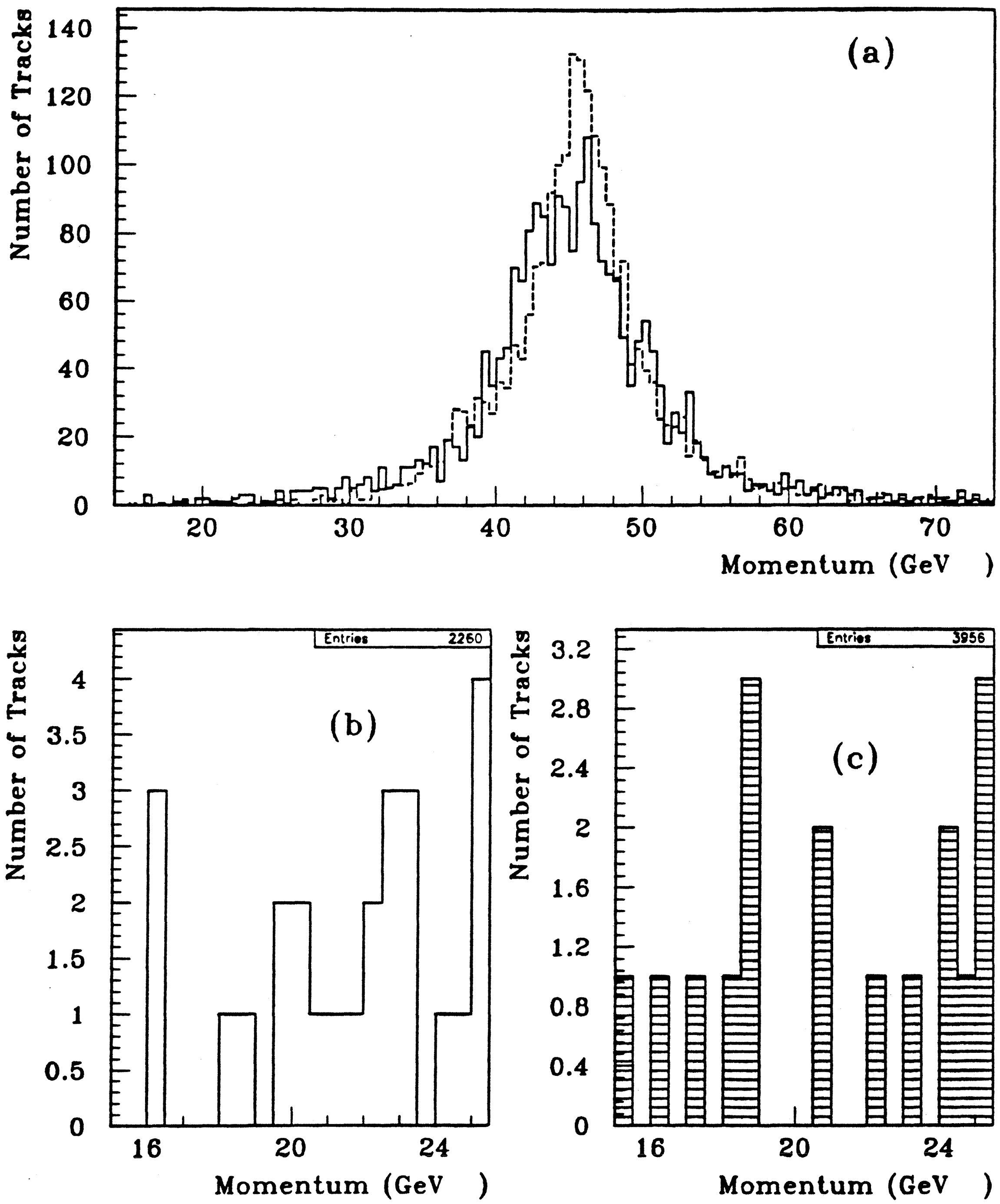

Figure 5.2: (a) Comparison of the momentum distribution of muons in candidate muon-pair (full line) with $\mu^+\mu^-$ simulation (dashed line). The events plotted passed the usual selection criteria, and additionally *acol* $\leq 1°$. The distribution for the simulated data is scaled by a factor 2260/3956, to give the same total number of tracks as in the real data. Figures (b) and (c) show details of the distribution towards the low end for the real and simulated data respectively (simulated data is unscaled in (c)).

tracking routine [40], and all kinematic quantities used in the analysis are the calculated values at the track origin.

Figure 5.3 shows r_0 and z_0 for candidate events which pass all the cuts outlined in section 5.4 (momentum, barrel, acolinearity, muon identification) *except the vertex cut*. The same distributions are shown with hatching for events which have a large energy deposit[11] associated to each track in the barrel electromagnetic calorimeter (such events are good e^+e^- candidates and are very unlikely to be cosmic muons). Also shown is a scatter-plot of z_0 against r_0 for the dimuon sample, which is seen to be approximately uniformly populated away from the vertex region.

Notice that the reconstructed beam spot is slightly displaced from the central plane ($z = 0$) of DELPHI. The vertex cut described above permits approximately 4 cm either side of the mean value of z_0.

5.5.3 Acolinearity Cut

The acolinearity is defined by

$$acol = 180.0 - \arccos\left(\frac{\mathbf{p}_1^{\mu}\cdot\mathbf{p}_2^{\mu}}{|\mathbf{p}_1^{\mu}|\ |\mathbf{p}_2^{\mu}|}\right) \tag{5.2}$$

where $\mathbf{p}_1^{\mu}$ and $\mathbf{p}_2^{\mu}$ are the three-momenta of the two muons. Figure 5.4(a) shows the distribution of acolinearity for real data candidate muon-pair events which pass all cuts of section 5.4 *except the acolinearity cut* (note the log scale on the y-axis).

For muon-pairs events the acolinearity is usually less than 1°, while for $e^+e^-\rightarrow\tau^+\tau^-$ events acolinearities between about 1° and 3° are more typical. This is demonstrated in figure 5.4(b) for simulated data. For certain studies (e.g. the study of the momentum distribution in section 5.5.1) an acolinearity cut of 1° is therefore a powerful way of reducing the tau background and obtaining a clean muon-pair sample. It is also possible to get an estimate of the $\tau^+\tau^-$ background from the real data acolinearity angle distribution (see section 5.8.1). However, the agreement in the acolinearity distribution between simulated and real $\mu^+\mu^-$

[11]The tracks have $E_{25}(HPC) \geq 35$ GeV, which essentially means that there is more than 35 GeV deposited in the barrel electromagnetic calorimeter close to this track. See section 5.6.1 for an exact definition.

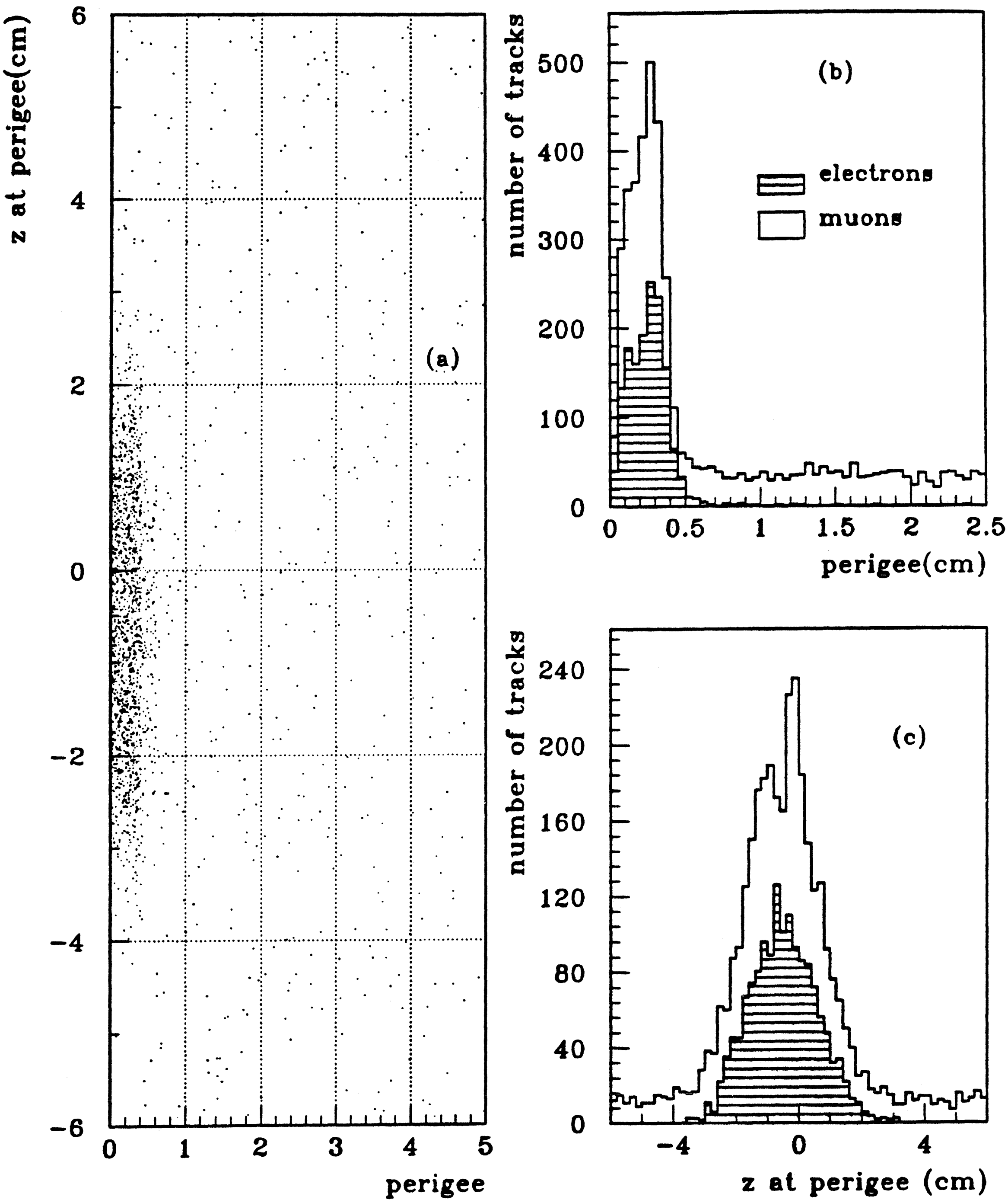

Figure 5.3: Scatter plot (a) shows z_0 against r_0 for the muon-pair events. These events pass all cuts of section 5.4 *except the vertex cut*. The distribution of r_0 and z_0 is shown in (b) and (c) respectively. The hatched distributions contain good e^+e^- pair candidate events.

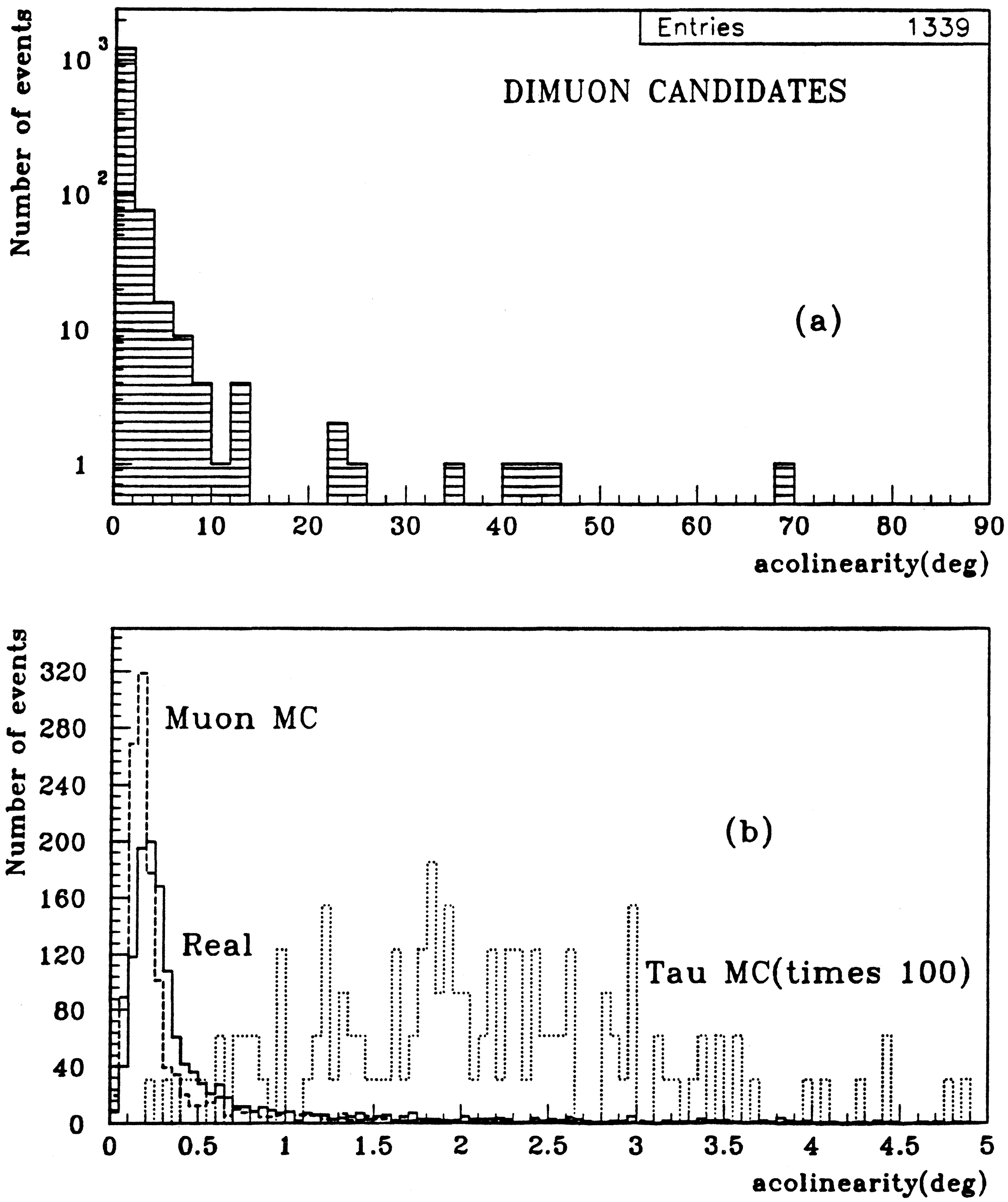

Figure 5.4: (a) Acolinearity distributions in real data for candidate dimuon events that pass all other cuts. (b) Comparison of acolinearity distributions in real data (solid line), $\mu^+\mu^-$ simulated data (dashed line), $\tau^+\tau^-$ simulated data (dotted line). Plotted events pass all the other muon-pair selection criteria of section 5.4. The simulated $\mu^+\mu^-$ distribution is scaled by a factor of 1339/2256 to give the same total number of events in the plot as for the real data. The simulated $\tau^+\tau^-$ distribution is scaled to represent approximately its contribution as a background, and further scaled by a factor of 100 for the sake of clarity.

events for this quantity is not particularly good (see again figure 5.4(b)). Around 1°, the acolinearity distribution is still falling rapidly with increasing angle. Since we want to select a sample with known efficiency and to be sure we are not discriminating against certain classes of events, we adopt a loose acolinearity cut.

In conclusion, a cut of $acol \leq 10°$ is imposed, mainly to reject against $\tau^+\tau^-$ final states. This cut removes 17 events from the muon-pair candidate sample in the real data[12], or $1.3 \pm 0.3\%$, and removes $1.3 \pm 0.2\%$ of the simulated $\mu^+\mu^-$ events (generated near the Z^0 mass) which pass all cuts except this acolinearity cut.

[12]i.e. 17 events pass all the cuts of section 5.4 except this acolinearity cut.

5.6 Particle Identification

5.6.1 High Density Projection Chamber

For high energy electrons, bremsstrahlung and pair-production processes lead to the production of electromagnetic showers in the High-Density Projection Chamber (HPC). Minimum ionising particles (MIPs) may be distinguished from electrons in the HPC by the small energy deposition. The matching of an energy deposition to a track is done in DELANA with the aid of the track extrapolation package. However, since we are only considering two track events, we use a very simple algorithm for this matching: we use a straight line extrapolation of the track as defined at the origin and look for energy deposited in the HPC within angular cuts around the track.

Apart from its simplicity, this so-called 'cone' method tends to reject more effectively against certain classes of tau background events where a charged pion (which may otherwise be classified as a muon by the HPC) is accompanied by almost colinear photons.

In figure 5.5(a) we show the energy deposited in the HPC within a 25° cone for all 'barrel two track events'. The response of the HPC to different classes of events is shown in figure 5.5(b). Finally, in figure 5.5(c) we show the energy deposition for tracks which furthermore have ≥ 3 layers hit in the MUB, and which are therefore good muon candidates.

In conclusion, we class tracks as being muons in the HPC if:

- $0.0 < E_{25}(HPC) < 2.0$ GeV

where $E_{25}(HPC)$ is the sum of the energies stored in all HPC TE banks defined at polar and azimuthal angles θ_{hpc} and ϕ_{hpc} which satisfy

- $|\phi_{hpc} - \phi| \leq 25°$ **and** $|\theta_{hpc} - \theta| \leq 25°$.

Here ϕ and θ are the angles of the track defined, as always, at the perigee.

5.6.2 Hadron Calorimeter

For the HCAL, the energy deposited in each of the four layers (or 'towers') is measured. Hadrons (mainly pions) may be expected to deposit most of their

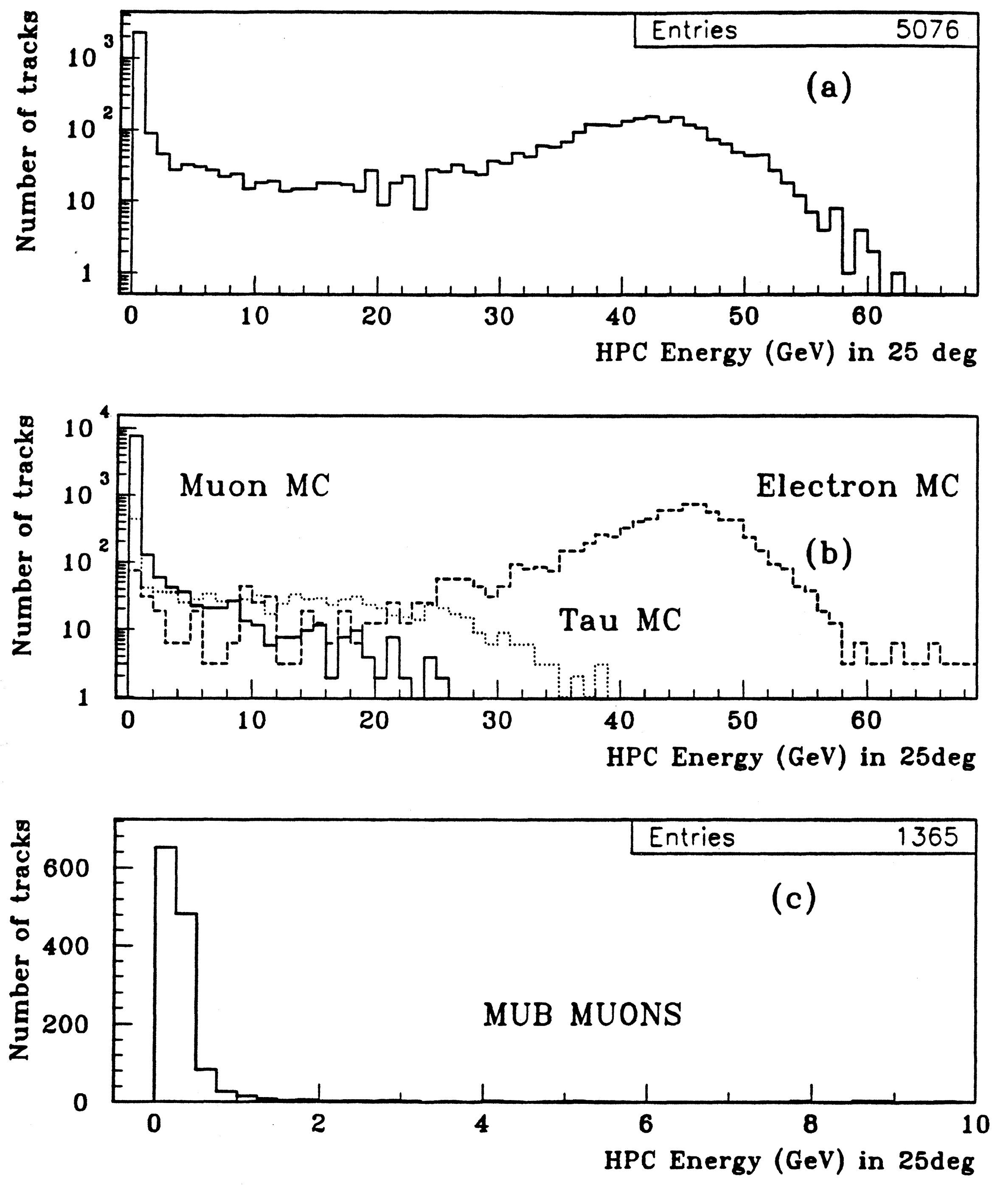

Figure 5.5: (a) The energy deposition in the HPC within a 25° 'cone' for all 'barrel two track events' in the real data. (b) The energy deposition in the HPC within a 25° 'cone' for all 'barrel two track events' for the $\mu^+\mu^-$, $\tau^+\tau^-$ and e^+e^- simulations. The distributions are scaled to take approximately into account the Monte Carlo statistics. The $\mu^+\mu^-$ distribution is scaled by 7499/3900 and the e^+e^- distribution is scaled by 7499/(803 x 1.5). (c) The energy deposition in the HPC within a 25° 'cone' for all 'barrel two track events' for tracks which had three or more layers associated to them in the MUB by EMMASS. Note that for all three plots, tracks with zero energy associated to them have not been plotted.

energy in the first two layers, due to strong interactions with the iron of the HCAL. Electrons which sneak through the electromagnetic calorimeter should mainly be contained in the first two layers as well. Muons above around 3 GeV are expected to pass through all the iron, leaving small energy deposits in all four layers.

The total energy in all four layers has an angular dependence (as demonstrated in figure 5.6(a)). We attempted to compensate for the effect by considering $E \sin^2 \theta$, which seemed to remove some of the angular dependence (figure 5.6(b)).

We look for layer energy deposits which are appropriate to MIPs and sum the number of layers with such deposits. That is, we find:

- the number of layers $NHLAY$ for which $0.0 < E_{ilay} \sin^2 \theta < 6.0$ GeV where E_{ilay} is the energy deposited in layer $ilay$ and θ is the polar angle of the track to which this energy was associated by DELANA.

The energy deposited in a layer is shown in figure 5.7 for tracks which are good muons in the MUB, in both the real and the simulated data.

Figures 5.6(c) and (d) show energy against $NHLAY$ for real data tracks which are firmly identified as muons in the MUB, and for real data tracks which have no muon signal in the MUB. We conclude that a high purity sample can be obtained with reasonable efficiency if we require:

- $NHLAY \geq 3$

for a track to be identified as a muon. No total energy cut is imposed.

5.6.3 Barrel Muon Chambers

Unlike the HPC and the HCAL, the MUB system does not cover the whole of the extended barrel region. In order to retain identification efficiency at polar angles where the track may intersect only with the Inners, we require only **one** or more MUB space points to be close to the track. This is possible as the level of 'noise' hits in the chambers was found to be negligible.

To assess the Barrel Muon Chambers performance we looked at that subset of barrel two track events which had an acolinearity angle $acol \leq 1°$ and for which

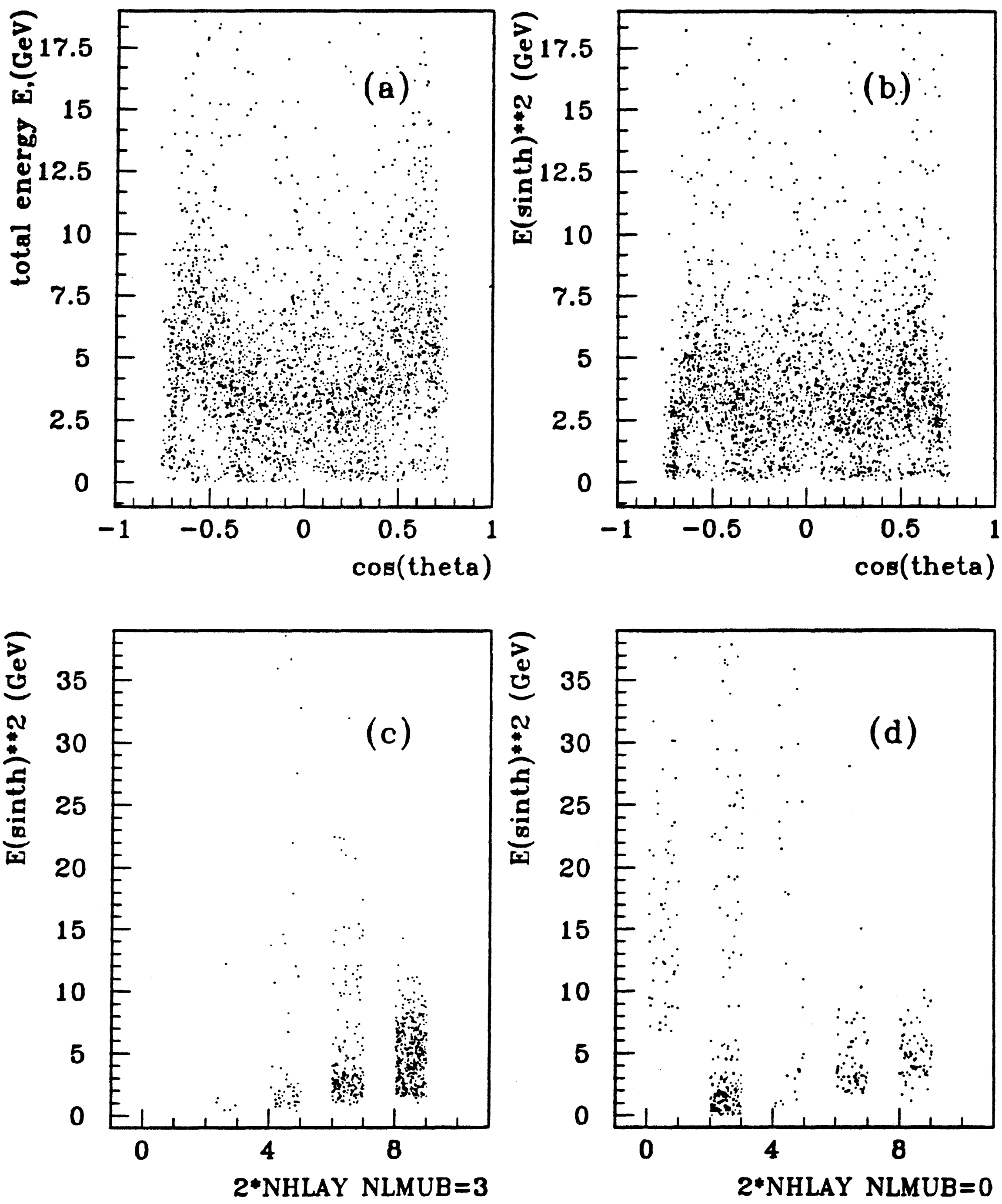

Figure 5.6: Muon identification in the HCAL. The plots are for all 'barrel two track events'. In (a) the total visible energy E associated to the track in the HCAL is plotted against $\cos\theta$. An angular dependence is seen; less energy is in general deposited by tracks with polar angle θ around 90°. In (b), $E\sin^2\theta$ is plotted against $\cos\theta$. Some of the angular dependence is removed. In (c) we plot $E\sin^2\theta$ against $2 \times NHLAY$ (see text for definition of $NHLAY$) for that subset of tracks from 'barrel two track events' which have at least three space points associated to them in the MUB. In (d), the same quantities are plotted for tracks which have no space points associated to them in the MUB, but which are within the MUB acceptance (i.e. the polar angle of the track satisfies $50° < \theta < 88°$ or $92° < \theta < 130°$).

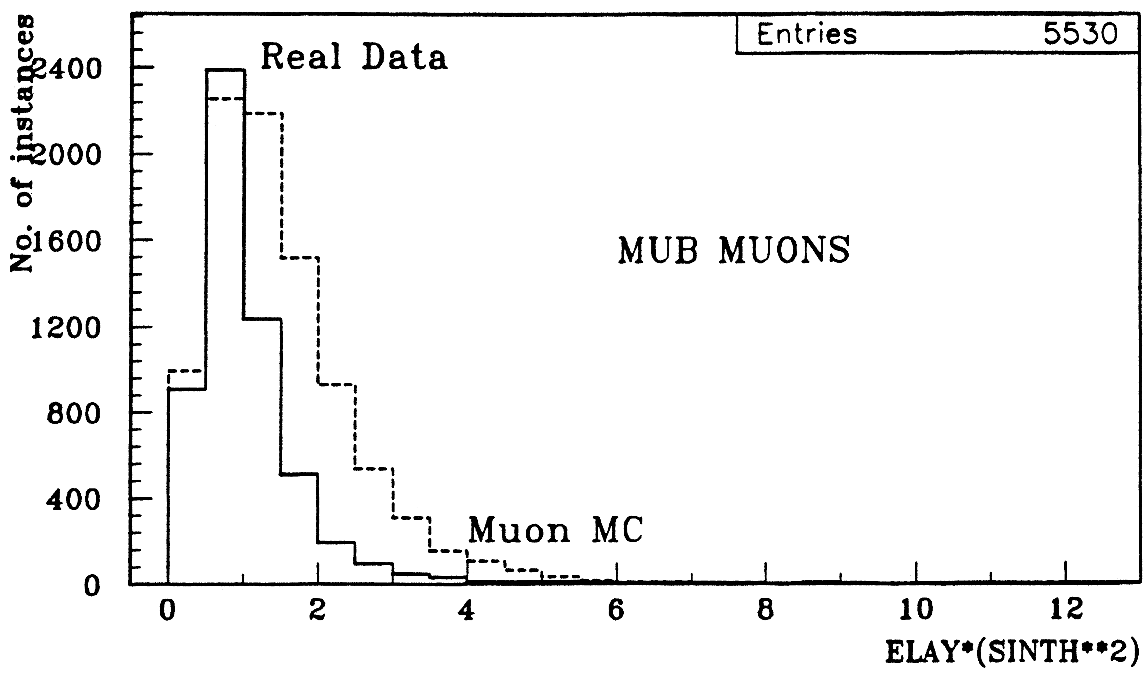

Figure 5.7: The response in a single HCAL layer (or 'tower') to tracks which are from 'barrel two track events' and have at least three space points associated to them in the MUB. $E_{ilay} \times \sin^2\theta$ is plotted for real data (solid line) and simulated $\mu^+\mu^-$ data (dashed line). The simulated distribution is scaled by 5530/9169 to correct for the number of entries.

both charged tracks had a momentum $p \geq 25$ GeV. In addition, we required that both tracks were positively identified as muons in the HPC according to the criterion of section 5.6.1. The number of space points (layers) associated to the tracks is shown in figure 5.8(a). The same plot for the simulated $\mu^+\mu^-$ sample is shown in figure 5.8(b). The global χ^2_G per degree of freedom and the χ^2 probability of the fit of the extrapolated track to the MUB hits are shown in figures 5.8(c) and (d) (clearly the χ^2_G was not correctly normalised for this data production).

In summary, a track is classified as a muon in the Barrel Muon Chambers if:

- ≥ 1 MUB space point associated to the track by EMMASS, with a cut on the χ^2_G (see section 4.3) such that the χ^2 probability ≥ 0.03.

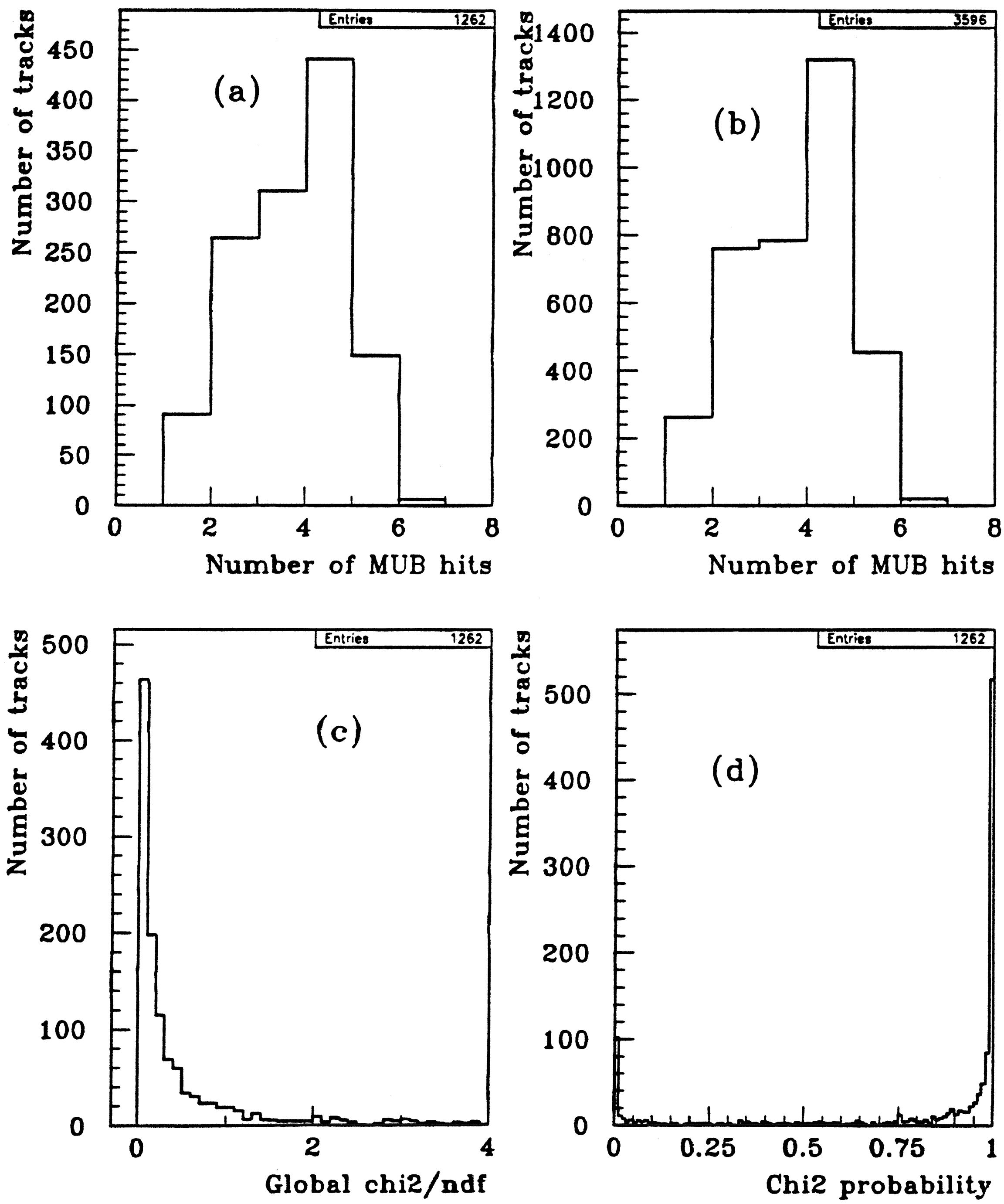

Figure 5.8: (a) The number of space points in MUB associated to likely muon tracks by EMMASS. (b) The same plot for the simulated $\mu^+\mu^-$ sample. (Tracks with zero space points associated are not plotted). (c) The global χ^2_G per degree of freedom in the real data sample and (d) the probability distribution for this χ^2_G.

5.7 Efficiencies

It is of course essential to know what proportion of the muon-pairs produced in DELPHI were actually detected. A variety of methods have been used to determine the various efficiencies and acceptances; where possible, we have relied on techniques using real rather than simulated data.

In the following discussions one should bear in mind that the total number of muon-pair candidate events near the Z^0 peak, 937, has a *statistical* error of about 3.3%.

5.7.1 Trigger Efficiency

The trigger efficiency for barrel muon-pair events was always greater than 90%. Up to run 9632, the overall efficiency was relatively low due to a hardware fault in the ID-OD back-to-back trigger[13]. For the later runs, the efficiency was close to 100% in the extended barrel region, as this fault was fixed and new triggers were introduced.

We scaled event numbers using the trigger efficiencies given in table 5.1 (which are all from [48]). These trigger efficiencies were determined using a real data muon-pair sample. Wherever there is redundancy between triggers, events triggered by one trigger may be used to calculate the efficiencies of the other(s).

Runs	Trigger efficiency
7419 to 9632	$92.0\% \pm 1.3(stat) \pm 0.6(sys)$
9633 to 10499	$99.2\% \pm 0.3(stat) \pm 0.2(sys)$
10500 to 10627	$98.1\% \pm 1.3(stat) \pm 0.0(sys)$
10628 onwards	$99.2\% \pm 0.1(stat) \pm 0.1(sys)$

Table 5.1: Trigger Efficiencies for Muon-Pair events satisfying $43° \leq \theta \leq 137°$.

5.7.2 Muon Identification Efficiency

We attempted to calculate the efficiency for the correct identification of a muon track using real data. In order to reduce the contamination due to tau-pair

[13] The inefficiency was in certain azimuthal (ϕ) regions, for all angles of θ.

events, we considered that subset of the barrel two track events which satisfied the following more restrictive cuts:

- a tighter momentum cut: exactly two charged tracks with momentum $p \geq 25$ GeV
- a tighter acolinearity cut: $acol \leq 1°$

In the real data sample, of the 2725 barrel two track events, 1956 survived after these cuts. Of 7499 simulated $\tau^+\tau^-$ events, 598 were barrel two track events, but only 34 (< 0.5% of the original sample) passed these more restrictive cuts as well. From 3900 simulated $\mu^+\mu^-$ events, 2257 were barrel two track events, and 1984 events passed the additional cuts of this section.

For tracks which were identified as muons in **either** detector i **or** detector j, we obtained two numbers for detector k:

1. $N_k(YES)$ = number of such tracks identified as a muon in detector k
2. $N_k(NO)$ = number of such tracks not identified as a muon in detector k

We then calculated the single track muon identification efficiencies, $\epsilon_k(sing)$ for the three detectors ($k = HPC, HCAL, MUB$) using the relation:

$$\epsilon_k(sing) = \frac{N_k(YES)}{N_k(YES) + N_k(NO)} \tag{5.3}$$

The results were:

- $\epsilon_{HPC}(sing) = 84.2 \pm 0.8\%$,
- $\epsilon_{HCAL}(sing) = 85.8 \pm 0.7\%$,
- $\epsilon_{MUB}(sing) = 71.2 \pm 1.0\%$,

A simple 'OR' of these three efficiencies (which assumes that the three efficiencies may be treated as independent probabilities) gives $\epsilon^{OR}(sing) = 99.4 \pm 0.1\%$.

The efficiency for the MUB is lowest because it does not cover the whole of the angular range of our analysis. In general, all these efficiencies depend quite strongly on θ, as shown in figure 5.9. There is a common decrease in efficiency ('correlated inefficiency') towards the extremes of the allowed angular

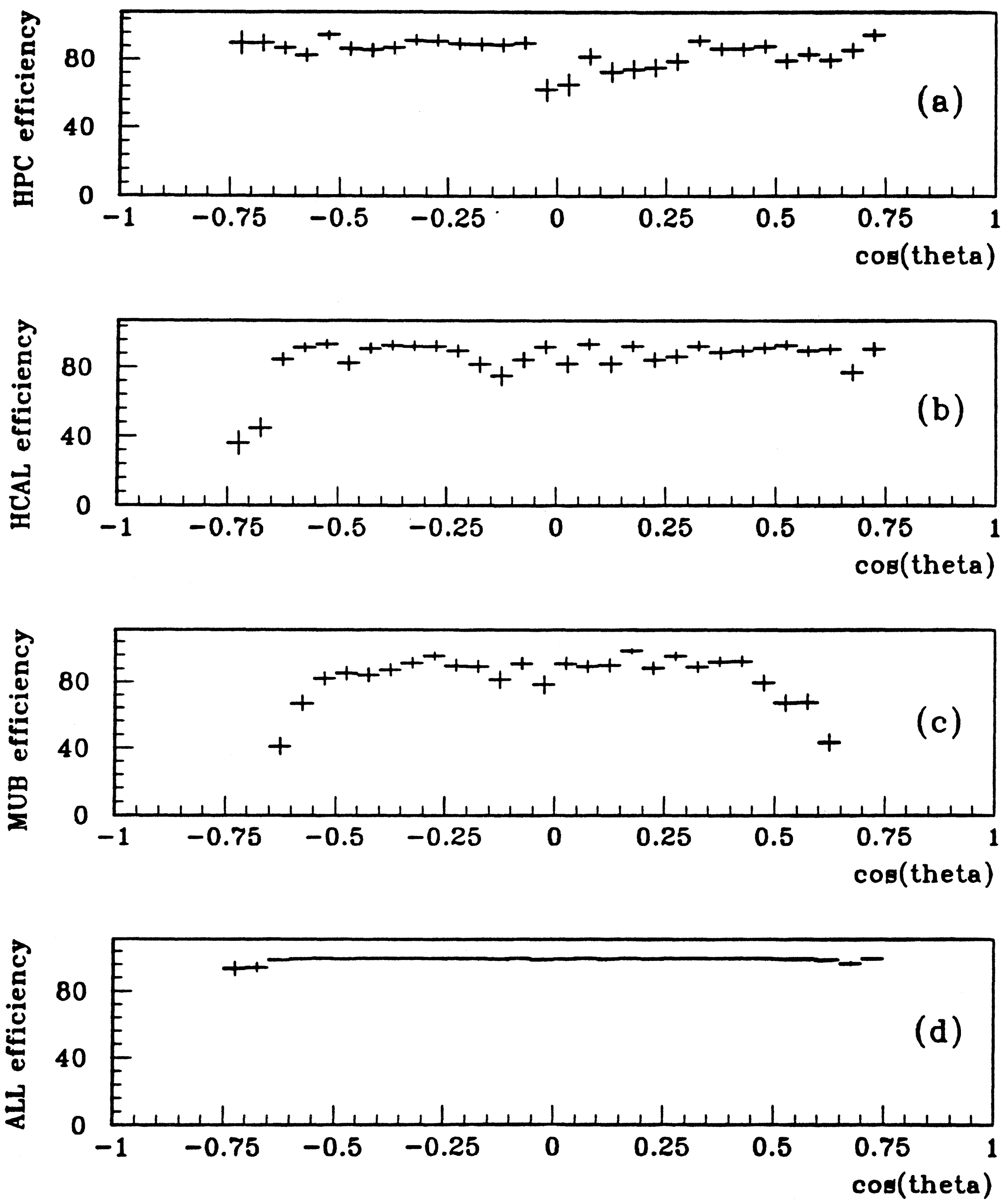

Figure 5.9: Calculated single track muon identification efficiencies as a function of $\cos\theta$ in the real data for (a) HPC, (b) HCAL, (c) MUB, (d) a simple 'OR' of the three detectors in each of the 40 $\cos\theta$ bins

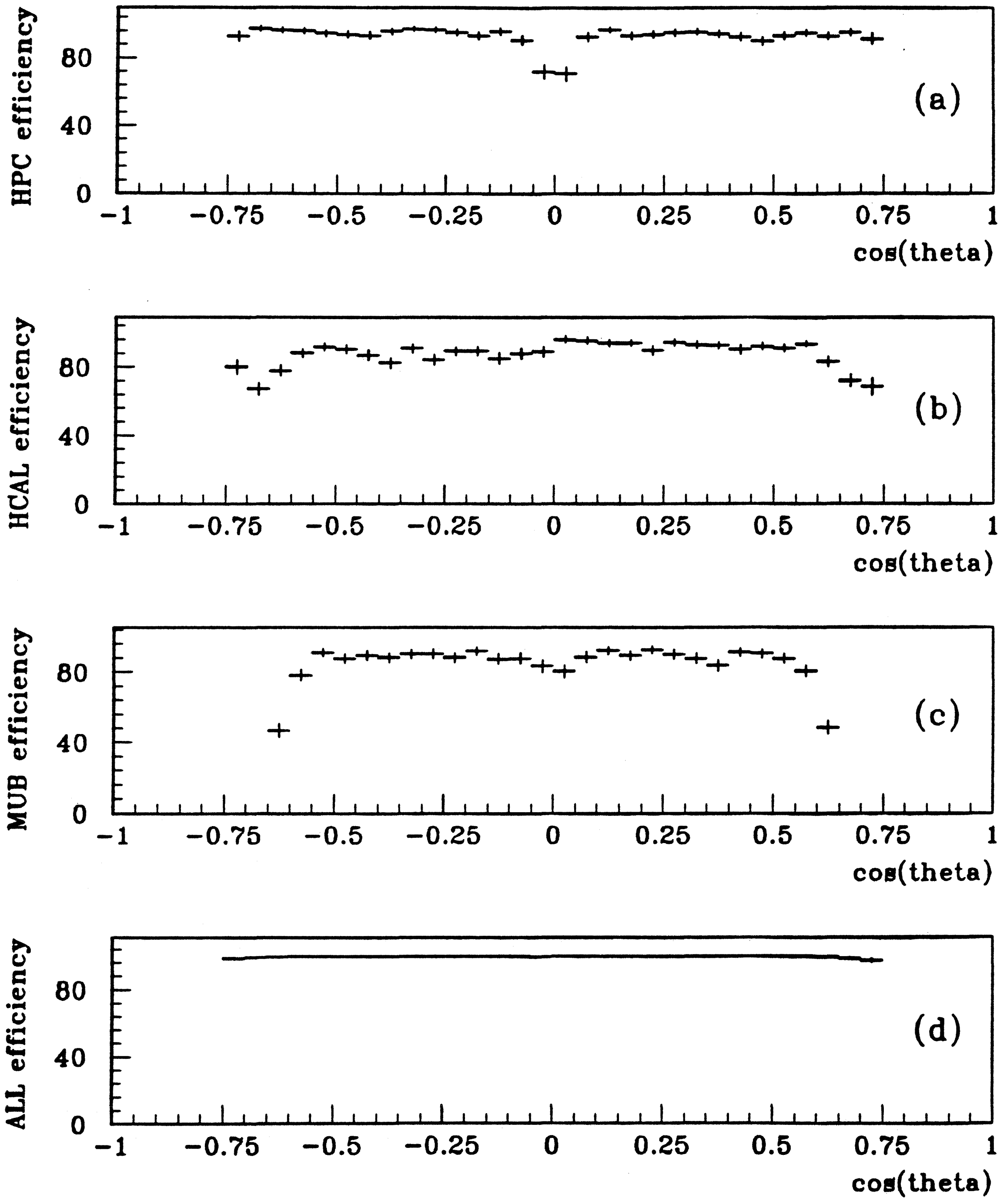

Figure 5.10: Calculated single track muon identification efficiencies as a function of $\cos\theta$ in the simulated data for (a) HPC, (b) HCAL, (c) MUB, (d) a simple 'OR' of the three detectors in each of the 40 $\cos\theta$ bins

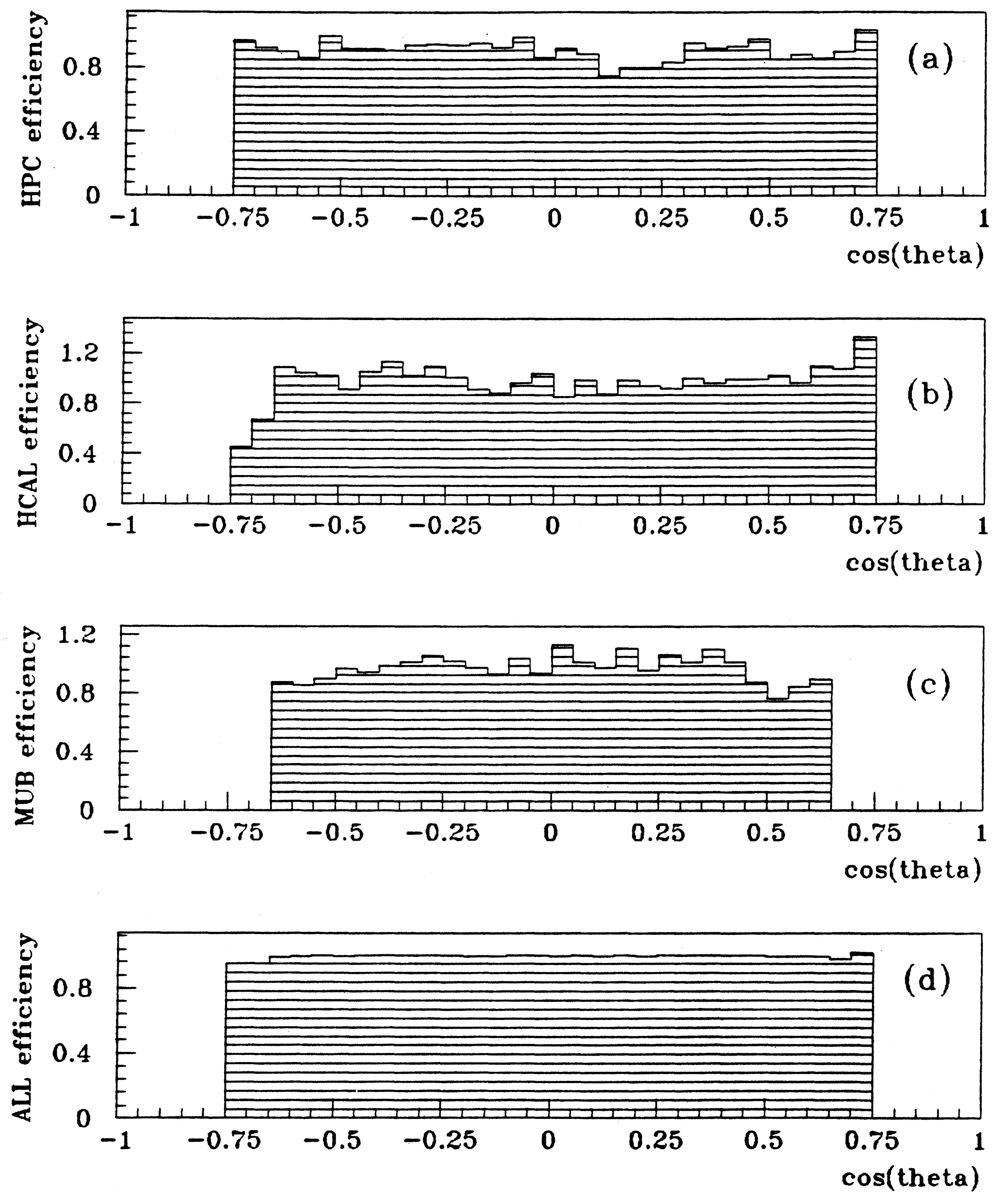

Figure 5.11: The ratio of the calculated single track muon identification efficiency in the real data (figure 5.9) to that in the simulated $\mu^+\mu^-$ sample (figure 5.10) as a function of $\cos\theta$ for (a) HPC, (b) HCAL, (c) MUB, (d) a simple 'OR' of the three detectors.

range and also near $\cos\theta = 0$. These qualities are also present in the simulated data (figure 5.10).

To obtain a 'two-track' efficiency, we find the single track efficiency ϵ_i^{OR} in bin i of $\cos\theta$ ($i = 1, ..., 40$) and take the product of the two efficiencies in back-to-back bins (i.e. we are assuming the two tracks have small acolinearity and that the probability of identification for each track is independent). In summing over bins, we weight the efficiencies by $(1+\cos^2\theta)$, the expected angular distribution of the tracks, so that the overall muon identification efficiency is given by:

$$\epsilon(total) = \frac{\sum_{i=1}^{40} \epsilon_i^{OR}\epsilon_{41-i}^{OR}(1+\cos^2\theta)_i}{\sum_{i=1}^{40}(1+\cos^2\theta)_i} \tag{5.4}$$

By this technique we obtain $\epsilon(total) = 98.1 \pm 0.1\%$ in the real data sample.

Simulated Data

We tested the effectiveness of these techniques using the simulated $\mu^+\mu^-$ events. The single track efficiencies were calculated in exactly the same way as for the real data.

The results were:

- $\epsilon_{HPC}(sing) = 92.8 \pm 0.4\%$
- $\epsilon_{HCAL}(sing) = 87.2 \pm 0.5\%$,
- $\epsilon_{MUB}(sing) = 72.8 \pm 0.7\%$,

The *calculated* single track muon identification efficiencies from the $\mu^+\mu^-$ simulation as a function of $\cos\theta$ are shown in figure 5.10. The ratio of the calculated single track efficiencies in the real data to those in the simulated $\mu^+\mu^-$ sample is shown in figure 5.11.

Since we know all the tracks are muons, we can also calculate the *actual* single track efficiencies simply by summing the number of tracks identified as a muon in each detector out of the 2257 barrel two track events (without the additonal restrictive cuts). We find:

- *actually* $\epsilon_{HPC}(sing) = 91.4 \pm 0.4\%$

- *actually* $\epsilon_{HCAL}(sing) = 86.5 \pm 0.5\%$
- *actually* $\epsilon_{MUB}(sing) = 72.2 \pm 0.7\%$

These efficiencies are in good agreement with the *calculated* values, although generally lower.

The single track muon efficiency in the HPC for the $\mu^+\mu^-$ simulated data is some 8% better than in the real data sample. The efficiencies for the HCAL and the MUB are slightly higher in the simulation than the real data sample, but the differences are quite small.

A simple 'OR' of the three detectors' single track efficiencies ($\epsilon_k(sing)$) gives an overall single track efficiency of $\epsilon^{OR}(sing) = 99.7 \pm 0.1\%$ for both the *calculated* and *actual* efficiencies. In fact, in all the 2257 barrel two track events, 4483 *tracks* were identified as muons, giving an *actual* overall single track identification efficiency in the simulated $\mu^+\mu^-$ sample of $\epsilon_{act}(sing) = 99.3 \pm 0.1\%$. This is slightly lower than the result of a simple 'OR', due to the existence of inefficient regions that are common to the three detectors.

2226 of all the 2257 barrel two track events had both muons identified, giving an actual event muon identification efficiency of $\epsilon_{act}(total) = 98.6 \pm 0.2\%$. The *calculated* overall efficiency (using equation 5.4) was $\epsilon_{sim}(total) = 99.2 \pm 0.1\%$.

Summary

The HPC muon identification efficiency appears to be significantly worse in the real data than in the simulation. However, for the MUB and HCAL there is good agreement between real data sample and the Monte Carlo. The result is that the calculated overall identification efficiency $\epsilon(total)$ is 1.1% lower in the real data.

There is some evidence from the simulation that our technique for calculating the overall muon-pair identification efficiency leads to a slight over-estimate. Assuming that this is a multiplicative factor, we multiply the *calculated* event identification efficiency in the real data by a factor of $\epsilon_{act}(total)/\epsilon_{sim}(total) = 0.994 \pm 0.002$ (obtained from our studies with the $\mu^+\mu^-$ simulation) to take into account the effect of inefficiencies which are common to the three detectors. The calculated overall muon identification efficiency for the real data becomes

- $\epsilon = 97.5 \pm 0.5\%$.

We have increased the error from the purely statistical error of 0.2% in view of the various assumptions we have had to make.

5.7.3 Track Reconstruction Efficiency

The DELPHI TPC contains regions of poor track reconstruction efficiency at the gaps between the six sectors (i.e. at every 60° in ϕ). There is also a gap between the two halves of the TPC (at $z = 0$, or $\theta = 90°$). Tracks which traverse these dead areas may still be reconstructed, either in the TPC (if they are sufficiently curved) with fewer reconstructed points, or using other detector(s) (most commonly, the ID and OD). Figure 5.12(a) shows the phi distribution for all barrel two track events, folded over six times (i.e. the horizontal axis is ϕ(degrees) modulo 60°). The inefficiency at $\phi = 30°, 90°, ..., 330°$ is clearly visible. A similar distribution is seen in the simulated $\mu^+\mu^-$ data (figure 5.12(b)). By dividing these two plots into 5 sections, and calculating the number of tracks apparently missing in the central section, we estimate track losses of $5.7 \pm 0.5\%$ (in the real data) and $5.3 \pm 0.5\%$ (in the simulated $\mu^+\mu^-$) due to the ϕ holes (statistical errors only).

For the polar angle, we expect a $(1 + \cos^2\theta)$ distribution in a plot of all charged tracks in barrel two track events (figure 5.12(c) and (d)). A region of low track reconstruction efficiency around $\cos\theta = 0$ is clearly visible. The loss is estimated at $1.3 \pm 0.2\%$ in the real data and $0.7 \pm 0.3\%$ in the simulated $\mu^+\mu^-$ sample.

Allowing for both θ and ϕ losses, the overall track reconstruction efficiency becomes $93.1 \pm 1.0\%$, where an additional error of 0.5% has been added to take account of possible systematic inaccuracy in the measurement of track parameters and correlations.

5.7.4 Acolinearity and Momentum Cuts, and Acceptance

The number of events which we fail to select because of the acolinearity and momentum cuts were estimated using the DYMU3 generator [13]. We generated

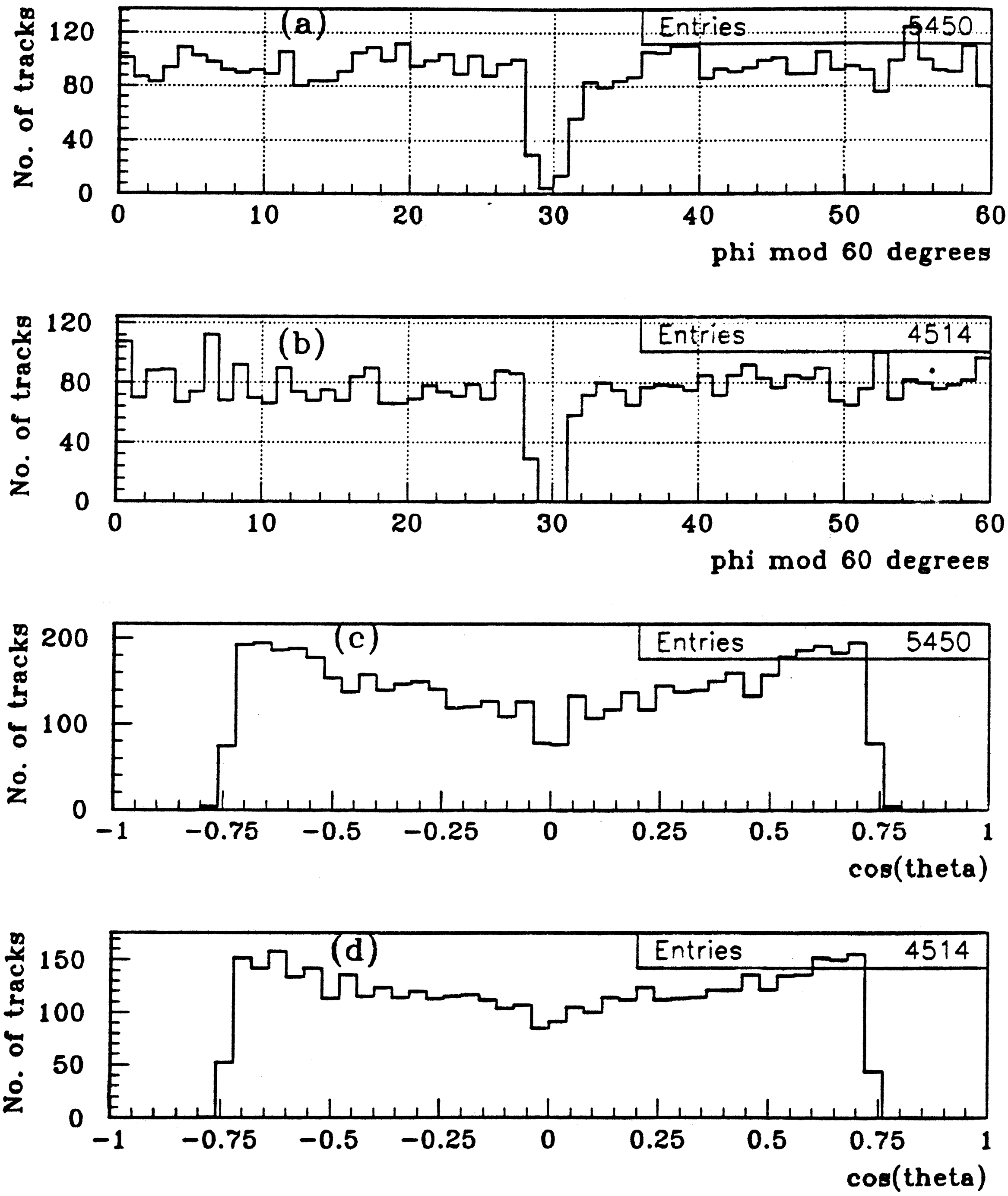

Figure 5.12: (a),(b) Distribution in ϕ(degrees) modulo 60° for all barrel two track events in real data and simulated $\mu^+\mu^-$ samples respectively. (c),(d) Distribution in θ for all barrel two track events in real data and simulated $\mu^+\mu^-$ samples respectively.

four-vectors for at least 5000 events over the full angular range at seven centre-of-mass energies and 'smeared' the momentum to mimic a momentum resolution of $\delta p/p = 10\%$. We then applied identical cuts to those applied to the real data to select barrel two track events.

The number of events passing successive cuts is shown in table 5.2. Correction Factor 1 is that factor which has to be applied to the number of detected events to get the number of events in the extended barrel region before the momentum and acolinearity cuts. Correction Factor 2 scales the number of detected events up to the number expected in the full angular range (4π steradians).

We see that due to the momentum and acolinearity cuts alone we fail to select about 3% of our muon-pairs. A greater fraction of events are lost at points where the overall cross-section is lower (away from the peak)[14].

CMS Energy	Events Generated	After Barrel Cut	After Mom. Cut	After Acol. Cut	Correction Factor 1	Correction Factor 2
88.28	5000	3163	3100	3009	1.051 ± 0.004	1.662 ± 0.019
89.28	5000	3178	3123	3042	1.045 ± 0.004	1.644 ± 0.019
90.28	5000	3215	3175	3121	1.030 ± 0.003	1.602 ± 0.018
91.28	10000	6520	6426	6306	1.034 ± 0.002	1.586 ± 0.012
92.28	5000	3199	3151	3091	1.035 ± 0.003	1.618 ± 0.018
93.28	5000	3218	3164	3088	1.042 ± 0.004	1.619 ± 0.018
94.28	5000	3197	3156	3054	1.047 ± 0.004	1.637 ± 0.018

Table 5.2: Topological Correction Factors computed with DYMU3

At $E_{CMS} = 91.28$, 6520 events pass the barrel cut, which implies an acceptance of 65.2±0.5%. This is close to the geometrical coverage of the extended barrel region, which for a single track assuming a $(1 + \cos^2\theta)$ distribution, is given

[14] To calculate these correction factors due to these cuts we are of course reliant on the accuracy of the event generator, DYMU3. The generator relies on the theory of electroweak radiative corrections — the theory we are trying to test. However, the largest corrections come from photon radiation (mainly in the initial state) which is pure QED and well understood. Nevertheless, it is desirable to relax the acolinearity and momentum cuts as far as is practicable, without introducing the possibility of large errors due to unpredictable backgrounds

by:

$$\frac{3}{8}\int_{43^\circ}^{137^\circ}\left(1+\cos^2\theta\right)\mathrm{d}\cos\theta = 0.646 \tag{5.5}$$

The errors in table 5.2 are purely statistical. Systematic errors, due to the inaccuracy of the generator or of the measurement of track characteristics, are hard to estimate, but in the case of Correction Factor 2, which we will use later for our cross-section estimates, are small compared to the statistical error.

5.8 Backgrounds

5.8.1 Tau Background

From 7499 Koralz $\tau^+\tau^-$ events, 131 passed all the cuts of section 5.4 (= $1.7 \pm 0.2\%$). We normalise by the number of DYMU3 $\mu^+\mu^-$ events which pass all these cuts and obtain a tau background in the muon-pair sample, estimated from Monte Carlo studies alone, of $3.1 \pm 0.3\%$ (statistical error only).

We may also obtain an estimate of this background from the real data by comparing the acolinearity distribution of the muon-pair candidates with that predicted by the Monte Carlos. Instead of using the absolute numbers of events of each type which were identified as muons, in this method we use the *ratios* of numbers of events of different acolinearities in the same Monte Carlo. The results are expected to be independent of muon identification efficiencies.

We consider only those events which pass all muon-pair selection criteria and divide them into two samples:

- Class 1: events with $0° \leq acol \leq \psi°$
- Class 2: events with $\psi° \leq acol \leq 10°$

For the *real* data final muon-pair event sample, we define:

- N_1, N_2 = number of events in class 1 and 2
- $N_i(\tau\tau)$ and $N_i(\mu\mu)$ = number of events in class i which are actually $\tau^+\tau^-$ pairs and $\mu^+\mu^-$ pairs respectively
- the fraction, $f = \frac{N_2}{N_1+N_2}$, of muon-pair candidate events which are of class 2

From the DYMU3 and KORALZ simulations, we define:

- f^τ, f^μ = the fraction of muon-pair candidate events of class 2 in the $\tau^+\tau^-$and $\mu^+\mu^-$simulations respectively

Now we may write down:

$$N_2(\tau\tau) + N_2(\mu\mu) = N_2 \quad (5.6)$$

$$f^\tau\left(N_1(\tau\tau) + N_2(\tau\tau)\right) + f^\mu\left(N_1(\mu\mu) + N_2(\mu\mu)\right) \approx f\left(N_1 + N_2\right) \quad (5.7)$$

where the equality holds in the case that the Monte Carlos exactly model the measured acolinearity distributions. Dividing through by $(N_1 + N_2)$, which is the number of events in our final muon-pair sample, we have:

$$f^{\tau}n^{\tau} + f^{\mu}n^{\mu} = f \tag{5.8}$$

where

$$n^{\tau} = \frac{N_1(\tau\tau) + N_2(\tau\tau)}{N_1 + N_2} \tag{5.9}$$

is the proportion of our sample which is actually tau pairs (and n^{μ} is similarly defined). With the obvious condition that $n^{\mu} + n^{\tau} = 1$, we find from equation 5.8:

$$n^{\tau} = \frac{f - f^{\mu}}{f^{\tau} - f^{\mu}} \tag{5.10}$$

For example, with $\psi = 1.0°$, $f = 0.145 \pm 0.009$, $f^{\mu} = 0.111 \pm 0.007$, $f^{\tau} = 0.863 \pm 0.030$, which gives a tau background of $n^{\tau} = 4.5 \pm 1.6\%$ where the error is limited by the statistics in the real event sample. This is consistent with the value quoted at the beginning of this section, but the error is about five times bigger.

In conclusion, we use the value of 3.1% obtained from the simulations alone, and we extend the error slightly to 0.5% as we know the particle identification in the simulation is not perfectly tuned.

5.8.2 Electron Background

There is a possibility of a small e^+e^- background in the muon-pair sample. To study this contamination, we considered barrel two track events and applied the following additional cuts:

- a tighter momentum cut: exactly two charged tracks with momentum $p \geq 25$ GeV
- a tighter acolinearity cut: *acol* $\leq 1°$

1956 events passed these cuts. Firstly, we looked at that subset of events for which both tracks had an electron-like signal in the barrel electromagnetic calorimeter: i.e. each track had $E_{25}(HPC) \geq 25$ GeV. Of the 670 events which satisfied all these criteria, none had both tracks identified as muons[15].

We then investigated misidentification of the electron as a muon in the HPC itself. One track was used to 'tag' a probable e^+e^- event, and we studied the second track to see if it was identified as a muon. We required $E_{25}(HPC) \geq 35$ GeV for the first track. Of 1239 instances, 13 had the second track identified as a muon (11 times in the HPC only). This corresponds to a maximum single track misidentification rate of $1.0 \pm 0.3\%$ if all these tracks are really electrons.

When a track is misidentified in the HPC, it is likely that it has hit a large area of dead-space. Since dead-space is mostly back-to-back correlated, we resort to Monte Carlo techniques again. In our 803 e^+e^- simulated events (all generated in the barrel), there were 647 barrel two track events. 17 tracks were seen as muons in the HPC (i.e. with $0 \leq E_{25}(HPC) \leq 2$ GeV). No tracks were identified as muons in the MUB or HCAL. 3 of the barrel two track events had both tracks identified as muons in the HPC, and so passed all the muon-pair selection criteria of section 5.4. It is interesting that all the tracks in these three events had polar angles $89.0° < \theta < 91.0°$.

The e^+e^- background is thus approximately $0.4 \pm 0.2\%$ (scaling the 803 events to the full solid angle by 1.6). It arises because there are inefficient areas in the HPC around the plane of $z = 0$, and an electron entering this region may leave a total energy deposit which is compatible with a minimum ionising particle.

The e^+e^- background will be neglected for the purpose of this analysis.

5.8.3 Cosmic Background

Cosmic muons reach the pit at an almost constant rate, whilst the rate of production of muon-pairs clearly depends on the run conditions (beam luminosity and cross-section at that centre-of-mass energy). In general, we expect the cosmic background in our muon-pair sample to be greater for centre-of-mass energies away from the peak. Outside the interaction region but well within the region for which the trigger and track reconstruction is efficient, we expect the plane of

[15]One event had one space point in the MUB associated to one track.

perigee against z_0 to be uniformly populated by cosmic muons (see figure 5.3). We considered events which passed all the muon-pair selection criteria of section 5.4 except the vertex cut. Two regions were defined:

- Region A: $r_0 \leq 0.8$ cm, $|z + 0.5| \leq 4.0$ cm (The Interaction Region);
- Region B: $r_0 \leq 5.0$ cm, $|z + 0.5| \leq 5.0$ cm, but excluding Region A.

We determined the integrated track flux density in Region B and, assuming these were all cosmic muon tracks and that the cosmic flux density was the same inside the interaction region, we obtained the estimates of cosmic muon background given in table 5.3. For the correction factor in table 5.3 (the factor by which the number of candidate muon-pair events must be multiplied) we have added an additional error of 0.5% in quadrature to represent systematic errors.

CMS Energy	Cosmic Background	Correction Factor
88.28	10.5 $\pm$ 1.0 %	0.895 $\pm$ 0.011
89.28	3.0 $\pm$ 0.4	0.970 $\pm$ 0.006
90.28	2.6 $\pm$ 0.2	0.974 $\pm$ 0.005
91.28	1.2 $\pm$ 0.1	0.988 $\pm$ 0.005
92.28	3.3 $\pm$ 0.3	0.967 $\pm$ 0.006
93.28	3.6 $\pm$ 0.5	0.964 $\pm$ 0.007
94.28	6.3 $\pm$ 0.5	0.937 $\pm$ 0.007
ALL	1.9 $\pm$ 0.1	0.981 $\pm$ 0.005

Table 5.3: Estimated Cosmic Background at different Centre-of-Mass Energies

5.8.4 Other Backgrounds

All other backgrounds, either 'physical' (two-photon events) or 'machine' (beam-gas,beam-wall events etc.) are expected to be negligible given the selection criteria employed.

5.9 Summary

The number of muon-pairs detected at seven different centre-of-mass energies is given in the second column of table 5.4. These numbers are then scaled by the following correction factors, estimated as above:

- 1.008 ± 0.001 for trigger efficiency (for runs after 10628);
- 1.026 ± 0.005 for muon identification efficiency;
- 1.074 ± 0.012 for track reconstruction efficiency;
- 1.586 ± 0.012 for **'acceptance cuts'**; that is, acolinearity and momentum cuts, and barrel acceptance (for $E_{CMS} = 91.28$). See also table 5.2;
- 0.969 ± 0.005 for tau pair background;
- 0.988 ± 0.005 for cosmic background (for $E_{CMS} = 91.28$). See also table 5.3.

Note that for runs before 10628 and/or at other beam energies, the appropriate correction factors have been used.

Column 4 of table 5.4 has the number of muon-pairs detected at each beam energy after all the correction factors have been applied. In column 3 we give the numbers of muon-pairs before any correction has been made for the momentum and acolinearity cuts and the barrel acceptance (the 'acceptance cuts'). The systematic errors are not only energy dependent but also time dependent (because of the trigger efficiences — see table 5.1). The mean systematic error at the peak point (weighted by the number of events) is 1.9% on the numbers in column 4, and 1.7% on those in column 3.

In the next chapter, we extract some electroweak observables using this muon-pair event sample.

$\sqrt{s}$	$\mu^+\mu^-$Events Detected	Corrected Number of Events (except Acceptance)	Total Corrected Number of Events over 4π
88.28	14	$14.0 \pm 3.7 \pm 0.3$	$23.2 \pm 6.2 \pm 0.6$
89.28	56	$59.5 \pm 8.0 \pm 1.0$	$97.8 \pm 13.1 \pm 2.0$
90.28	173	$183.0 \pm 13.9 \pm 3.1$	$293.2 \pm 22.3 \pm 6.0$
91.28	937	$1022.0 \pm 33.4 \pm 17.3$	$1620.9 \pm 53.0 \pm 30.7$
92.28	62	$65.4 \pm 8.3 \pm 1.1$	$105.8 \pm 13.4 \pm 2.0$
93.28	38	$40.7 \pm 6.6 \pm 0.7$	$65.9 \pm 10.7 \pm 1.3$
94.28	42	$42.9 \pm 6.6 \pm 0.7$	$70.2 \pm 10.8 \pm 1.3$

Table 5.4: Number of Muon-Pair Candidate Events at Seven Centre-of-Mass Energies

Chapter 6
Extraction of Electroweak Observables

6.1 Partial Width Ratio

The ratio of hadronic to muon-pair cross-sections is defined as:

$$R = \frac{\sigma\,(e^+e^- \to \text{hadrons})}{\sigma\,(e^+e^- \to \mu^+\mu^-)} \tag{6.1}$$

The selection procedure for hadronic events is a slight modification of that described in [22]. Hadronic events are selected by requiring at least 5 charged tracks of momentum $p > 100$ MeV in the barrel region, with a total minimum charged energy of at least 14% of the centre-of-mass energy $\sqrt{s}$.

We summed the number of hadrons detected at each beam energy for our particular selection of 'good' runs. The results are given in column 2 of table 6.1. The total number of hadronic events in these runs is 42803. An efficiency for hadronic event selection of $92.7 \pm 1.1\%$ was assumed for all energies and runs [10]. Having corrected the number of hadrons at each energy for this hadronic event selection efficiency, we obtained R by dividing by the corrected number of muons detected at this energy. The results are given in column 3 of table 6.1.

The ratio of hadronic to muon-pair partial widths is given by:

$$\Gamma_h/\Gamma_{\mu\mu} = \frac{\Gamma(Z^0 \to \text{hadrons})}{\Gamma(Z^0 \to \mu^+\mu^-)} \tag{6.2}$$

This quantity was obtained by multiplying R by correction factors to subtract the contribution to the cross-sections from diagrams where the reaction is mediated by an s-channel photon. The correction factors are dependent on the centre-of-mass energy, ranging from about 0.99 near the Z^0 pole to about 0.92 at the lower end of the energy range [51], since the s-channel photon contribution is more

$\sqrt{s}$ (GeV)	Number of hadronic evts	R	$\Gamma_h/\Gamma_{\mu\mu}$
88.22	587	$27.24 \pm 7.37 \pm 0.73$	$25.20 \pm 6.81 \pm 0.67$
89.22	1536	$16.93 \pm 2.30 \pm 0.41$	$16.25 \pm 2.21 \pm 0.39$
90.22	4755	$17.50 \pm 1.35 \pm 0.41$	$17.17 \pm 1.33 \pm 0.40$
91.22	31354	$20.87 \pm 0.69 \pm 0.47$	$20.63 \pm 0.68 \pm 0.46$
92.22	1918	$19.56 \pm 2.52 \pm 0.44$	$19.26 \pm 2.49 \pm 0.43$
93.22	1475	$24.14 \pm 3.97 \pm 0.54$	$23.52 \pm 3.86 \pm 0.53$
94.22	1178	$18.11 \pm 2.84 \pm 0.41$	$17.41 \pm 2.63 \pm 0.39$

Table 6.1: Ratio of hadronic to muon-pair cross-sections and ratio of partial decay widths. The values of $\sqrt{s}$ used are those computed taking into account the results of the LEP beam energy calibration measurements [50].

significant away from the peak[1]. The values of $\Gamma_h/\Gamma_{\mu\mu}$ obtained at the seven different centre-of-mass energies are given in column 4 of table 6.1.

The mean correction factor over these beam energies, weighted by the number of hadronic events detected at each energy, is 0.9846. Using this value, we obtain an average partial width ratio of

$$\Gamma_h/\Gamma_{\mu\mu} = 19.97 \pm 0.56(stat) \pm 0.45(sys)$$

.

[1]If the reaction $e^+e^- \rightarrow f\bar{f}$ were mediated only by the photon, the ratio R would be given to lowest order by

$$R_\gamma = 3\sum_{f}^{Nf} e_q^2$$

where e_q is the electric charge quantum number of the final state quark and the sum is over all kinematically accessible $q\bar{q}$ final states. At LEP energies

$$R_\gamma = 3\left(\left(\frac{2}{3}\right)^2 + \left(\frac{-1}{3}\right)^2 + \left(\frac{2}{3}\right)^2 + \left(\frac{-1}{3}\right)^2 + \left(\frac{-1}{3}\right)^2\right) = \left(\frac{11}{3}\right) \approx 3.7$$

We expect measured cross-section ratio to tend towards this value when the centre-of-mass energy is a long way away from the Z^0 mass (but above the threshold for $b\bar{b}$ production) and to tend towards the partial width ratio (about 20) when $\sqrt{s} = M_Z$.

6.2 Cross-sections

6.2.1 Luminosity Measurement

The luminosity is determined by measuring the cross-section for the Bhabha scattering process $e^+e^- \rightarrow e^+e^-$ at small angles, with the DELPHI Small Angle Tagger (SAT) (see Chapter 2). The Bhabha selection criteria are as described in [22]. The uncertainty on the luminosity determination has been reduced by installation of the "butterfly-wings" (an additional lead mask in front of one of the SAT arms to cover a dead zone in the vertical plane), a reduction of the error on the SAT trigger efficiency, and increased simulation statistics. The overall systematic error on the 1990 luminosity measurement is $\pm 0.8\% \pm 1.0\%$, where the second error is due to theoretical uncertainty on the computation of the Bhabha cross-section within the SAT acceptance. The integrated luminosity taken at each beam energy during our pre-defined 'good' runs (see section 5.3) is given in table 6.2[2]. The total integrated luminosity for all DAS runs used in this analysis was about 2.069 pb^{-1}.

$\sqrt{s}$ (GeV)	Number of Bhabha evts	Integrated Luminosity (nb^{-1})
88.22	3337	$126.5 \pm 2.2 \pm 1.6$
89.22	5610	$198.4 \pm 2.6 \pm 2.6$
90.22	7730	$279.1 \pm 3.2 \pm 3.6$
91.22	28464	$1089.3 \pm 6.5 \pm 14.2$
92.22	2355	$90.9 \pm 1.9 \pm 1.2$
93.22	3129	$123.2 \pm 2.2 \pm 1.6$
94.22	4008	$161.4 \pm 2.5 \pm 2.1$

Table 6.2: The integrated luminosity collected during our predefined 'good' runs. The systematic error on the integrated luminosity is taken as 1.3% which represents the theoretical error of 1.0% and the experimental error of 0.8% added in quadrature.

[2]These results are from the LUMINOSITY90 file (6-DEC-1990) maintained by the DELPHI SAT Group.

6.2.2 Results

The muon-pair cross-sections σ_μ are obtained simply by dividing the corrected number of muons detected at each centre-of-mass energy by the integrated luminosity collected at that energy, that is:

$$\sigma_\mu(\sqrt{s}) = \frac{N^{\mu}_{corr}(\sqrt{s})}{\sum_i (\int \mathcal{L}dt)_i} \tag{6.3}$$

where the sum over i is over all 'good' runs taken at $\sqrt{s}$.

The results are given in table 6.3. Two cross-sections are given at each energy. The first, σ_μ^{barr}, is a cross-section calculated before making any correction for the muon momentum and acolinearity cuts and the barrel acceptance. That is to say, the number of muons detected has been corrected for the cosmic background, the $e^+e^-\to\tau^+\tau^-$ background, trigger efficiency, muon identification efficiency and track reconstruction efficiency only. The second cross-section, σ_μ, is obtained from the number of muons detected corrected to 100% acceptance over 4π.

Note that only the statistical errors on the integrated luminosity have been included (i.e. the systematic error quoted is wholly from the muon-pair selection). All cross-sections are therefore subject to the additional error of 0.8%(expt)$\pm$1.0%(theory), which we implicitly assume is an overall normalisation error.

$\sqrt{s}$ (GeV)	Number of $\mu^+\mu^-$events	σ_μ^{barr} (nb)	σ_μ (nb)
88.22	14	$0.111 \pm 0.030 \pm 0.002$	$0.184 \pm 0.049 \pm 0.004$
89.22	56	$0.300 \pm 0.040 \pm 0.005$	$0.493 \pm 0.066 \pm 0.010$
90.22	173	$0.656 \pm 0.050 \pm 0.011$	$1.050 \pm 0.080 \pm 0.021$
91.22	937	$0.938 \pm 0.031 \pm 0.016$	$1.488 \pm 0.049 \pm 0.028$
92.22	62	$0.720 \pm 0.092 \pm 0.012$	$1.165 \pm 0.149 \pm 0.022$
93.22	38	$0.330 \pm 0.054 \pm 0.006$	$0.535 \pm 0.087 \pm 0.010$
94.22	42	$0.266 \pm 0.041 \pm 0.005$	$0.435 \pm 0.067 \pm 0.008$

Table 6.3: Number of selected events and cross-sections σ_μ for $e^+e^-\to\mu^+\mu^-$ for different centre-of-mass energies. The errors on the integrated luminosity are statistical only.

6.2.3 Fitting the Z^0 Resonance

The variation of the total cross-section with $\sqrt{s}$ around the Z^0 resonance (the 'lineshape') can be described to a good approximation by a formulation which includes a Born like term and an appropriate treatment of QED contributions. Such an ansatz is essentially independent of the Standard Model. When fitting to experimental data, using a model independent formulation is a clean way of extracting information about the Z^0 resonance.

Let us recall (from Chapter 1) the Born level (i.e. lowest order) formula for the Z^0 resonance:

$$\sigma_f^0(s) = \frac{12\pi\Gamma_{ee}\Gamma_{\mu\mu}}{M_Z^2}\frac{s}{(s-M_Z^2)^2+M_Z^2\Gamma_Z^2} \qquad (6.4)$$

$$\sigma_f^0(s=M_Z^2) = \frac{12\pi\Gamma_{ee}\Gamma_{\mu\mu}}{M_Z^2\,\Gamma_Z^2} \qquad (6.5)$$

Including higher order terms, equation 6.4 may be written as a modified Born approximation [49]:

$$\sigma_f^0(s) = \frac{12\pi\Gamma_{ee}\Gamma_{\mu\mu}}{M_Z^2}\frac{s}{(s-M_Z^2)^2+s^2\Gamma_Z^2/M_Z^2}(1+\delta(s)) \qquad (6.6)$$

The electroweak observables which we may extract by fitting the lineshape for the reaction $e^+e^-\rightarrow\mu^+\mu^-$ are the mass and the width of the Z^0 boson (M_Z and Γ_Z), and the *product* of the electron and muon partial widths, $\Gamma_{\mu\mu}\Gamma_{ee}$. Here we shall assume lepton universality, so that $\Gamma_{\mu\mu}=\Gamma_{ee}$ to a very good approximation, and we fit the leptonic partial width Γ_{ll} ($l=e,\mu$).

Predicted cross-sections at each beam energy point σ_i^{the} were obtained from the program ZFITTER [52] which uses the ZBIZON package of the Dubna-Zeuthan radiative corrections group. For the input to ZBIZON we set m_t = 130 GeV and M_H = 100 GeV. A χ^2 was formed between the measured and predicted cross-sections at each energy, defined by:

$$\chi^2_{CS} = \sum_{i=1}^{7}\frac{\left(\sigma_i^{exp}-\sigma_i^{the}\right)^2}{\left(\delta\sigma_i^{exp}\right)^2} \qquad (6.7)$$

where the sum is taken over all seven centre-of-mass energy points[3]. σ_i^{exp} is the experimental cross-section at point i and the $\delta\sigma_i^{exp}$ are the purely statistical errors

[3]The author gratefully acknowledges A.Olshevsky for supplying the necessary programs.

on this cross-section (which should be uncorrelated from point to point). χ^2_{CS} was minimised using the MIGRAD algorithm in the CERN function minimisation program MINUIT [53].

Fits of σ_μ

First we fitted to the cross-sections σ_μ (column 4 of table 6.3) obtained after correcting for all experimental cuts including those on muon polar angles, acolinearity and momenta[4]. Initially the Z^0 mass (M_Z) and width (Γ_Z) and the partial width to leptons (Γ_{ll}) were left as free parameters. The result is shown in figure 6.1(a). The minimum χ^2_{CS} values are[5]:

$$\begin{aligned} M_Z &= 91.059 \pm 0.095 \text{ GeV} \\ \Gamma_Z &= 2.504 \pm 0.178 \text{ GeV} \\ \Gamma_{ll} &= 84.5 \pm 5.2 \text{ MeV} \end{aligned}$$

The χ^2_{CS} per degree of freedom of the fit is $\chi^2_{CS}/ndf = 4.70/(7-3)$.

For the mass of the Z^0 an extra error of ± 0.020 GeV must be added due to the LEP beam energy calibration error. There is also an additional error on Γ_Z and Γ_{ll} due to the overall normalisation error. The values for the Z^0 mass and total width are in agreement with those determined in recent analyses of the hadronic lineshape [22], which are:

$$M_Z = 91.182 \pm 0.023 \text{ GeV} \tag{6.8}$$
$$\Gamma_Z = 2.462 \pm 0.021 \text{ GeV.} \tag{6.9}$$

However, as there are many fewer muon-pair events than hadronic events (see again table 6.1), the statistical errors are much larger for the fit to the $\mu^+\mu^-$ lineshape.

Given this agreement, we fixed M_Z and Γ_Z to the values given in 6.8 and 6.9. Now only Γ_{ll} was a free parameter. The minimum χ^2_{CS} fit is shown in figure 6.1(b).

[4]For the theoretically predicted cross-sections a cut was made on the invariant mass of the final state muons s' which required $s' \geq 1.0$ GeV^2, whereas physically the minimum value of s' is $4m_\mu^2$. However, when one considers that the typical value of s' is about $M_Z^2 \approx 8100$ GeV^2, one sees that the likely effect of this cut is very small.

[5]The errors are those returned from the HESSE routine of MINUIT.

The 'best' value of Γ_{ll} (with the error returned from MINUIT) is:

$$\begin{aligned} \Gamma_{ll} &= 83.76 \pm 1.18\,\text{MeV} \\ \text{with}\ \ \chi^2_{CS}/ndf &= 6.98/(7-1) \end{aligned}$$

The systematic error on the leptonic partial width due to the uncertainty on Γ_Z (± 0.021 GeV) was estimated by refitting with $\Gamma_Z = 2.483$ GeV and 2.441 GeV. The fitted leptonic partial width varied by ± 0.60 MeV. Similarly, the estimated systematic error on Γ_{ll} due to the uncertainty on M_Z(± 0.023 GeV) is ± 0.12 MeV. The weighted mean systematic error on the number of muon-pair events is 1.9% which, combined with the systematic error on the luminosity, gives an overall normalisation error of 2.3% and an error on Γ_{ll} of ± 0.97 MeV. Combining these systematic errors in quadrature, we find finally

$$\Gamma_{ll} = 83.8 \pm 1.2(stat) \pm 1.1(sys)\,\text{MeV}$$

Fits of σ_μ^{barr}

It is also possible to fit the experimental cross-sections to those predicted by ZFITTER after cuts on the muons' energies (EMIN), the minimum and maximum angle of the μ^+ (ANG1,ANG2), and the acolinearity(ACOL). Setting EMIN=15 GeV, ANG1=43°, ANG2=137°, ACOL=10° and fitting to our values of σ_μ^{barr} (column 3 of table 6.3) we obtained the curves of figure 6.1(c) and figure 6.1(d). The results of the two fits were:

1. $M_Z, \Gamma_Z, \Gamma_{ll}$ free:

$$\begin{aligned} M_Z &= 91.057 \pm 0.093\,\text{GeV} \\ \Gamma_Z &= 2.470 \pm 0.173\,\text{GeV} \\ \Gamma_{ll} &= 83.6 \pm 5.0\,\text{MeV} \\ \chi^2_{CS}/ndf &= 4.46/(7-3) \end{aligned}$$

2. $M_Z = 91.182$, $\Gamma_Z = 2.462$, Γ_{ll} free:

$$\begin{aligned} \Gamma_{ll} &= 83.8 \pm 1.2(stat) \pm 1.1(sys)\,\text{MeV} \\ \chi^2_{CS}/ndf &= 6.70/(7-1). \end{aligned}$$

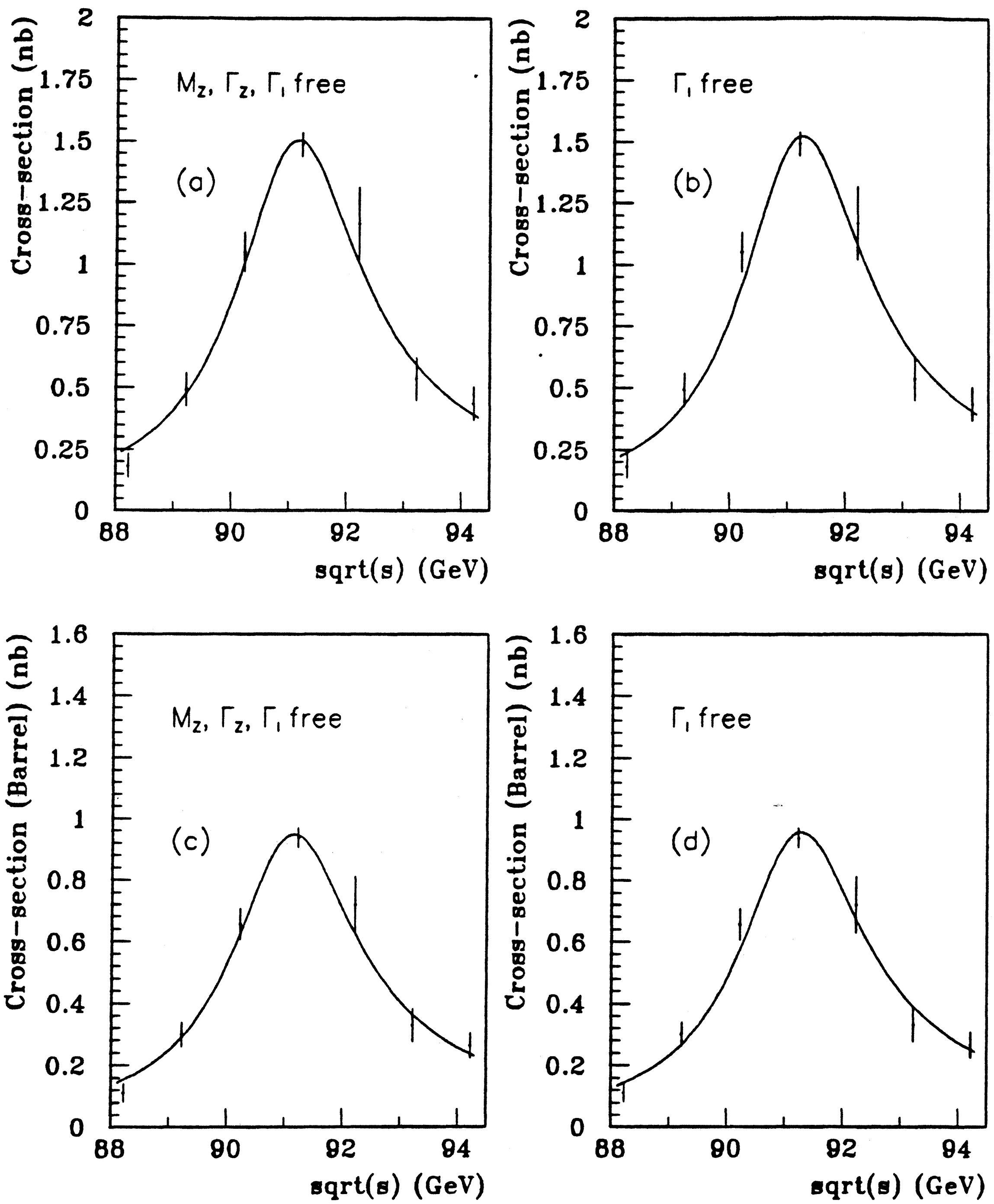

Figure 6.1: Fits of DELPHI $\mu^+\mu^-$line-shape using ZFITTER. (a) Fit of $\sigma_\mu(s)$ with M_Z,Γ_Z,and $\Gamma_{\mu\mu}$ as free parameters (after correcting for all experimental cuts). (b) Fit of $\sigma_\mu(s)$ with only $\Gamma_{\mu\mu}$ as a free parameter (after correcting for all experimental cuts). (c) Fit of $\sigma_\mu^{barr}(s)$ with M_Z,Γ_Z,and $\Gamma_{\mu\mu}$ as free parameters (with cuts on the muons' energies, angles and acolinearity). (d) Fit of $\sigma_\mu^{barr}(s)$ with only $\Gamma_{\mu\mu}$ as a free parameter (with cuts on the muons' energies, angles and acolinearity).

The systematic error on Γ_{ll} includes contributions from the uncertainty on M_Z,Γ_Z, the luminosity and the number of muon-pairs, estimated exactly as above. The results are consistent with those determined by the fits to σ_μ.

6.3 Forward-Backward Asymmetries

As described in Chapter 1, the differential cross-section for $e^+e^- \rightarrow f\bar{f}$ has the form:

$$\frac{d\sigma_f}{d\Omega} = \frac{\alpha^2}{4s}\left[A_1(s)(1+\cos^2\theta) + A_2(s)\cos\theta\right] \tag{6.10}$$

and the term in $\cos\theta$ leads to an asymmetry in the rate of production of fermions between the forward and backward hemispheres.

Clearly, it is necessary to know which track in a candidate $\mu^+\mu^-$event was a μ^- and which was a μ^+. In 11 of the 1322 candidate events, both tracks had the same charge (in 7 cases, both tracks were assigned a negative charge, in 4 cases both were positive). This is clearly unphysical as electric charge must be conserved in the Z^0 decay. The lower momentum (more highly-curved) track is more likely to have its charge correctly measured. This was confirmed by scanning the 'problem' events using the event display program DELGRA [57]. Wrong charge assignment was generally found to be due to software 'errors', e.g. incorrect association of hits in the Outer Detector with the track in the TPC. In this study, we use the lower momentum track to define the track charge assignments.

8 of the 1322 candidate events had one track just outside the extended barrel region. These events were discarded.

6.3.1 Results

Direct Measurements

The most direct measurement of the forward-backward asymmetry may be made using the relation:

$$A_{FB}^{dir} = \frac{N_F - N_B}{N_F + N_B} \tag{6.11}$$

where

- N_F = number of μ^- tracks with $\theta < 90°$
- N_B = number of μ^- tracks with $\theta > 90°$

Here, θ is the polar angle between the μ^- track and the e^- beam at the vertex. The results are given in column 4 of table 6.4. The errors quoted are statistical, given by:

$$\delta A_{FB}^{dir}(s) = \sqrt{\frac{4\,N_B(s)\;N_F(s)}{(N_B(s)+N_F(s))^3}} \tag{6.12}$$

$$= \sqrt{\frac{\left(1 - A_{FB}^{dir}(s)^2\right)}{N_T(s)}} \tag{6.13}$$

where $N_T(s)$ is the total number of events seen at centre-of-mass energy $\sqrt{s}$.

However, these asymmetries have not been corrected for effects due to the extended barrel cut (which demands that we only detect muons in the region $43° \leq \theta \leq 137°$), and due to detector inefficiencies within this angular region. For example, if the overall acceptances in the forward and backward hemispheres are given by ϵ_F and ϵ_B, then the asymmetry is given by:

$$A_{FB} = \frac{\frac{N_F}{\epsilon_F} - \frac{N_B}{\epsilon_B}}{\frac{N_F}{\epsilon_F} + \frac{N_B}{\epsilon_B}} \tag{6.14}$$

The acceptances drop out if $\epsilon_F = \epsilon_B$, but we cannot expect this equality to hold in general because of the $\cos\theta$ term in equation 6.10.

If we assume 100% efficiency for regions within some cut cth such that $-cth \leq \cos\theta \leq cth$, and we assume zero efficiency elsewhere, the corrected asymmetry A_{FB} may be obtained from the directly measured asymmetry by a factor which is a constant for all values of $A_2(s)/A_1(s)$:

$$A_{FB} = \frac{3 + cth^2}{4\,cth}\,A_{FB}^{dir}. \tag{6.15}$$

With $cth = \cos 43°$ (since we restricted our events to the 'extended barrel region' in Chapter 5) this becomes $A_{FB} \approx 1.21\,A_{FB}^{dir}$. Calculating the corrected asymmetries A_{FB} in this way, we obtained the results in column 5 of table 6.4.

Fitting the Angular Distribution

To check for systematic effects a fit was made of the angular distribution of the muons to the expected distribution (equation 6.10). A *log-likelihood* method was used in view of the small statistics[6]. From equation 6.10, we can say that the

[6]The author gratefully acknowledges L.Lyons for supplying the necessary programs.

$\sqrt{s}$ (GeV)	N_F	N_B	A_{FB}^{dir}	A_{FB} (4π)	A_{FB}^{LL}
88.22	3	11	-0.571 ± 0.219	-0.690 ± 0.265	-0.724 ± 0.272
89.22	21	35	-0.250 ± 0.129	-0.302 ± 0.156	-0.371 ± 0.150
90.22	80	92	-0.070 ± 0.076	-0.084 ± 0.092	-0.053 ± 0.080
91.22	488	442	$+0.049 \pm 0.033$	$+0.060 \pm 0.040$	$+0.055 \pm 0.037$
92.22	25	37	-0.194 ± 0.125	-0.234 ± 0.151	-0.246 ± 0.122
93.22	24	14	$+0.263 \pm 0.157$	$+0.318 \pm 0.189$	$+0.358 \pm 0.169$
94.22	26	16	$+0.238 \pm 0.150$	$+0.288 \pm 0.181$	$+0.334 \pm 0.154$

Table 6.4: Forward-Backward Asymmetries at Seven Centre-of-Mass Energies

probability density for observing an event i for which the cosine of the muon is $(\cos\theta)_i = z_i$, is given by:

$$y_i(R) = N(1 + z_i^2 + R(s)\ z_i) \tag{6.16}$$

where

$$R(s) \quad = \quad \frac{A_2(s)}{A_1(s)}. \tag{6.17}$$

N is a normalisation factor which turns out to be a constant (i.e. independent of R) and so may be dropped:

$$\int_{-1}^{1} N\left(1 + z^2 + Rz\right)\mathrm{d}z = 1 \ \Rightarrow\ N = 3/8 \tag{6.18}$$

The likelihood $\mathcal{L}$ is defined as the product of the y_i for all n events collected at $\sqrt{s}$ in the final sample:

$$\mathcal{L}(R) = \prod_i^n \left(1 + z_i^2 + R(s)\ z_i\right) \tag{6.19}$$

$\mathcal{L}(R)$ is the joint probability density for obtaining the observed set of $\cos\theta_i$ for any specific value of R. The best value of R was estimated by maximising the log-likelihood LL as a function of R, where:

$$LL = \log\mathcal{L} = \sum_i^n \log\left(1 + z_i^2 + R(s)\ z_i\right) \tag{6.20}$$

The asymmetries obtained, $A_{FB}^{LL} = \frac{3R}{8}$ are given in column 6 of table 6.4. The given error on A_{FB}^{LL} is from the change in R required to reduce LL from its maximum value by 0.5[7]. The results are consistent with the direct measurements but the errors are smaller.

Systematic Errors

We recalculated the asymmetry for six values of $\theta_{cut} = \cos^{-1} cth$ from 43° to 53°. The mean values on the peak were $A_{FB}^{LL} = 0.059$ and $A_{FB} = 0.064$ with standard deviations of 0.006 and 0.005 respectively. There was no significant systematic trend.

If the 11 'like-sign' events are discarded (rather than switching the sign of the higher momentum track), the peak asymmetries become $A_{FB}^{LL} = 0.058 \pm 0.037$ and $A_{FB} = 0.064 \pm 0.040$.

The magnitude of the systematic errors seems to be well below that of the statistical errors for this data sample. We estimate a systematic error of 0.005. Hence, for the point nearest to the Z^0 resonance peak, the asymmetry is given by:

$$A_{FB} = 0.060 \pm 0.040(stat) \pm 0.005(sys)\ , \text{ for } \sqrt{s} = 91.22 \text{ GeV}$$

6.3.2 Fitting the Asymmetry across the Resonance

A fit was made to the muon forward-backward asymmetries at seven centre-of-mass energies spanning the Z^0 resonance. The predicted asymmetry A_{FBi}^{the} at energy point i was obtained from ZFITTER. A χ^2 was formed between the measured and predicted asymmetries, defined by:

$$\chi_{AS}^2 = \sum_{i=1}^{7} \frac{\left(A_{FBi} - A_{FBi}^{the}\right)^2}{\left(\delta A_{FBi}\right)^2} \tag{6.21}$$

where the sum is taken over all centre-of-mass energy points and δA_{FBi} is the statistical error on the directly measured asymmetry for energy point i.

[7]This assumes that the likelihood function $\mathcal{L}(R)$ is a Gaussian, that is:

$$\mathcal{L} = \exp\left(\frac{-(R-R_0)^2}{2\sigma^2}\right)$$

where R_0 is the value of R when the log-likelihood is a maximum. $\mathcal{L}$ should tend to a Gaussian when the number of observations (events) n is large (for a proof see for example [58]).

From the formulae of Chapter 1 we have for the muon-pair lowest order forward-backward asymmetry on the peak:

$$A^0_{FB}(s = M_Z^2) = \frac{3}{4}\frac{v_\mu a_\mu}{(v_\mu^2 + a_\mu^2)}\frac{v_e a_e}{(v_e^2 + a_e^2)} \tag{6.22}$$

Again, this formula is almost model independent. Assuming lepton universality, $v_e = v_\mu = v_l$ and $a_e = a_\mu = a_l$, and this becomes:

$$A^0_{FB}(s = M_Z^2) = \frac{3}{4}\frac{v_l^2 a_l^2}{(v_l^2 + a_l^2)^2} \tag{6.23}$$

In the Standard Model $v_l = -1 + 4\sin^2\theta_W$ and $a_l = -1$ to lowest order. Away from the Z^0 pole, $\Re(\chi)$ is non-zero and the asymmetry is mainly dependent on the product $a_e a_\mu \Re(\chi)$. Radiative corrections modify the vector and axial vector coupling constants whilst essentially preserving the tree level relations for the asymmetry (and the partial width).

χ^2_{AS} was minimised using MINUIT with v_l^2 and a_l^2 as free parameters. We fixed $M_Z = 91.182$ GeV and $\Gamma_Z = 2.462$ GeV. The results were:

$$\begin{aligned} v_l^2 &= 0.0119 \pm 0.0073(stat) \pm 0.0007(sys) \\ a_l^2 &= 0.590 \pm 0.210(stat) \pm 0.0022(sys) \\ \chi^2_{AS}/ndf &= 8.65/(7-2) \end{aligned}$$

where the systematic errors represent the effect of the uncertainties on M_Z and Γ_Z. The directly measured asymmetries A_{FB} and the results from the fit are shown in figure 6.2.

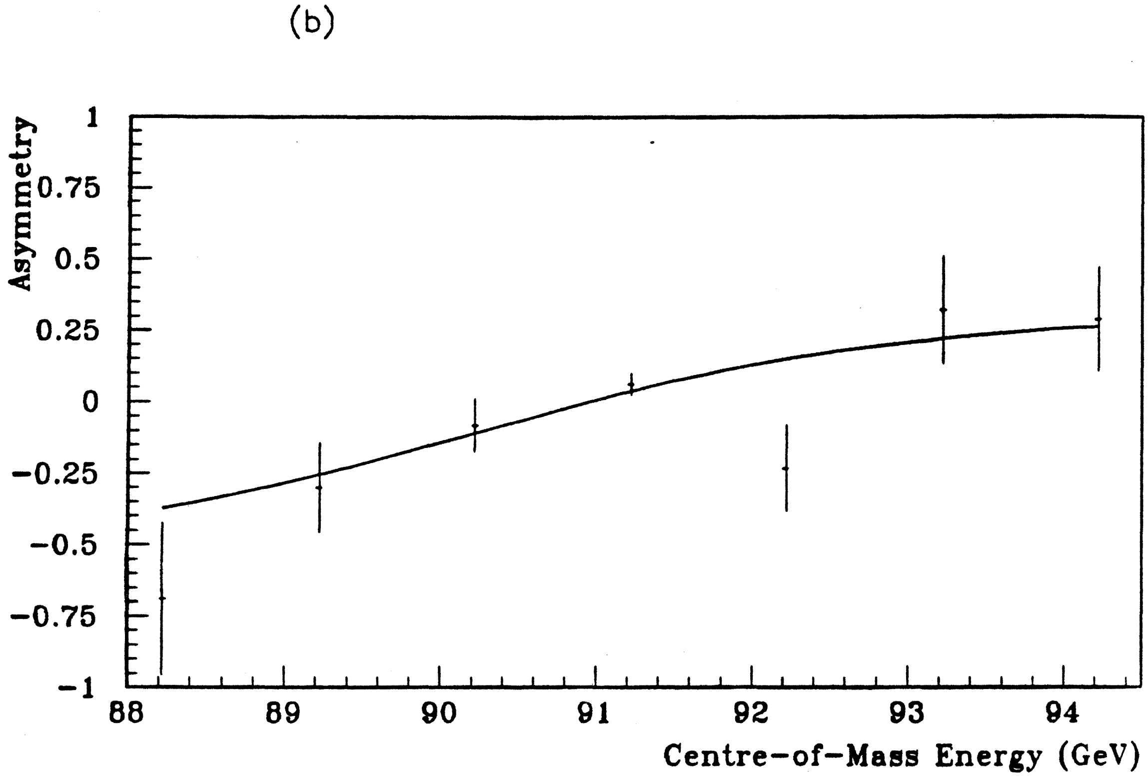

Figure 6.2: A Fit of $\mu^+\mu^-$ Forward-Backward Asymm[illegible] using ZFITTER, with v_l and a_l as Free Param[illegible]

6.4 Simultaneous fit of Line Shape and Asymmetries

A simultaneous fit was made to the both $\sigma_\mu(s)$ and $A^\mu_{FB}(s)$ across the Z^0 resonance, using the leptonic vector and axial vector coupling constants as free parameters. As in section 6.3.2, we assumed $v_l = v_e = v_\mu, a_l = a_e = a_\mu$. The leptonic decay width to lowest order is (from equation 1.42):

$$\Gamma_{ll} = \frac{G_F M_Z^3}{24\pi\sqrt{2}} \left(v_l^2 + a_l^2\right) \tag{6.24}$$

Thus, a_l^2 is essentially proportional to Γ_l (since $a_l^2 \gg v_l^2$), and v_l^2 is mainly determined from the peak asymmetry, to which it is related linearly. Therefore, the errors on a_l^2 and v_l^2 are very nearly Gaussian.

We minimised a 'total' χ^2 defined by:

$$\chi^2_{tot} = \chi^2_{CS} + \chi^2_{AS} \tag{6.25}$$

The measured points and the curve resulting from the simultaneous fit are shown in figure 6.3. The result of the fit is:

$$\begin{aligned} v_l^2 &= 0.0134 \pm 0.0116 \\ a_l^2 &= 0.996 \pm 0.0195 \end{aligned} \tag{6.26}$$

with $\chi^2_{AS} = 10.3$, $\chi^2_{CS} = 6.6$, $\chi^2_{tot}/ndf = 16.9/(14-2)$.

The systematic error on these values has contributions from the uncertainty on $M_Z(\pm 0.023$ GeV) and $\Gamma_Z(\pm 0.021$ GeV), and the overall normalisation error (2.3%). The errors were estimated by refitting with values for M_Z, Γ_Z and σ_μ which differed from their central values by one standard deviation. The results were:

$$\begin{aligned} \delta v_l^2 &= \pm 0.0006(M_Z) \pm 0.00008(\Gamma_Z) \pm 0.00005(\sigma_\mu) \\ \delta a_l^2 &= +0.0001(M_Z) \pm 0.0069\,(\Gamma_Z) \pm 0.012(\sigma_\mu) \end{aligned} \tag{6.27}$$

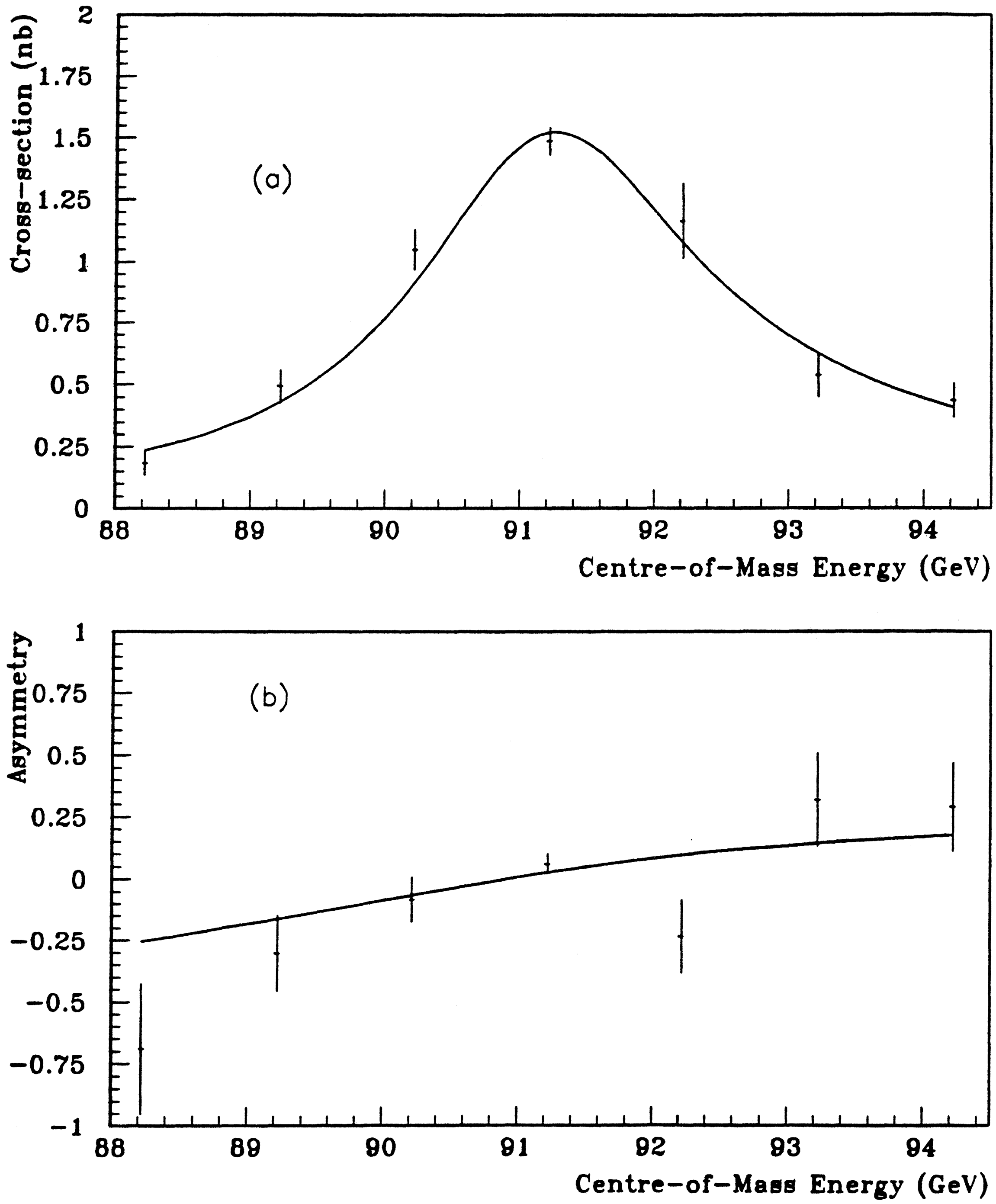

Figure 6.3: A Simultaneous Fit of DELPHI $\mu^+\mu^-$Cross-Sections and Forward-Backward Asymmetries using ZFITTER, with v_l and a_l as Free Parameters.

Adding these systematic errors in quadrature, we have:

$$\begin{aligned} v_l^2 &= 0.0134 \pm 0.0116(stat) \pm 0.0006(sys) \\ a_l^2 &= 0.996 \pm 0.019(stat) \pm 0.014(sys) \end{aligned} \tag{6.28}$$

Taking the sign of both v_l and a_l to be negative, as suggested by neutrino-electron scattering experiments [54], we find finally:

$$\begin{aligned} v_l &= -0.116^{+0.074}_{-0.042}(stat) \pm 0.003(sys) \\ a_l &= -0.998 \pm 0.010(stat) \pm 0.007(sys) \end{aligned} \tag{6.29}$$

In fact, the errors on v_l and a_l are not uncorrelated. Figure 6.4 shows one and two standard deviation contours (generated by MINUIT) for a direct fit of v_l and a_l. Also shown are the Standard Model predicted values of these coupling constants for a range of top quark massses as shown and for Higgs masses in the range 40 to 1000 GeV.

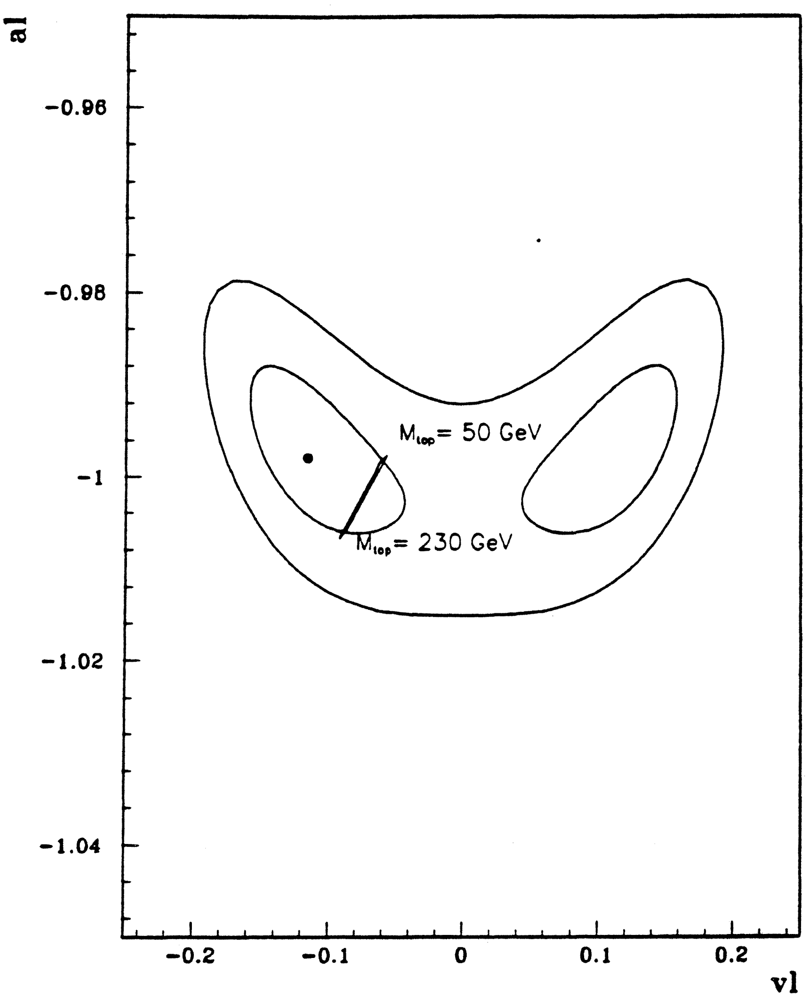

Figure 6.4: One and two standard deviation contours for the fit to v_l and a_l, with the Standard Model predictions for a range of top quark masses (as shown) and Higgs masses in the range 40 to 1000 GeV.

6.5 Summary and Conclusions

"I do not know what I may appear to the world, but to myself I seem to have been only like a boy playing on the sea-shore, and diverting myself in now and then finding a smoother pebble or a prettier shell than ordinary, whilst the great ocean of truth lay all undiscovered before me." Sir Isaac Newton.

The measurement of cross-sections, forward-backward asymmetries, and the partial width ratio has been presented for the reaction $e^+e^- \to \mu^+\mu^-$ close to the Z^0 peak. Data collected in the DELPHI apparatus up until July 15^{th}, 1990 were included, with the requirement that all relevant detectors were in good working order. This corresponded to an integrated luminosity of around 2.07 pb^{-1}. 1322 candidate muon-pair events were identified.

The ratio of the hadronic to muon-pair partial widths was determined from the numbers of hadronic and muon-pair events detected, and was found to be:

$$\Gamma_h/\Gamma_{\mu\mu} = \frac{\Gamma(Z^0 \to \text{hadrons})}{\Gamma(Z^0 \to \mu^+\mu^-)} = 19.97 \pm 0.56(stat) \pm 0.45(sys)$$

The measured leptonic partial decay width has been determined from a fit to the muon-pair cross-sections at seven centre-of-mass energies:

$$\Gamma_{ll} = \sqrt{\Gamma_{ee}\Gamma_{\mu\mu}} = 83.8 \pm 1.2(stat) \pm 1.1(sys) \text{ MeV}$$

The forward-backward asymmetry at $\sqrt{s} = 91.22$ GeV (the energy point nearest the peak) was:

$$A_{FB} = 0.060 \pm 0.040(stat) \pm 0.005(sys)$$

A simultaneous fit to the muon-pair cross-sections and the forward-backward asymmetries across the Z^0 resonance yielded:

$$\begin{aligned} v_l &= -0.116^{+0.074}_{-0.042}(stat) \pm 0.003(sys) \\ a_l &= -0.998 \pm 0.010(stat) \pm 0.007(sys) \end{aligned}$$

In the Standard Model, the value of the leptonic partial decay width Γ_{ll} depends on the mass of the top quark m_t. This is illustrated in figure 6.5, which shows the dependence of Γ_{ll} on m_t, as predicted by the GAMMAZ program of Burgers, Hollik and Kleiss [60]. The spread in values at each value of m_t is due to the fact that Γ_{ll} has been plotted for all combinations of the following input parameters: $M_Z = 91.159, 91.182, 91.205$ GeV, $\Gamma_Z = 2.441, 2.462, 2.483$ GeV, $M_H = 10, 100, 1000$ GeV, and the strong interaction coupling constant $\alpha_s(M_Z^2) = 0.101, 0.106, 0.111$[8]. The size of a box on this plot is proportional to the number of entries in that bin. One sees that Γ_{ll} is relatively insensitive to all but the top quark mass. Within the range $50 \leq m_t \leq 250$ GeV the leptonic partial width ranges from about 83 MeV to around 85 MeV. All these values are consistent with the measured value of Γ_{ll} in this analysis. Our value is also consistent with the average of all four LEP experiments, which has been calculated to be 83.7 ± 0.7 [56].

The ratio of partial widths Γ_h/Γ_{ll} turns out to be rather insensitive to m_t or M_H, and provides a good test of the Standard Model. The dependence on top quark mass is illustrated in figure 6.6. The ratio is plotted for all combinations of the values of M_Z, Γ_Z, M_H and α_s given above, as calculated with GAMMAZ. The three bands correspond to the three values of $\alpha_s(M_Z^2)$. One sees that the predicted values of Γ_h/Γ_{ll} are approximately in the range 20.6 to 20.8, so that all values lie roughly within one standard deviation of our measured value of $\Gamma_h/\Gamma_{\mu\mu}$ (note that the error on the measured value is about three times greater than the uncertainty on the Standard Model prediction). The average of the four LEP experiments for the *leptonic* partial width ratio is 21.08 ± 0.20 [56].

The vector and axial vector coupling constants also depend on the top quark and Higgs masses. The predicted ranges of v_l and a_l are from -0.056 to -0.096 and -0.998 to -1.008 respectively. The measured values are consistent with these predictions (see figure 6.4).

[8]This value for the strong interaction coupling constant is taken from a recent DELPHI measurement of energy-energy correlations asymmetry [59], which gave:

$$\alpha_s = 0.106 \pm 0.003(stat) \pm 0.003(sys) \pm 0.003(theory)$$

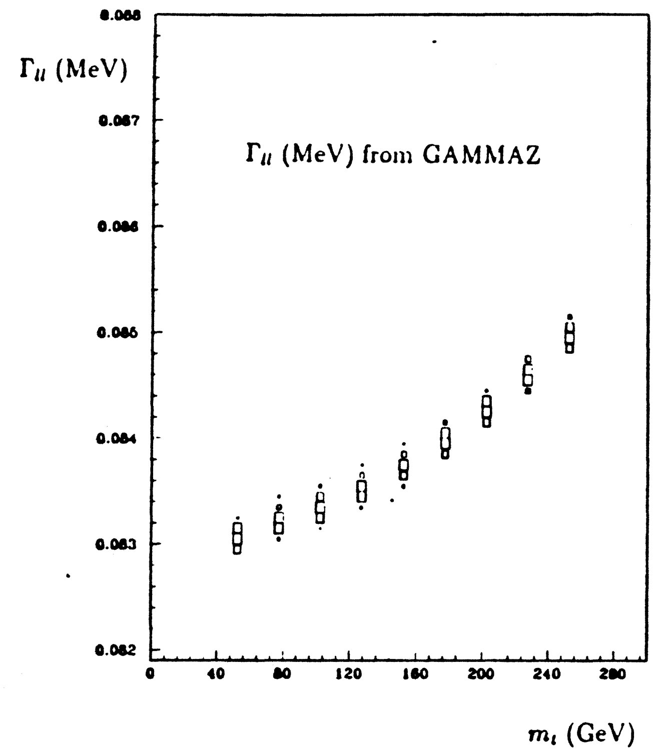

Figure 6.5: Standard Model prediction of Γ_{ll}, calculated with GAMMAZ, for all combinations of $M_Z = 91.159, 91.182$ and 91.205 GeV, $\Gamma_Z = 2.441, 2.462$ and 2.483 GeV, $M_H = 10, 100$ and 1000 GeV, and $\alpha_s(M_Z^2) = 0.101, 0.106$ and 0.111.

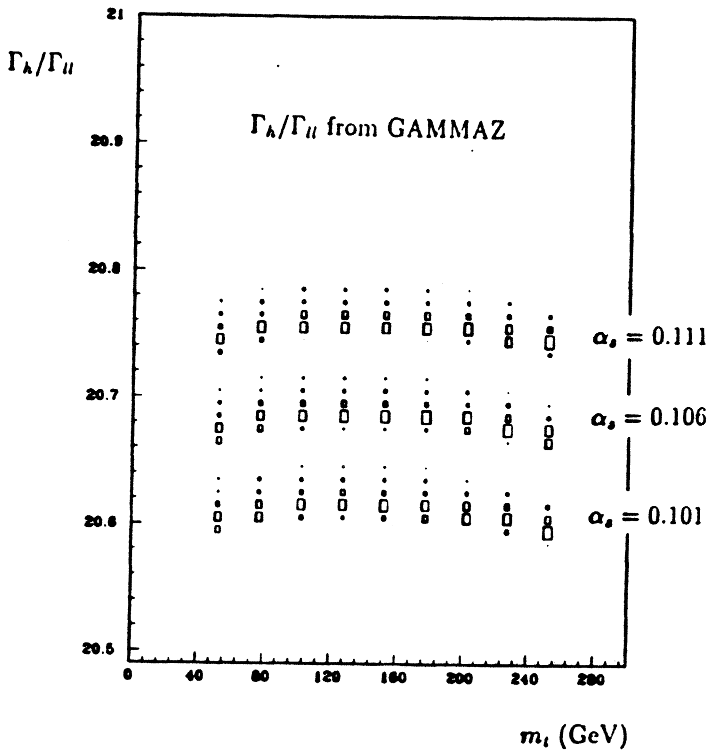

Figure 6.6: Standard Model prediction of Γ_h/Γ_{ll} calculated with GAMMAZ, for all combinations of $M_Z = 91.159, 91.182$ and 91.205 GeV, $\Gamma_Z = 2.441, 2.462$ and 2.483 GeV, $M_H = 10, 100$ and 1000 GeV, and $\alpha_s(M_Z^2) = 0.101, 0.106$ and 0.111.

In conclusion, in this analysis of the reaction $e^+e^- \to \mu^+\mu^-$ at $s \approx 8100$ GeV^2, all results are consistent with the predictions of the Standard Model.

Appendix A

Members of the DELPHI Collaboration, 1990

P. Abreu [a], W. Adam [b], F. Adami [c], T. Adye [d], G.D. Alexeev [e], J.V. Allaby [f], P. Allen [g],
S. Almehed [h], F. Alted [g], S.J. Alvsvaag [i], U. Amaldi [f], E. Anassontzis [j], W.-D. Apel [k],
B. Asman [l], P. Astier [m], C. Astor Ferreres [n], J.-E. Augustin [o], A. Augustinus [f], P. Baillon [f],
P. Bambade [o], F. Barao [a], G. Barbiellini [p], D.Y. Bardin [e], A. Baroncelli [q], O. Barring [h],
W. Bartl [b], M.J. Bates [r], M. Baubillier [m], K.-H. Becks [s], C.J. Beeston [r], P. Beilliere [t],
I. Belokopytov [u], P. Beltran [v], D. Benedic [w], J.M. Benlloch [g], M. Berggren [l], D. Bertrand [x],
S. Biagi [y], F. Bianchi [z], J.H. Bibby [r], M.S. Bilenky [e], P. Billoir [m], J. Bjarne [h], D. Bloch [w],
P.N. Bogolubov [e], D. Bollini [α], T. Bolognese [c], M. Bonapart [β], P.S.L. Booth [y], M. Boratav [m],
P. Borgeaud [c], H. Borner [r], C. Bosio [q], O. Botner [γ], B. Bouquet [o], M. Bozzo [δ], S. Braibant [f],
P. Branchini [q], K.D. Brand [s], R.A. Brenner [ε], C. Bricman [x], R.C.A. Brown [f], N. Brummer [β],
J.-M. Brunet [t], L. Bugge [ζ], T. Buran [ζ], H. Burmeister [f], C. Buttar [r], J.A.M.A. Buytaert [x],
M. Caccia [η], M. Calvi [η], A.J. Camacho Rozas [n], J.-E. Campagne [f], A. Campion [y],
T. Camporesi [f], V. Canale [q], F. Cao [x], L. Carroll [y], C. Caso [δ], E. Castelli [p],
M.V.Castillo Gimenez [g], A. Cattai [f], F.R. Cavallo [α], L. Cerrito [q], P. Charpentier [f], P. Checchia [θ],
G.A. Chelkov [e], L. Chevalier [c], P. Chliapnikov [u], V. Chorowicz [m], R. Cirio [z], M.P. Clara [z],
J.L. Contreras [g], R. Contri [δ], G. Cosme [o], F. Couchot [o], H.B. Crawley [κ], D. Crennell [d],
M. Cresti [θ], G. Crosetti [δ], N. Crosland [r], M. Crozon [t], J. Cuevas Maestro [n], S. Czellar [ε],
S. Dagoret [o], E. Dahl-Jensen [λ], B. Dalmagne [o], M. Dam [f], G. Damgaard [λ], G. Darbo [δ],
E. Daubie [x], M. Davenport [f], P. David [m], A. De Angelis [p], M. De Beer [c], H. De Boeck [x],
W. De Boer [k], C. De Clercq [x], M.D.M. De Fez Laso [g], N. De Groot [β], C. De La Vaissiere [m],
B. De Lotto [p], A. De Min [η], C. Defoix [t], D. Delikaris [f], P. Delpierre [t], N. Demaria [z],
L.Di Ciaccio [q], A.N. Diddens [β], H. Dijkstra [f], F. Djama [w], J. Dolbeau [t], O. Doll [s], K. Doroba [μ],
M. Dracos [w], J. Drees [s], M. Dris [ξ], W. Dulinski [w], R. Dzhelyadin [u], D.N. Edwards [y], L.-O. Eek [γ],
P.A.-M. Eerola [ε], T. Ekelof [γ], G. Ekspong [l], J.-P. Engel [w], V. Falaleev [u], A. Fenyuk [u],
M.Fernandez Alonso [n], A. Ferrer [g], S. Ferroni [δ], T.A. Filippas [ξ], A. Firestone [κ], H. Foeth [f],
E. Fokitis [ξ], F. Fontanelli [δ], H. Forsbach [s], B. Franek [d], K.E. Fransson [γ], P. Frenkiel [t],
D.C. Fries [k], A.G. Frodesen [i], R. Fruhwirth [b], F. Fulda-Quenzer [o], H. Furstenau [k], J. Fuster [f],
J.M. Gago [a], G. Galeazzi [θ], D. Gamba [z], U. Gasparini [θ], P. Gavillet [f], S. Gawne [y], E.N. Gazis [ξ],
P. Giacomelli [α], K.-W. Glitza [s], R. Gokieli [m], V.M. Golovatyuk [e], A. Goobar [l], G. Gopal [d],
M. Gorski [μ], Y. Gouz [u], V. Gracco [δ], A. Grant [f], F. Grard [x], E. Graziani [q], M.-H. Gros [o],
G. Grosdidier [o], B. Grossetete [m], S. Gumenyuk [u], J. Guy [d], F. Hahn [s], M. Hahn [k], S. Haider [f],
Z. Hajduk [β], A. Hakansson [h], A. Hallgren [γ], K. Hamacher [s], G. Hamel De Monchenault [c],
F.J. Harris [r], B. Heck [f], I. Herbst [s], J.J. Hernandez [g], P. Herquet [x], H. Herr [f], E. Higon [g],
H.J. Hilke [f], T. Hofmokl [μ], R. Holmes [κ], S.-O. Holmgren [l], J.E. Hooper [λ], M. Houlden [y],
J. Hrubec [b], P.O. Hulth [l], K. Hultqvist [l], D. Husson [w], B.D. Hyams [f], P. Ioannou [j],
P.-S. Iversen [i], J.N. Jackson [y], P. Jalocha [π], G. Jarlskog [h], P. Jarry [c], B. Jean-Marie [o],
E.K. Johansson [l], M. Jonker [f], L. Jonsson [h], P. Juillot [w], R.B. Kadyrov [e], G. Kalkanis [j],
G. Kalmus [d], G. Kantardjian [f], F. Kapusta [m], P. Kapusta [π], S. Katsanevas [j], E.C. Katsoufis [ξ],
R. Keranen [ε], J. Kesteman [x], B.A. Khomenko [e], B. King [y], N.J. Kjaer [λ], H. Klein [f], W. Klempt [f],
A. Klovning [i], P. Kluit [x], J.H. Koehne [k], B. Koene [β], P. Kokkinias [ν], M. Kopf [k], M. Koratzinos [f],
K. Korcyl [π], A.V. Korytov [e], B. Korzen [f], C. Kourkoumelis [j], T. Kreuzberger [b], J. Krolikowski [μ],
U. Kruener-Marquis [s], W. Krupinski [π], W. Kucewicz [η], K. Kurvinen [ε], M.I. Laakso [ε],

C. Lambropoulos [ν], J.W. Lamsa [κ], L. Lanceri [p], V. Lapin [υ], J.-P. Laugier [c], R. Lauhakangas [t],
P. Laurikainen [t], G. Leder [b], F. Ledroit [l], J. Lemonne [x], G. Lenzen [s], V. Lepeltier [o],
A. Letessier-Selvon [m], E. Lieb [s], E. Lillestol [f], E. Lillethun [i], J. Lindgren [t], I. Lippi [θ], R. Llosa [g],
M. Lokajicek [e], J.G. Loken [r], M.A. Lopez Aguera [n], A. Lopez-Fernandez [o], D. Loukas [ν],
J.J. Lozano [g], R. Lucock [d], B. Lund-Jensen [γ], P. Lutz [l], L. Lyons [r], G. Maehlum [f],
N. Magnussen [s], J. Maillard [l], A. Maltezos [ν], F. Mandl [b], J. Marco [n], J.-C. Marin [f], A. Markou [ν],
L. Mathis [l], C. Matteuzzi [η], G. Matthiae [q], M. Mazzucato [θ], M.Mc Cubbin [y], R.Mc Kay [κ],
E. Menichetti [z], C. Meroni [η], W.T. Meyer [κ], W.A. Mitaroff [b], G.V. Mitselmakher [e],
U. Mjoernmark [h], T. Moa [l], R. Moeller [λ], K. Moenig [s], M.R. Monge [δ], P. Morettini [δ],
H. Mueller [k], H. Muller [f], G. Myatt [r], F. Naraghi [m], U. Nau-Korzen [s], F.L. Navarria [α],
P. Negri [η], B.S. Nielsen [λ], M. Nigro [θ], V. Nikolaenko [υ], V. Obraztsov [υ], R. Orava [t],
A. Ostankov [υ], A. Ouraou [c], R. Pain [m], H. Palka [π], T. Papadopoulou [ζ], L. Pape [f], P. Pasini [α],
A. Passeri [q], M. Pegoraro [θ], V. Perevozchikov [υ], M. Pernicka [b], M. Pimenta [a], O. Pingot [x],
C. Pinori [θ], A. Pinsent [r], M.E. Pol [a], G. Polok [π], P. Poropat [p], P. Privitera [α], A. Pullia [η],
J. Pyyhtia [t], A.A. Rademakers [β], D. Radojicic [r], S. Ragazzi [η], W.H. Range [y], P.N. Ratoff [r],
A.L. Read [ζ], N.G. Redaelli [η], M. Regler [b], D. Reid [y], P.B. Renton [r], L.K. Resvanis [j],
F. Richard [o], J. Ridky [e], G. Rinaudo [z], I. Roditi [f], A. Romero [z], P. Ronchese [θ], E.I. Rosenberg [κ],
U. Rossi [α], E. Rosso [f], P. Roudeau [o], T. Rovelli [α], V. Ruhlmann [c], A. Ruiz [n], H. Saarikko [t],
Y. Sacquin [c], E. Sanchez [g], J. Sanchez [g], E. Sanchis [g], M. Sannino [δ], M. Schaeffer [w],
H. Schneider [k], F. Scuri [p], A. Sebastia [g], A.M. Segar [r], R. Sekulin [d], M. Sessa [p], G. Sette [δ],
R. Seufert [k], R.C. Shellard [f], P. Siegrist [c], S. Simonetti [δ], F. Simonetto [θ], A.N. Sissakian [e],
T.B. Skaali [ζ], J. Skeens [κ], G. Skjevling [ζ], N.E. Smirnov [υ], G.R. Smith [d], R. Sosnowski [μ],
K. Spang [λ], T. Spassoff [e], E. Spiriti [q], S. Squarcia [δ], H. Staeck [s], C. Stanescu [q], G. Stavropoulos [ν],
F. Stichelbaut [x], A. Stocchi [η], J. Strauss [b], R. Strub [w], C.J. Stubenrauch [f], M. Szczekowski [μ],
M. Szeptycka [μ], P. Szymanski [μ], S. Tavernier [x], G. Theodosiou [ν], A. Tilquin [l], J. Timmermans [β],
V.G. Timofeev [e], L.G. Tkatchev [e], D.Z. Toet [β], A.K. Topphol [i], L. Tortora [q], D. Treille [f],
U. Trevisan [δ], G. Tristram [l], C. Troncon [η], E.N. Tsyganov [e], M. Turala [π], R. Turchetta [w],
M.-L. Turluer [c], T. Tuuva [t], I.A. Tyapkin [e], M. Tyndel [d], S. Tzamarias [f], F. Udo [β],
S. Ueberschaer [s], V.A. Uvarov [υ], G. Valenti [α], E. Vallazza [z], J.A.Valls Ferrer [g],
G.W. Van Apeldoorn [β], P. Van Dam [β], W.K. Van Doninck [x], N. Van Eijndhoven [f],
C. Vander Velde [x], J. Varela [a], P. Vaz [a], G. Vegni [η], M.E. Veitch [r], J. Velasco [g], L. Ventura [θ],
W. Venus [d], F. Verbeure [x], L.S. Vertogradov [e], L. Vibert [m], D. Vilanova [c], E.V. Vlasov [υ],
A.S. Vodopyanov [e], M. Vollmer [s], G. Voulgaris [j], M. Voutilainen [t], V. Vrba [e], H. Wahlen [s],
C. Walck [l], F. Waldner [p], M. Wayne [κ], A. Wehr [s], P. Weilhammer [f], J. Werner [s],
A.M. Wetherell [f], J.H. Wickens [x], J. Wikne [ζ], W.S.C. Williams [r], M. Winter [w], D. Wormald [ζ],
G. Wormser [o], K. Woschnagg [γ], N. Yamdagni [l], P. Yepes [β], A. Zaitsev [υ], A. Zalewska [π],
P. Zalewski [μ], P.I. Zarubin [e], E. Zevgolatakos [ν], G. Zhang [s], N.I. Zimin [e], R. Zitoun [m],
R.Zukanovich Funchal [l], G. Zumerle [θ] and J. Zuniga [g]

[a] *LIP, Av. Elias Garcia 14 - 1e, P-1000 Lisbon Codex, Portugal*
[b] *Institut für Hochenergiephysik, Österreichische Akademie der Wissenschaften, Nikolsdorfergasse 18, A-1050 Vienna, Austria*
[c] *DPhPE, CEN-Saclay, F-91191 Gif-Sur-Yvette Cedex, France*
[d] *Rutherford Appleton Laboratory, Chilton, Didcot OX11 0QX, UK*
[e] *Joint Institute for Nuclear Research, Dubna, Head Post Office, P.O. Box 79, SU-101 000 Moscow, USSR*
[f] *CERN, CH-1211 Geneva 23, Switzerland*
[g] *Instituto de Fisica Corpuscular (IFIC), Centro Mixto Universidad de Valencia-CSIC, Avda. Dr. Moliner 50, E-46100 Burjassot (Valencia), Spain*
[h] *Department of Physics, University of Lund, Sölvegatan 14, S-223 63 Lund, Sweden*
[i] *Department of Physics, University of Bergen, Allégaten 55, N-5007 Bergen, Norway*
[j] *Physics Laboratory, University of Athens, Solonos Street 104, GR-10680 Athens, Greece*
[k] *Institut für Experimentelle Kernphysik, Universität Karlsruhe, Postfach 6980, D-7500 Karlsruhe 1, FRG*
[l] *Institute of Physics, University of Stockholm, Vanadisvägen 9, S-113 46 Stockholm, Sweden*
[m] *LPNHE, Universités Paris VI et VII, Tour 33 (RdC), 4 place Jussieu, F-75230 Paris Cedex 05, France*
[n] *Facultad de Ciencias, Universidad de Santander, av. de los Castros, E-39005 Santander, Spain*
[o] *Laboratoire de l'Accélérateur Linéaire, Université de Paris-Sud, Bâtiment 200, F-91405 Orsay, France*
[p] *Dipartimento di Fisica, Università di Trieste and INFN, Via A. Valerio 2, I-34127 Trieste, Italy*

and Istituto di Fisica, Università di Udine, Via Larga 36, I-33100 Udine, Italy
- Istituto Superiore di Sanità, Istituto Nazionale di Fisica Nucleare (INFN), Viale Regina Elena 299, I-00161 Rome, Italy
and Dipartimento di Fisica, Università di Roma II and INFN, Tor Vergata, I-00173 Rome, Italy
- Nuclear Physics Laboratory, University of Oxford, Keble Road, Oxford OX1 3RH, UK
- Fachbereich Physik, University of Wuppertal, Postfach 100 127, D-5600 Wuppertal 1, FRG
- Laboratoire de Physique Corpusculaire, Collège de France, 11 place M. Berthelot, F-75231 Paris Cedex 5, France
- Institute for High Energy Physics, Serpukhov, P.O. Box 35, SU-142 284 Protvino (Moscow Region), USSR
- Greek Atomic Energy Commission, Nuclear Research Centre Demokritos, P.O. Box 60228, GR-15310 Aghia Paraskevi, Greece
- Division des Hautes Energies, CRN–Groupe DELPHI, B.P. 20 CRO, F-67037 Strasbourg Cedex, France
- Physics Department, Universitaire Instelling Antwerpen, Universiteitsplein 1, B-2610 Wilrijk, Belgium
and IIHE, ULB–VUB, Pleinlaan 2, B-1050 Brussels, Belgium
and Service de Physique des Particules Elémentaires, Faculté des Sciences, Université de l'Etat Mons, Av. Maistriau 19, B-7000 Mons, Belgium
- Department of Physics, University of Liverpool, P.O. Box 147, Liverpool L69 3BX, UK
- Dipartimento di Fisica Sperimentale, Università di Torino and INFN, Via P. Giuria 1, I-10125 Turin, Italy
- Dipartimento di Fisica, Università di Bologna and INFN, Via Irnerio 46, I-40126 Bologna, Italy
- NIKHEF-H, Postbus 41882, NL-1009 DB Amsterdam, The Netherlands
- Department of Radiation Sciences, University of Uppsala, P.O. Box 535, S-751 21 Uppsala, Sweden
- Dipartimento di Fisica, Università di Genova and INFN, Via Dodecaneso 33, I-16146 Genoa, Italy
- Department of High Energy Physics, University of Helsinki, Siltavuorenpenger 20 C, SF-00170 Helsinki 17, Finland
- Physics Department, University of Oslo, Blindern, N-1000 Oslo 3, Norway
- Dipartimento di Fisica, Università di Milano and INFN, Via Celoria 16, I-20133 Milan, Italy
- Dipartimento di Fisica, Università di Padova and INFN, Via Marzolo 8, I-35131 Padua, Italy
- Ames Laboratory and Department of Physics, Iowa State University, Ames IA 50011, USA
- Niels Bohr Institute, Blegdamsvej 17, DK-2100 Copenhagen Ø, Denmark
- Institute for Nuclear Studies, and University of Warsaw, Ul. Hoża 69, PL-00681 Warsaw, Poland
- Physics Department, National Technical University, Zografou Campus, GR-15773 Athens, Greece
- High Energy Physics Laboratory, Institute of Nuclear Physics, Ul. Kawiory 26 a, PL-30055 Cracow 30, Poland

Appendix B

Readout System

In this appendix we describe the MUB readout system. First we give an overview of the DELPHI data acquisition system (**DAS**) taken mainly from [21].

B.1 Overview

The Readout System is based on the FASTBUS standard. The aim is to read and record events at up to a few Hz. The system divides into three main phases:

B.1.1 First and Second Level Readout Phase

This phase is synchronous with the Beam Cross Over (BCO), which occurs every 22 μs. The accumulation of data in detectors' Front End Buffers (FEBs) takes anything from a few hundred nanoseconds to about 22 μs for the TPC. The first level trigger decision is taken 3 μs after BCO. If it is positive, the second level trigger phase is started, and this decision is taken 39 μs after BCO. If it is negative, the present data are aborted. Note that one or two BCOs will have been missed. If the second level decision is positive, there is a 3.5 ms deadtime while detectors' front ends are freed.

The whole sequence is controlled by the Trigger Supervisor ('ZEUS'). Each detector has a Local Trigger Supervisor ('PANDORA').

B.1.2 The Main Readout Phase

If the event is passed by the Second Level Trigger, the data in the Front End Buffers are transferred to the Crate Event Buffer (CEB) by the Crate Processor. During this process, data reduction (zero suppression) and formatting are done (and also third level processing in the future). The data in the CEBs are then transferred to a four event deep Multi-Event Buffer (MEB) for each detector. The data transfer tasks in this phase are handled for each detector by a Local Event Supervisor (LES), under the control of a global Event Supervisor (ES). Processing of the third level trigger (which had not yet been enabled by the end of the 1990 run) is performed in parallel and data in the MEB is aborted in the case of a negative decision.

At the end of the readout phase, the data exist in 15 MEBs (mostly one per detector).

Event Tagging and Data Storage

The task of transferring data from the MEBs to the Global Event Buffer (GEB) is handled by the Global Event Controller (GEC)[1].

Fourth level Tagging (implemented on emulators) is designed for fast physics analysis and rejection of background. Its results are added to the data in the GEB before it is transferred to the data acquisition computer (a VAX8700).

B.2 Barrel Muon Readout System

A schematic diagram of the important components of the MUB readout system is shown in figure 3.3.

MUB, TOF and MUF/HOF share the same Equipment Computer (MicroVax) and the same Equipment Computer [FASTBUS] Crate (ECC), situated in D1 (the counting room devoted to DAS hardware).

MUB is divided into two sub-detectors (essentially by the plane $x = 0$ in the DELPHI frame) which are identical but which have separate triggering and data acquisition systems. All anode and delay line signals are fed to amplifier/discriminator boxes on the DELPHI Barrel and half are sent to each of two counting rooms, called 'B2' and 'D2'. In each counting room there is one FASTBUS crate, one CAMAC crate, and a Multiplexer. Since very few chambers fire in any one event, signals are multiplexed six-fold before being digitised.

Each FASTBUS crate holds the following modules:—

[1]In fact, by the end of 1990 running, the ES and the GEC had been combined into one Global Event Supervisor (GES).

- 7 LEP Time Digitisers (LTDs [26]): each module handles 48 channels and has multihit capability;
- 1 Hit Latch Buffer: this module contains one bit for each input channel of the Multiplexor, indicating whether or not a hit occurred in that channel;
- 1 PANDORA (Local Trigger Supervisor Control Box): this module communicates with the central DELPHI trigger control and transmits Warning and Clock signals;
- 1 Local Trigger Supervisor Fan Out (LTS-FO): this module distributes timing signals received from PANDORA to the LTDs;
- 1 FASTBUS Intersegment Processor (FIP [63]): this module serves as a Front End Freeing Controller (FEFC) and a Crate Processor (CP);
- 1 FASTBUS Branch Driver (FBD): this provides an interface to the local trigger system, loads its decision tables and reads out its decisions.

The CAMAC crate houses the Local Trigger Supervisor Decision Box (LTS-DB), which receives all anode signals from the Multiplexor and stores anode hit pattern information which is used to provide a MUB first and second level trigger decision for use in the Muon Subtrigger.

The readout architecture allows any partition to be running in the main DAS readout (in 'global') or in standalone, diagnostic mode. When the CP receives a T2-YES interrupt from PANDORA (meaning the second-level trigger decision is positive) it transfers data from the front end electronics into the Front End Buffers (FEBs) (this is called 'Front End Freeing'). It then writes the accounting number of the next event into a free FEB and sends PANDORA a signal to indicate readiness (called NEI-DONE or Next Event Initialisation Done). PANDORA then sends a similar signal (FE-RDY or Front End Ready) to ZEUS. If ZEUS receives FE-RDYs from all partitions in the global readout, it sends out a so-called WNG-BCO to all PANDORAs just before the next beam cross-over. Asynchronously, the FIP transfers the data from the FEBs to the Crate Event Buffer(CEB).

The physical CEB is divided into four logical CEBs — one each for RAW data, T1/T2 data, LT3 (local third level trigger) data, and 'Processed' data. During 1990 running, the T3 and the Processed Data blocklets were dummy.

B.2.1 The Equipment Computer Crate (ECC)

The Front End Crates in B2 and D2 are connected to the ECC (in D1) over a FASTBUS cable from their FIPs. In the ECC a single FIP is used for the MUB LES and the MUF/HOF LES. The Equipment Computer is interfaced to the ECC by means of a CERN FASTBUS Interface (CFI). The ECC also contains a Segment Interconnect (SI) to connect to the central Event Supervisor crate.

The software in the LES supervises the transfer of data from CEB to MEB and formats it into ZEBRA banks [34]. Data in the MEB are copied into the Spy Event Buffer, from where it may be read into the Equipment Computer (via the CFI), where online monitoring tasks may access it via the Model Buffer Manager. The Barrel Muon monitoring task ('MUONLINE' [32]), is a version of the offline data analysis module with many additional error finding routines. So far it has been run extensively only in an offline mode after the data have been written to a special disk area on the operations computer (usually an hour or so after it was collected).

B.2.2 MUB T1/T2

The aim of the MUB 1st/2nd level trigger is to provide a trigger within 3 μs for single muons passing through the Barrel Muon Chambers. It was installed and read out for the 1990 running, but not used as an active trigger.

The muon signature is based upon combinations of hit patterns from anode wire information only [61].

It is intended to be used in 1991 in coincidence with the TOF to reduce the rate (predominantly from cosmics) to bring it well within the limit of 5 Hz imposed by the input to the third level trigger.

B.2.3 MUB T3

Local T3 processing will be performed in the FIPs by routines called from a task running asynchronously with tasks performing front-end freeing and readout.

Rough coordinates of the MUB hit points (θ and ϕ) are produced from a series of look-up tables for use by the global T3 processor [62].

Appendix C

Description of Selected EMMASS Routines

This appendix contains a description of selected EMMASS routines. Routines which are general to both the MUB and the MUF, and routines which are specific to the MUB are described.

C.1 General Code

EMMFIT

Called : For each chosen combination of tracks and MUB or MUF space points.

Purpose: Common fitting routine for MUB and MUF to fit the track to the Muon Chamber hits and calculate the χ^2_G, χ^2_M and χ^2_{ex} and the fit results.

Method : The matrix method outlined in Chapter 4 is used.

EMMTER

Called : For each space point (TER) in MUB or MUF to which the track is fitted.

Purpose: To create new TERs with the added words tabulated in Chapter 4 and to disable the original banks .

Method : Using TANAGRA routines TELEM and TABLE.

EMMSEL

Called : Once per event.

Purpose: To activate the best solution (TER) where there are multiple associations (i.e. several TERs hanging off the same TE header representing the association of one hit to several tracks).

Method : The solutions are activated where there are the most layers associated to a single track. Where two tracks have the same number of layers associated to them, TERs associated to the track with the smaller global χ^2_G are activated.

C.2 Barrel Muon Chamber Code

EMMTEB

Called : Once per event

Purpose: To collect together all MUB hits

Method : A call is made to TLIST to obtain the IDs of all activated *and* deactivated TERs. The relevant data for all the MUB hits in the event are picked up from the TER banks through calls to TGET and arranged in layer by layer order, in arrays called TMUB and DTMUB:

TMUB(LAYER NUMBER , HIT NUMBER , 1) = R

TMUB(LAYER NUMBER , HIT NUMBER , 2) = $R\phi$

TMUB(LAYER NUMBER , HIT NUMBER , 3) = z

DTMUB(LAYER NUMBER , HIT NUMBER , 1) = $\sigma^2_{R\phi}$

DTMUB(LAYER NUMBER , HIT NUMBER , 2) = σ^2_z

In this case, $\sigma^2_{R\phi}$ and σ^2_z are the squares of the MUB measurement error on the coordinates $R\phi$ and z. To a good approximation, the error on $R\phi$ is equal to the error on the drift distance measurement. The error on z is equal to the error on the distance measured along the chambers' delay line.

Comments: Several result data may co-exist for the same header. This means that although there is only one TE for each MUB space point, there may be two TERs where there is left-right ambiguity. Only one of these TERs may be active — the creation of a new alternative TER will automatically cause TANAGRA to deactivate an existing TER. Therefore, it is arbitrary which of two TERs is active, and it is essential to pick up both activated and dectivated MUB TERs.

If there is no data in the Barrel Muon Chambers, all processing for this event in the Barrel code of EMMASS stops here.

EMMTKB

Called : Once per event

Purpose: To collect together all extrapolated track impact points

Method : The results of the extrapolations are in TKX banks, which are defined for every reference surface intersected by the track. In this routine, the ID numbers of the TKX banks are arranged in the format

IDTRB(TRACK NUMBER , 1) = ID of TKX bank in INNERS

IDTRB(TRACK NUMBER , 2) = ID of TKX bank in OUTERS

IDTRB(TRACK NUMBER , 3) = ID of TKX bank in PERIPHERALS

Comments: Because the reference surfaces are cylinders of finite length, it is possible that TKX banks will not be defined on all three surfaces. If there are no TKX banks defined (i.e. no extrapolated tracks) on the MUB reference surfaces, all processing in this event in the Barrel section of EMMASS stops here.

A loop is now performed over all the extrapolated tracks...

EMMEXB

Called : Once per extrapolated track

Purpose: To obtain the impact points of the extrapolated tracks in the plane of the Muon Chambers

Method : Impact points for the extrapolated tracks are defined on cylinders close to the 24-sided MUB polygons . A local extrapolation is necessary to obtain the hit points for the extrapolated track in the plane of the Muon Chambers. A straight line extrapolation is performed using the momentum vector in the TKX bank. Use is made of the full MUB geometry database because several chambers, particularly in the Outers and Peripherals, are at anomalous radii. The results are stored in the EXMUB array:

EXMUB(ILAY, 1) = R of extrapolated track in layer ILAY

EXMUB(ILAY, 2) = $R\phi$ of extrapolated track in layer ILAY

EXMUB(ILAY, 3) = z of extrapolated track in layer ILAY

Next the matrices ATB and VIB, which will be input to the fitting routine EMMFIT, are prepared. Matrix inversion is performed using the routine EMMINV, which is a slight modification of the CERN library routine SXMINV.

EMMCSB

Called : Once per extrapolated track

Purpose: To select all MUB hits close to this track

Method : The χ^2 between each MUB hit and this extrapolated track is calculated, using the difference between the extrapolated hit point in the relevant layer and the MUB hit point, together with the MUB measurement errors and (co-)variances in the TKX bank error matrix (representing propagated measurement errors and the multiple scattering error ellipse).

Those MUB hits with a χ^2 less than TKCUT with this track are copied into the TMUBA and DTMUBA arrays, which have the same form as TMUB and DTMUB above.

EMMMJB

Called : Once per extrapolated track

Purpose: Controls the calls to the fitting routine EMMFIT

Method : The following arrays must be passed to EMMFIT:

T(ILAY,1), T(ILAY,2) : the measured coordinates ($R\phi$ and z) of the MUB hit in layer ILAY to which the track is to be fitted

DT(ILAY,1), DT(ILAY,2) : the $\sigma^2_{R\phi}$ and σ^2_z of this hit

EXT(ILAY,1) , EXT(ILAY,2) : $R\phi$ and z of extrapolated track in layer ILAY

EMMFIT returns the χ^2 of the fit. There may be two or more hits in one layer associated with the track, especially if there is left-right ambiguity. A maximum of one hit in any one layer is used in the final fit. The combination of hits which gives the best χ^2 in the fit is chosen and output.

The fit 'fails' if the returned χ^2 per degree of freedom is greater than CHISEL. Suppose there are NP layers with a hit associated with the track. If the fit fails , we find the best fit with all combinations with NP-1 layers (i.e. each MUB hit is successively 'dropped'). If necessary, we may try NP-2, NP-3 etc...

If there is no good fit, the best fit with one layer associated is kept.

Once the best combination has been found, the arrays GLOB and DLAY, containing respectively global and layer information for the fit, are filled and input to EMMTER.

Appendix D

Description of Selected Routines for Muon Detector Simulation in FASTSIM

'SPMSIM' is the last simulation module called in FASTSIM. It handles the fast simulation of both the Barrel and the End-Cap Muon Chambers. It has among its input, the following parameters, calculated in MUTRACK [41] for each track which reaches the Muon Chambers:

- In common block EXMUBH, the impact points in the Barrel Muon Chambers in each of the seven chamber layers (3 Inner, 2 Outer, 2 Peripheral), given in terms of the R,$R\phi$, and z.
- In common EXMUBV, variances and covariances including the variances in $R\phi$ and in z for each of the three layers of modules and the covariances between Inners and Outers, Inners and Peripherals, and Outers and Peripherals in $R\phi$ and z.
- In common EXMUFH, the hit points in the Forward Muon Chambers in DELPHI x and y.
- In common EXMUFV, variances in x and y for each layer of quadrants, and covariances between layers.

The main aims of the code in SPMSIM are to obtain the hit points after allowing for realistic multiple scattering, check whether these *smeared* tracks strike chambers or dead space, and obtain the hit points as *seen* by the chambers, for storage in the TE-BANKS.

The first action in SPMSIM, after initialising local variables, is to decide whether the track in question is in the Barrel or in one of the End-Caps. The program then steps through a series of routines, with names SPMuXX, where u='B' for a track in the Barrel, and u='F' for a track in one of the End-Caps.

As the example, we describe the Barrel routines. The End-Cap routines are exactly analogous.

D.1 SPMBSH

If the user sets the flag ITMULS in the FASTSIM title file to 1, hit points are smeared for the effect of multiple scattering in the routines SPMuSH. An idea of the size of the deviation due to this effect for muons of different momenta is given in figure D.1 (in DELPHI, the muon track length in iron is about 1 m).

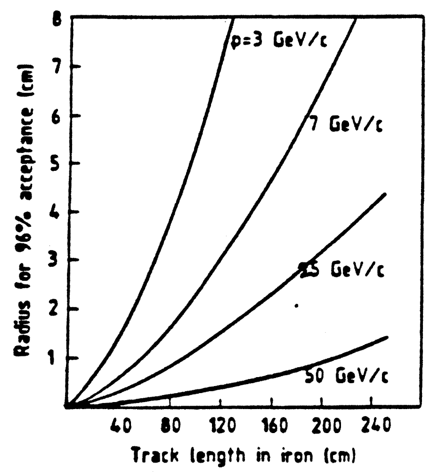

Figure D.1: Radius of 96% acceptance circle for multiply scattered muons as a function of the muon track length in iron and of muon momentum (from [65]).

Let us call the deterministic track (the track the particle would take if there were no multiple scattering) the z axis. The mean angular deflection projected in the x-z plane, due to electromagnetic interactions between z and $z + dz$, is given by [64]:

$$d\theta = \frac{k\sqrt{dz}}{\beta(z)p(z)} \tag{D.1}$$

where p is the particle's momentum and k is a constant given approximately by

$$k = \frac{16\ \mathrm{MeV}}{\sqrt{\mathrm{X}_0}} \tag{D.2}$$

X_0 being the radiation length of the material at this point.

Therefore, if the Inners are at z_1, say, the mean displacement in x at the Inners due to deflection in the interval near z is

$$dx_1 = (z_1 - z)d\theta \tag{D.3}$$

Therefore

$$(dx_1)^2 = \frac{k^2(z_1 - z)^2 dz}{(p\beta)^2} \tag{D.4}$$

Hence, the mean square displacement perpendicular to the deterministic track due to scattering in all intervals up to z_1 is given by:

$$\sigma_{x_1}^2 = k^2 \int_0^{z_1} \frac{(z_1 - z)^2 dz}{(p\beta)^2} \tag{D.5}$$

Similarly, we may write for the Outers (if they are at z_2)

$$\sigma_{x_2}^2 = k^2 \int_0^{z_2} \frac{(z_2 - z)^2 dz}{(p\beta)^2}$$

Clearly, these deflections are correlated. A particle which has been deflected in the positive x-direction before striking the Inners, is more likely to be found with a positive x-displacement when it hits the Outers. The Inners-Outers covariance is given by

$$\rho_{12}\sigma_{x_1}\sigma_{x_2} = k^2 \int_0^{z_1} \frac{(z_1 - z)(z_2 - z)dz}{(p\beta)^2} \tag{D.6}$$

where ρ_{12} is the 'correlation coefficient' between the Inners and the Outers.

Now, the general expression for a Gaussian distribution in two variables is (see for instance [58])

$$P(x_1, x_2) = N \exp\left\{\frac{-1}{2}\left(\frac{1}{1-\rho_{12}^2}\right)\left(\frac{x_1^2}{\sigma_{x_1}^2} + \frac{x_2^2}{\sigma_{x_2}^2} - \frac{2\rho_{12}x_1x_2}{\sigma_{x_1}\sigma_{x_2}}\right)\right\} \tag{D.7}$$

where N is a normalisation constant.

From the CERN library routine SXRNG we obtain two numbers, A and B say, which are from a Gaussian distribution with a unit variance. That is

$$P(A) \propto \exp\left(-A^2/2\right) \tag{D.8}$$

$$P(B) \propto \exp\left(-B^2/2\right) \tag{D.9}$$

Now, x_1 can only depend on σ_{x_1}. We first fix x_1 by

$$x_1 = A \times \sigma_{x_1} \tag{D.10}$$

The distribution in x_2 becomes

$$P(x_2) \propto \exp\left\{\frac{-1}{2}\left(\frac{1}{1-\rho_{12}^2}\right)\left(\frac{x_2^2}{\sigma_{x_2}^2} - \frac{2\rho_{12}x_1x_2}{\sigma_{x_1}\sigma_{x_2}}\right)\right\} \tag{D.11}$$

which we may rewrite as

$$P(y) \propto \exp\left\{\frac{-y^2}{2}\right\} \tag{D.12}$$

where

$$y = \frac{1}{\sqrt{1-\rho_{12}^2}}\left(\frac{x_2}{\sigma_{x_2}} - \frac{\rho_{12}x_1}{\sigma_{x_1}}\right) \tag{D.13}$$

Hence, setting $y = B$ and using the above equation for x_1, we find finally

$$x_2 = B\sigma_{x_2}\sqrt{1-\rho_{12}^2} + A\rho_{12}\sigma_{x_2} \tag{D.14}$$

In this way, we obtain the *smeared* hit points which are the input to the rest of the routines, if multiple scattering is selected by the user[1].

D.2 SPMBCH

Each chamber in the barrel has a unique integer indentifier. For each layer:

ICH(ILAYER)= 100×ISECT+10×ILAYER+ICHAMB

ILAYER is the layer number (1 to 7), ISECT is the sector number (1 to 50 in the convention adopted here) and ICHAMB is the chamber number within the layer (counting left to right looking outwards from the centre of DELPHI). We obtain ICH in SPMBCH, having first converted into the local coordinate frame of the module (using SPMTOX). We also determine here whether the track missed the chambers (because it was between modules, or between chambers within a module) and obtain the drift distance.

D.3 SPMBDS

Other Dead Space, particularly in non-standard modules, is described in SPMBDS. Considerations include (see Appendix of [25]):

- nylon endplugs with electronics at each end of each chamber

[1] In the Barrel, there is a further layer of modules — the Peripherals — for which we find the hit point using the displacement in the plane of the Outers (x_2) and the Outers/Peripherals correlation coefficient.

- cryogenic ducts and cable ducts
- gaps for magnet legs in Outers and Peripherals
- further non-standard modules in Peripherals

The extent of these dead areas may be illustrated for the Barrel by plotting $R\phi$ against z for the Muon Chamber hits for large numbers of muons (for each layer independently). Two such scatter plots are shown in figure D.2.

In the End-Caps, the square hole around the beam pipe and the gaps between the four quadrants are described.

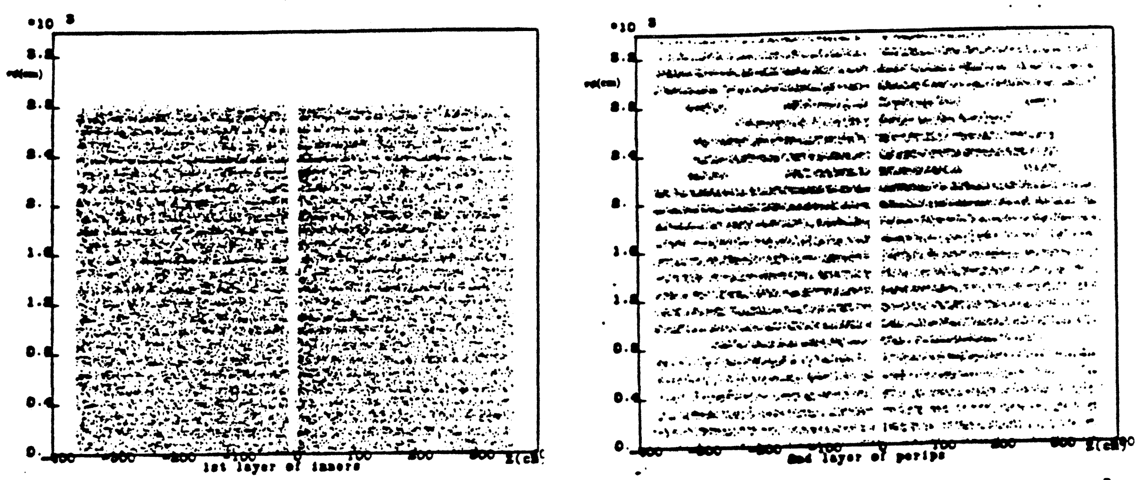

Figure D.2: Scatter plot of muon hits in the Barrel Muon Chambers. The hits for 100,000 muon-pair events are shown in the $(R\phi, z)$ plane. In the first layer of the Inners (left) there is very little dead space except at $z = 0$. In the second layer of the Peripherals (right) we see additional areas which are not covered by Muon Chambers between modules, every 15° in ϕ (these areas are covered by chambers in the Outers). There are four holes for the Solenoid support legs, and some modules are shorter than average to allow space for cryogenic and cable ducts.

D.4 SPMBMH

The hit as reconstructed by the Barrel Muon Chambers is established in SPMBMH. Within a chamber there is a small amount of dead space (e.g. at the supports for the anode wire). A typical estimate of the chamber's resulting overall efficiency is 95%. A call is to a uniform distribution random number generator to determine if the hit is detected. Then the impact point is smeared for measurement error using SXRNG. The measurement errors on $R\phi$ and z are not correlated (these errors and the chamber efficiency are set at the start of each run in the routine SPMINI).

D.5 SPMBTE

The purpose of SPMBTE is to produce TE-banks compatible with those obtained in the DELPHI analysis processors, MUBANA and MUFANA. Most of the data in the results bank are the same for each hit and default values for these quantities are set in SPMINI at the start of the run. Two TER banks are created where there is left-right ambiguity.

Appendix E
Publications of the LEP Experiments

DELPHI publications up to November 27th, 1990:

DELPHI

CERN–EP/89–134	Measurement of the Mass and Width of the Z^0-Particle from Multihadronic Final States Produced in e^+e^- Annihilations P. Aarnio et al. 16 October 1989 **Phys. Lett. 231B (1989) 539**
CERN–EP/90–19	Study of Hadronic Decays of the Z^0 Boson P. Aarnio et al. 9 February 1990 **Phys. Lett. 240B (1990) 271**
CERN–EP/90–31	Study of the Leptonic Decays of the Z^0 Boson P. Aarnio et al. 9 March 1990 **Phys. Lett. 241B (1990) 425**
CERN–EP/90–32	A Precise Measurement of the Z Resonance Parameters Through its Hadronic Decays P. Abreu et al. 9 March 1990 **Phys. Lett. 241B (1990) 435**
CERN–EP/90–33	Search for Heavy Charged Scalars in Z^0 Decays P. Abreu et al. 9 March 1990 **Phys. Lett. 241B (1990) 449**
CERN–EP/90–44	Search for Light Neutral Higgs Particles Produced in Z^0 Decays P. Abreu et al. 4 April 1990 **Nucl. Phys. B342 (1990) 1**

DELPHI Continued

CERN–EP/90–46	Search for the t and b' Quarks in Hadronic Decays of the Z^0 Boson P. Abreu et al. 6 April 1990 **Phys. Lett. 242B (1990) 536**
CERN–EP/90–60	Search for Pair Production of Neutral Higgs Bosons in Z^0 Decays P. Abreu et al. 9 May 1990 **Phys. Lett. 245B (1990) 276**
CERN–EP/90–78	A Study of Intermittency in Hadronic Z^0 Decays P. Abreu et al. 6 June 1990 **Phys. Lett. 247B (1990) 137**
CERN–EP/90–79	Search for Scalar Quarks in Z^0 Decays P. Abreu et al. 6 June 1990 **Phys. Lett. 247B (1990) 148**
CERN–EP/90–80	Search for Sleptons and Gauginos in Z^0 Decays P. Abreu et al. 6 June 1990 **Phys. Lett. 247B (1990) 157**
CERN–EP/90–89	A Comparison of Jet Production Rates on the Z^0 Resonance to Perturbative QCD P. Abreu et al. 22 June 1990 **Phys. Lett. 247B (1990) 167**
CERN–PPE/90–117	Charged Multiplicity and Rapidity Distributions in Z^0 Hadronic Decays P. Abreu et al. 30 July 1990 to be published in **Zeit. Phys. C(1990)**
CERN–PPE/90–118	A Measurement of the Partial Width of the Z^0 Boson into b Quark Pairs P. Abreu et al. **Paper presented at the Singapore Conference** **August 1990**

DELPHI Continued

CERN–PPE/90–119	DELPHI Results on the Z^0 Resonance Parameters Through its Hadronic and Leptonic Decay Modes P. Abreu et al. **Paper presented at the Singapore Conference** **August 1990**
CERN–PPE/90–122	Energy–Energy Correlations in Hadronic Final States from the Z^0–Decays P. Abreu et al. 29 August 1990 **Phys. Lett. 252B (1990) 149**
CERN–PPE/90–123	Measurement of the Partial Width of the Decay of the Z^0 into Charm Quark Pairs P. Abreu et al. 29 August 1990 **Phys. Lett. 252B (1990) 140**
CERN–PPE/90–128	The DELPHI Detector at LEP P. Aarnio et al. 13 September 1990 to be published in **Nucl. Instrum. Methods (1990)**
CERN–PPE/90–163	Search for Higgs Bosons Using the DELPHI Detector P. Abreu et al. 7 November 1990 **Paper presented at the Singapore Conference,** **August 1990**
CERN–PPE/90–167	Search for Non-Standard Z^0 Decays in Two–Particle Final States P. Abreu et al. 13 November 1990 **Paper presented at the Singapore Conference,** **August 1990**

DELPHI Continued

CERN–PPE/90–173	Charged Particle Multiplicity Distributions in Z^0 Hadronic Decays P. Abreu et al. 16 November 1990 to be published in **Zeit. Phys. C**
CERN–PPE/90–174	Experimental Study of the Triple–Gluon Vertex P. Abreu et al. 16 November 1990 to be published in **Phys. Lett.B**

Some publications of the other three LEP experiments which are relevant to the subject matter of this thesis:

ALEPH

CERN–EP/89–141	Determination of the Leptonic Branching Ratios of the Z D. Decamp et al. 2 November 1989 **Phys. Lett. 234B (1990) 399**
CERN–PPE/90–104	Measurement of Electroweak Parameters from Z Decays into Fermion Pairs D. Decamp et al. 19 July 1990 to be published in **Zeit. Phys. C**

L3

L3 Preprint #003	Measurement of g_A and g_V, the Neutral Current Coupling Constants to Leptons B. Adeva et al. 24 November 1989 **Phys. Lett. 236B (1990) 109**
L3 Preprint #005	A Measurement of the Z^0 Leptonic Partial Widths and the Forward–Backward Asymmetry B. Adeva et al. 5 February 1990 **Phys. Lett. 238B (1990) 122**
L3 Preprint #008	A Determination of Electroweak Parameters from $Z^0 \rightarrow \mu^+\mu^-(\gamma)$ B. Adeva et al. 21 June 1990 **Phys. Lett. 247B (1990) 473**
L3 Preprint #017	A Determination of Electroweak Parameters from Z^0 Decays into Charged Leptons B. Adeva et al. 20 August 1990 **Phys. Lett. 250B (1990) 183**

OPAL

CERN–EP/89–147	Measurement of the Decay of the Z^0 into Lepton Pairs M.Z. Akrawy et al. 13 November 1989 **Phys. Lett. 235B (1990) 379**
CERN–EP/90–27	A Combined Analysis of the Hadronic and Leptonic Decays of the Z^0 M.Z. Akrawy et al. 23 February 1990 **Phys. Lett. 240B (1990) 497**
CERN–EP/90–81	Analysis of Z^0 Couplings to Charged Leptons M.Z. Akrawy et al. 11 June 1990 **Phys. Lett. 247B (1990) 458**

Glossary

BCO Beam Cross-Over.

BM Block Mover.

BRICH Barrel Ring Imaging Cherenkov Counter.

CAEN Intelligent High Voltage power supply used for most of DELPHI.

CCA Combined Calorimetry.

CEB Crate Event Buffer.

CERN Conseil Europeen pour la Recherche Nucleaire.

CFI CERN FASTBUS Interface.

CHI CERN Host Interface.

CP Crate Processor or Central Partition.

DAS Data Acquisition System.

DAST Direct Application Software for TANAGRA.

DDAP DELPHI Database Applications Package.

DELPHI Detector with Electron Photon and Hadron Identification ("Don't Ever Let Physics Hinder Ideas").

DELANA DELPHI Analysis and Reconstruction Program.

DELGRA DELPHI Interactive Graphics Program.

DELSIM DELPHI Simulation Program.

DST Data Storage Tape.

EMMASS Muon Chamber Mass identification module in DELANA.

EMF Forward Electromagnetic Calorimeter.

EMU Error Message Utility.

EP Elementary Process.

ES Event Supervisor.

FASTSIM DELPHI Fast Simulation Program

FCA Forward Chambers A.

FCB Forward Chambers B.

FEMC Forward Electromagnetic Calorimeter.

FE-RDY Front-End Ready (sent from Pandora to Zeus).

FIP Fastbus Intersegment Processor.

FRICH Forward Ring Imaging Cherenkov Counter.

G64 Micro-computer system used in slow-controls.

GEC Global Event Controller.

GES Global Event Supervisor.

GPM General Purpose Master.

GSW theory Glashow-Salam-Weinberg theory.

HBOOK CERN histogramming, fitting and data presentation package.

HCAL Hadron Calorimeter.

HFM HCAL, FEMC, MUB beam test experiment.

HLB Hit Latch Buffer.

HOF Forward Hodoscope.

HPC High Density Projection Chamber (Barrel Electromagnetic Calorimeter).

ID Inner Detector.

LES Local Event Supervisor.

LEP Large Electron Positron Collider.

LTD LEP Time Digitiser.

LTS-DB Local Trigger Supervisor Decision Box.

MEB Multi-Event Buffer.

MBM Model Buffer Manager.

MUB Barrel Muon Chambers.

MUBANA MUB first stage processing in DELANA.

MUBSIM MUB simulation processor in DELSIM.

MUONLINE MUB Online Monitoring and error diagnostic program.

MUF Forward Muon Chambers.

MVX Vertex Detector.

NEI-DONE Next Event Initialisation Done (sent from FIP to Pandora).

OD Outer Detector.

PANDORA Local Trigger Supervisor Box.

PAW Physics Analysis Workstation (CERN data analysis and presentation package).

PYTHHIA Global Trigger Decision Box.

SAT Small Angle Tagger.

SEB Spy Event Buffer.

SI Segment Interconnect.

T*n* *n*th level trigger.

TANAGRA Track Analysis and Graphics Package (see below).

TDC Time to Digital Converter.

TOF Time of Flight Counters.

TLA Three Letter Acronym.

TPC Time Projection Chamber.

VD (Micro)Vertex Detector.

VSAT Very Small Angle Tagger.

ZEUS Global Trigger Supervisor Box.

TANAGRA Data Hierachy

TD TANAGRA Detector Data bank.

TE TANAGRA Track Element bank.

TS TANAGRA Track String bank.

TK TANAGRA Track bank.

TB TANAGRA Track Bundle bank.

TV TANAGRA Tracks and Vertex bank.

TiX TANAGRA Extrapolation Bank.

TiR TANAGRA Results bank.

TiG TANAGRA Graphics bank.

Bibliography

[1] F.Halzen & A.D.Martin, "Quarks and Leptons", Wiley 1984
P.Renton, "Electroweak Interactions", Cambridge University Press 1990

[2] S.L.Glashow, Nucl. Phys.**22**(1961) 579
A.Salam, Phys. Rev. **127** (1962) 331
S.Weinberg, Phys. Rev. Lett **19** (1967) 1264

[3] I.J.R.Aitchison & A.J.G.Hey, "Gauge Theories in Particle Physics"(2nd Edition), Adam Hilger 1989

[4] C.N.Yang & R.L.Mills, Phys. Rev.**96** (1954) 191

[5] M.Kobayashi and T.Maskawa, Prog. Theor. Phys **49** (1973) 652

[6] P.W.Higgs, Phys. Rev. **145** (1966) 1156

[7] C.Rubbia, "The 'Future' in High Energy Physics", invited talk at European Particle Accelerator Conference, Rome, 7-11 June 1988, CERN-EP/88-130 (1988)

[8] D.A.Ross,J.C.Taylor, Nucl. Phys. B **51** (1973) 25
A.Sirlin, Phys. Rev. D **22** (1980) 971

[9] Particle Data Group,"Review of Particle Properties", Phys. Lett. **239B** (1990)

[10] DELPHI collaboration, "DELPHI Results on the Z^0 Resonance Parameters through its Hadronic and Leptonic Decay Modes", contributed to Singapore Conference, August 1990 (CERN-PPE/90-119)

[11] G.Burgers & F.Jegerlehner, "Δr, or the relation between the electroweak couplings and the weak vector boson masses", in "Z Physics at LEP1", (ed: G.Alterelli, R.Kleiss, C.Verzegnassi) (CERN89-08) (1989) p55

[12] M.Consoli & W.Hollik, "Electroweak radiative correction for Z physics", *ibidem*, p7

[13] J.E.Campagne, R.Zitoun, Z. Phys **C43** (1989) 469

[14] F.Dydak, "Proceedings of 1989 International Symposium on Lepton and Photon Interactions at High Energies", Stanford University, August 7-12,1989, p249

[15] M.Sands,"Introduction to the Physics of Electron Storage Rings", SLAC-121 UC-28, November 1970

[16] "LEP Design Report", CERN-LEP/84-01 (1984)

[17] See for example, "Proceedings of the ECFA Workshop on LEP 200", (ed: A. Böhm, W. Hoogland), Aachen, 29 September-1 October 1986, CERN 87-08 (1987)

[18] A.Blondel, "Polarization at LEP", invited talk at 1989 IUCF Topical Conference, Spencer, USA, 16-18 October 1989, CERN-EP/90-21 (1990)

[19] D.Treille, "Physics with the Pretzel LEP", CERN-EP/89-90 (1989)

[20] "DELPHI — A Detector with Lepton, Photon and Hadron Identification", Letter of Intent, 31 January 1982 (DELPHI 82-01)

[21] DELPHI Collaboration, "The DELPHI Detector at LEP", CERN-PPE/90-128 (1990), submitted to Nuclear Instruments and Methods

[22] DELPHI Collaboration, Phys. Lett. B **241-3** (1990) 435, and paper in preparation

[23] U.S. NIM Committee, "FASTBUS Modular High Speed Data Acquisition and Control System", U.S. Department of Energy, Division of High Energy Physics, DOE/ER-0189.

[24] F.Sauli, "Principles of Operation of Multiwire Proportional and Drift Chambers", CERN 77-09 (1977)

[25] T. Fearnley, M.Sc. Thesis, University of Oxford, 1987

[26] G. Delavallade, J.P. Vanuxem, "The LTD: A FASTBUS Time Digitiser for LEP Detectors", CERN EP-Electronics Note 85-06 (1987)

[27] A.C. Pinsent, "Experiments on the Muon Identifier for DELPHI", internal report, University of Oxford, May 1988
N.C.E. Crosland, "Drift Chamber Tests and Development of FASTSIM", internal report, University of Oxford, June 1988

[28] M.E.F.Veitch, A.C.Pinsent, V.Obratztsov, P.Eerola and R.Keranen, "Muon Identification Efficiencies from the HFM Experiment" DELPHI 89-57 PHYS 48
M.E.F.Veitch, D.Phil. thesis, University of Oxford, 1989

[29] S.D.Hodgson, "Muon Chamber Efficiencies in the Delphi Detector", internal report, University of Oxford, June 1990

[30] N.C.E.Crosland, "Some Interim Results on Echos", internal report, University of Oxford, November 1988

[31] E.Daubie *et al.*, "Improvement of the Stability of Operation of Drift Chambers Running in the Limited Streamer Mode in a Mixture of Ar-CO_2-C_4H_{10} (15-70-15) by the Addition of 2.5% Methylal to the Gas Composition" DELPHI 86-107 TRACK 41 (1986)

[32] A.C.Pinsent, D. Phil. Thesis, University of Oxford (1990)

[33] H.J.Klein, J.Zoll, "PATCHY Reference Manual" (revised for version 4.3), CERN Program Library (1988)

[34] R. Brun, J. Zoll, "ZEBRA - Data Structure Management System", CERN Program Library, Q100 (1987)

[35] Yu. Belokopytov, S. Gumenyuk, V. Perevozchikov, R. Yamaleev, "Detector Description Application Package: User Manual for Version 3.00", DELPHI 88-87 PROG 121 (1989)

[36] DELPHI Collaboration, "DELSIM DELPHI Event Generation and Detector Simulation — User's Guide", DELPHI 89-67 PROG 142 (1989)

[37] T. Sjöstrand *et al.*, "The LUND Monte Carlo Program", CERN Pool Programs W5035/W5045/W5046/W5047/W5048 Long Writeup (1989)
B. van Eijk, "EURODEC User Manual Version 2.3", DELPHI 89-39 PROG 136 (1989)

[38] DELPHI Collaboration, "DELPHI Data Analysis Program (DELANA) User's Guide", DELPHI 89-44 PROG 137 (1989)

[39] D. Bertrand, L. Pape, "TANAGRA Track Analysis and Graphics Package User's Guide", DELPHI 87-95 PROG 98 (1989)

[40] J. Cuevas *et al.*, "Fast Simulation for DELPHI - Reference Manual", DELPHI 87-27 PROG 72 Rev. (1987)

[41] L.Bugge, "Tracking of Charged Particles through DELPHI Calorimeter", DELPHI 89-04 PROG 125 (1989)

[42] A.Grant, "A Monte Carlo calculation of High Energy Hadronic Cascade in Matter", Nucl. Inst. Meth. **131** (1975) 167-172

[43] R. Brun, D. Lienart, "HBOOK User Guide", CERN Program Library, Y250 (1987)

[44] M.Winter, private communication

[45] S. Jadach & Z. Was, Comput. Phys. Commun. **36** (1985) 191.

[46] F.A.Berends, R.Kleiss, W.Hollik, DESY preprint DESY 87-094.

[47] R.Brun *et al.*, "Physics Analysis Workstation", CERN Program Library Q121.

[48] D.Reid & B.Nijjhar, private communication

[49] F.A.Berends, CERN 89-08, Volume 1 (1989) 89

[50] G.Bobbink *et al.*, LEP Absolute Energy in 1990, LEP Commissioning note no. 12 (1990), unpublished.

[51] P. Ratoff, private communication

[52] D.Yu Bardin *et al.*, Z.Phys. **C44** (1989) 493
M.S.Bileenky, A.A. Sazonov, JINR preprint E2-89-792, Dubna (1989)
T.Riemann *et al.*, "Proceedings of International Workshop on Radiative Corrections for e^+e^- collisions", Tegernsee, 3-7 April, 1989, p162

[53] F.James, M.Roos, "Function Minimization and Error Analysis", CERN Program Library, D506 (1985)

[54] K.Abe *et al.*, Phys. Rev. Lett. **62** (1989) 1709
J.Dorenbosch *et al.*, Z.Phys. **C41** (1989) 567

[55] DELPHI Collaboration, Phys. Lett. **B241** (1990) 425

[56] F.Dydak, contribution to the Singapore Conference, August 1990

[57] W.Venus, private communication

[58] L. Lyons, "Statistics for Nuclear and Particle Physicists", p88, Cambridge University Press (1986)

[59] DELPHI Collaboration, Phys.Lett. **252B** (1990) 149.

[60] G. Burgers, CERN 88-06 Volume 1, p121.

[61] M.J.Bates, "The Oxford Muon Chamber Test Rig and the DELPHI Barrel Muon First and Second Level Trigger", internal report, University of Oxford, June 1989

[62] C.J.Beeston, "Third Level Trigger for the DELPHI Barrel Muon Chambers", internal report, University of Oxford, May 1989

[63] G. Goujon, M. Mur, "FIP, FASTBUS Intersegment Processor", DELPHI presentation, November 1985
Ph. Charpentier, G. Goujon, M. Gros, M. Mur, B. Paul, "The FASTBUS Intersegment Processor", presented at IEEE Conference, Washington, October 1986

[64] B. Rossi, "High Energy Particles", Prentice-Hall, New York (1952)

[65] H. Burmeister *et al.*, CERN/TCL/Int 74-7 (1974).